FRIEDRICH-ALEXANDER
UNIVERSITÄT
ERLANGEN-NÜRNBERG

CENEM
Center for Nanoanalysis
and Electron Microscopy

Master's thesis in the field of Nanotechnology

Interface design of Au_xNi_{1-x} alloy nanoparticles on (0001) oriented α-Al_2O_3 investigated by X-rays and electrons

presented by

Martin Dierner

Institute of Micro- and Nanostructure Research

Prof. Dr. rer. nat. habil. Erdmann Spiecker

Supervisor: Dr. Johannes Will

Erlangen, 16. März 2020

Acknowledgment

First, I would like to thank **Prof. Erdmann Spiecker** for giving me the opportunity to work on this highly interesting topic at his Institute of Micro- and Nanostructure Research at the Friedrich-Alexander University and to get an insight in characterization methods of materials with electrons and x-rays.

My special thanks go to **Johannes Will** for supervising the work and the valuable support and discussions during the data evaluation, especially regarding the X-ray scattering methods.

Furthermore, I would like to thank
... **Thomas Przybilla, Tadahiro Yokosawa, Mingjian Wu** and **Peter Denninger** for the guidance and the support on the *Titan* and the FIB/SEM
... **Johanna Schubert** and **Dorota Kubacka** for the guidance on the *Winter E-beam HVB 130* and the RTA furnace
... **Tobias Zenk** from the Institute for Crystallography and Structural Physics (ICSP) for the guidance on the *Rigaku* helping by the performance of the XRD measurements
... **Johannes Dallmann** from the ICSP providing me his self-written python script for the plotting of XRD pole-figures
... **Dong Wang** from the TU Ilmenau for the usage of their RTA-system
... **Nicolas Karpstein** and **Malte Lenz** for the entertaining coffee breaks and the supply of extremely delicious coffee during the whole time of the master thesis
... all others from the **WW9-Team** for the nice atmosphere and fun at the institute

Last but not least I appreciate the support of the *Center for Nanoanalysis and Electron Microscopy (CENEM)* and the Graduate School *GRK 1896 "In situ Microscopy with Electrons, X-rays and Scanning Probes"*, that made it possible to accomplish this research.

Abstract

In this work, the epitaxial interface between Au_xNi_{1-x} and α-Al_2O_3 is investigated. For preparation Au/Ni bilayers are e-beam evaporated on (0 0 0 1) oriented α-Al_2O_3. Rapid thermal annealing of the bilayers at 935 °C for 120 s in reducing atmosphere is used to fabricate Au_xNi_{1-x} alloy nanoparticles. To suppress phase separation, the samples are quenched after heating. The lattice parameter of the particles is systematically controlled via the Au concentration. XRD out-of-plane measurements confirmed the successful formation of AuNi alloy particles and show that the out-of-plane lattice parameter follows the expected values for AuNi bulk alloys. Furthermore, the dependence of the texturing on the atmosphere is shown, e.g. a predominant (1 1 1)-texturing for high H_2-flow rates. The combination of XRD out-of-plane and in-plane measurements reveal a pronounced AuNi (1 1 1) [1 $\bar{1}$ 0] $\parallel$ α-Al_2O_3 (0 0 0 1) [1 0 $\bar{1}$ 0] orientation relationship (OR1). (1 1 1) AuNi XRD pole-figures reveal the existence of two twin variants within OR1. In addition, two further twin variants can be found where the particles are rotated by ±18 degrees around the ⟨1 1 1⟩ surface normal, changing the orientation relation to AuNi (1 1 1) [$\bar{3}$ 2 1] $\parallel$ α-Al_2O_3 (0 0 0 1) [1 0 $\bar{1}$ 0] (OR2). For particles with a mismatch >1 % a diffuse signal can be observed in the in-plane measurements, which originates from buckling of the terminating layer at the interface (delocalized coherent interface). The vanishing of the diffuse signal for particles with 55 at.% Au indicates a change in the interface structure from a delocalized coherent interface to a semi-coherent interface. These findings are complemented by TEM investigations of plan-view prepared lamellas showing the NP-substrate interface. EBSD measurements confirmed the presence of both twin variants of OR1 within the lamella. The TEM observations strengthen the picture of a semi-coherent interface obtained by in-plane XRD measurements due to the rise of hexagonal (Twin1) and triangular (Twin2) shaped misfit dislocation networks.

Contents

List of abbreviations and symbols

Abbreviations

α-Al_2O_3	Corundum
ADF	Annular Dark Field
Ag	Silver
Ar	Argon
Au	Gold
BF	Bright Field
BFP	Back Focal Plane
BSE	Backscattered Electrons
CBS	Concentric Backscatter
CTEM	Conventional Transmission Electron Microscopy
Cu	Copper
CVD	Chemical Vapor Deposition
DF	Dark Field
DP	Diffraction Pattern
EBID	Electron Beam Induced Deposition
EBSD	Electron Back Scatter Diffraction
ECS	Equilibrium Crystal Shape
EDX	Energy Dispersive X-Ray Spectroscopy
ETD	Everhart-Thornley Detector
FEG	Field-Emission Gun
FIB	Focused Ion Beam
FWHM	Full Width at Half Maximum
GIS	Gas Injection System
H_2	Hydrogen
HAADF	High-Angle Annular Dark Field
IBID	Ion Beam Induced Deposition
MD	Molecular Dynamics
Me	Metal
Ni	Nickel
NPs	Nanoparticles

OR	Orientation Relation
PVD	Physical Vapor Deposition
RTA	Rapid Thermal Annealing
RTP	Raqpid Thermal Processing
SAD	Selected-Area Diffraction
SE	Secondary Electrons
SEM	Scanning Electron Microscopy
SSD	Solid-State Dewetting
STEM	Scanning Transmission Electron Microscopy
TEM	Transmission Electron Microscopy
TLD	Through-Lens Detector
TTT	Time Temperature Transformation
XRD	X-Ray Diffraction
ZA	Zone Axis

Symbols

$\boldsymbol{b}$	Burgers vector	[nm]
$\boldsymbol{k'}$	scattered wave vector	[nm^{-1}]
$\boldsymbol{k_0}$	incident wave vector	[nm^{-1}]
$\boldsymbol{Q}$	scattering vector	[nm^{-1}]
δ	lattice mismatch	[%]
γ_{pv}	surface energy of the uppermost particle facet	[$\mathrm{J\,m}^{-2}$]]
γ_{sp}	substrate-particle interfacial energy	[$\mathrm{J\,m}^{-2}$]
γ_{sv}	surface energy of the substrate	[$\mathrm{J\,m}^{-2}$]
γ_S	surface energy	[$\mathrm{J\,m}^{-2}$]
λ	wavelength	[nm]
ν_S	number of atoms per unit area	[nm^{-2}]
Ω_a	atomic volume	[$\mathrm{m}^3\,\mathrm{mol}^{-1}$]
$\mathrm{at.\%}_x$	atomic fraction of element x	[at.%]
$\mathrm{vol.\%}_{Au}$	volumic fraction of Au	[vol.%]
τ	equilibration time	[s]
θ_B	Bragg angle	[°]
a_{Au}	lattice parameter of Au	[Å]
a_{Layer}	lattice parameter of the film/particle	[Å]
a_{NiAu}	lattice parameter Au/Ni solid solution	[Å]
a_{Ni}	lattice parameter of Ni	[Å]

a_{Sub}	lattice parameter of the substrate	[Å]
d	dislocation spacing	[nm]
d_{hkl}	lattice plane spacing	[nm]
D_S	surface diffusion coefficient	$[m^2\,s^{-1}]$
F_{hkl}	structure factor	[-]
f_n	atomic scattering factor	[-]
g_{hkl}	reciprocal lattice vector	$[nm^{-1}]$
k	*Boltzmann* constant	$[J\,K^{-1}]$
R	particle radius	[nm]
T_{abs}	absolute temperature	[K]
x_{Ni}	percentage of Ni	[-]

List of Figures

List of Tables

1 Introduction

The phenomenon of solid-state dewetting (SSD) has originally gained attention since it weakens or destroys nanoscaled products and the focus of research was therefore on avoiding this effect. Several studies were carried out over the years to understand the underlying meachanism of SSD and therefore how to control it. The control of this process made it possible to use the previously undesired effect to produce complex nanostructures for a wide range of applications at low cost and without time-consuming work [1].
In many of these applications such as metal-ceramic sensors, catalysts, power electronics etc. metal-ceramic interfaces play an important role [2–4]. Due to the different thermal expansion coefficients of metals and ceramics and, in general, a high lattice mismatch applications suffer from mechanical stresses making the metal-ceramic interfaces the weak point in the device [5]. The usage of a binary alloy system on the metal side offers the possibility to tailor and systematically reduce the mismatch, leading to a less strained interface with improved mechanical stability.

In this thesis the AuNi system is used to fabricate Au_xNi_{1-x} alloy nanoparticles by equilibrating Au/Ni bilayers on (0 0 0 1) oriented α-Al_2O_3 using SSD. First a parameter study is carried out with respect to the process-parameter for the production of the alloyed particles. Second the Au concentration is varied to systematically control the lattice-mismatch between the particles and the substrate and therefore control and respectively design the interface of both materials. The particle-substrate interface and the orientation of the NPs is investigated by X-rays and electrons.

2 Fundamentals of solid-state dewetting

As-deposited thin films are usually metastable, which leads to the formation of particles or arrays of islands when the film is heated. This process is called dewetting and is driven by the minimization of the total surface and interfacial energies [1]. The process is shown schematically in Figure 2.1. With decreasing film thickness down to several nanometers, there is a strong increase in the driving force, which leads to dewetting already below the melting temperature of the materials. This process is called solid-state dewetting (SSD) [1]. In the following sections the processes of solid-state dewetting and the dewetting behaviour of Au/Ni-bilayers is explained in more detail.

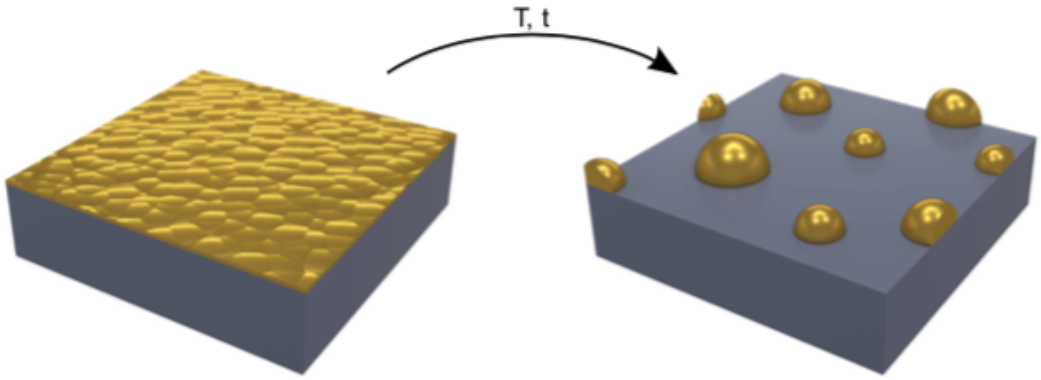

Figure 2.1: Shematic visualisation of the formation of droplets from a thin film during dewetting, reprinted from Niekiel [6].

2.1 Thermodynamics

The driving force for solid-state dewetting is the reduction in total energy of the material system. Since thin films have a high surface-to-volume ratio which is energetically unfavorable, the supply of thermal energy leads to a reduction of the surface area through particle formation and thus to a reduction of the total energy [1]. This process

is known as wetting behaviour and for isotropic interfaces well described by the Young-Laplace equation, where the surface energy of an equilibrated system is represented by the wetting angle [7, 8].
However, the assumption of isotropic interface energies only applies to the interfaces of liquid and amorphous solids. In the case of solid-state dewetting of crystalline materials, the situation is more complex due to possible anisotropic surface energies [9]. Caused by the anisotropy, an isolated solid particle has a facetted equilibrium shape known as the *Wulff* shape, which is given by the *Wulff* construction and is explained more detailed in Section 2.3.

2.2 Phenomenology

Generally, the process of solid-state-dewetting can be divided into three different stages, the nucleation of voids, void growth and particle formation. The first necessary step is the nucleation of voids, since a thin film is stable to pertubations smaller than the film thickness [1]. There are two possible ways in polycrystalline films for the nucleation of voids. One approach is grain boundary grooving, which was first modelled by Mullins and extensively treated theoretically by Srolovitz and Safran [10, 11]. In this model dewetting appears from the free surface to the interface via surface diffusion, which means that the influence of the film-substrate interfacial energy is ignored. The bottom-up equivalent is the void nucleation from the interface, which occurs when the interfacial energy is relatively high. For both methods the preferred nucleation sites are grain boundaries and grain boundary triple junctions [1, 9, 12].

Second, once a void of critical size has nucleated, void growth takes place. One approach for the growth mechanism is edge retraction via the diffusion of material along different diffusional paths. While the common view of edge retraction is based on surface self diffusion [13], also other mechanisms like grain boundary diffusion and interface diffusion are reported [14, 15]. During edge retraction, an elevated rim is formed connected to a depression zone in front of the corresponding rim. Further deepening of the depression zone leads to a pinch-off as soon as it reaches the substrate [1].
Due to the anisotropy of surface energies in crystalline materials, also texture evolution takes place during the process of SSD, starting in the early stages during grain growth [16]. By a preferential growth of grains with a favourable orientation a typical texture evolves, resulting in the parallel alignment of a low-index facet with respect to the substrate. Thus, for fcc metals, a $\{1\,1\,1\}$ out-of-plane texture arises since the

{1 1 1} planes are the closest packed planes with the lowest surface energy. Given that the interface-energy of a metal film (or particle) and a single-crystalline substrate is orientation-dependent, a preferred in-plane texture can also be expected. For example, well known orientation relations of equilibrated fcc-metals on (0 0 0 1)-oriented sapphire are Metal (Me) $(1\,1\,1)[1\,\bar{1}\,0]\|$sapphire $(0\,0\,0\,1)[1\,0\,\bar{1}\,0]$ and Me $(1\,1\,1)[1\,\bar{1}\,0]\|$sapphire $(0\,0\,0\,1)[2\,\bar{1}\,\bar{1}\,0]$ [17–19].

2.3 Particle formation

The formation of particles occurs in the final stage of SSD. Due to repeated pinch-off elongated cylindrical structures form which are far away from the equilibrium crystal shape (ECS). Therefore the structures further decay into particles, which can be described by *Rayleigh* instabilites [20].
After the *Rayleigh*-like breakup, the equilibration of the particles can be illustrated by the *Wulff/Winterbottom*-construction, which is based on the anisotropy of surface energies in solid crystalline materials. By plotting the surface energy vector with respect to the surface directions, the ECS of an isolated particle is obtained [21]. This can be seen in Figure 2.2. The vector γ_{hkl} is plotted with a length proportional to the absolute magnitude of the anisotropic surface energy, represented by the solid black line. The ECS can be constructed by an inner envelope of planes perpendicular to γ_{hkl}, which minimizes the total surface energy by an optimization of relative surface areas of different crystallographic planes [9].

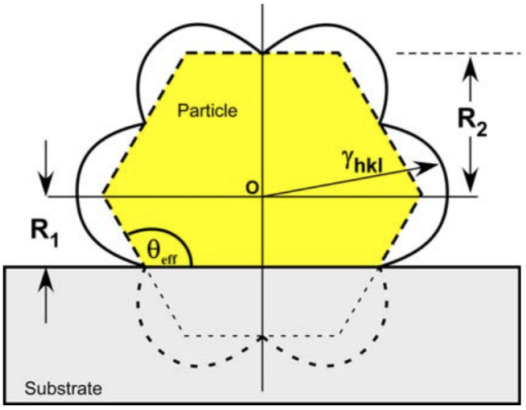

Figure 2.2: Schematic drawing of the Winterbottom analysis for an equilibrated particle on a substrate, reprinted from Sadan and Kaplan [8].

In case of particles on a crystalline support, also the interface between substrate and particle has to be considered. Therefore a modified *Wulff* approach was introduced by

Winterbottom [22] dealing with the generated interface as a function of particle heigth and contact angle. By measuring the distance from the center of the *Wulff* plot (*Wulff*-point, O) to the particle-substrate interface (R_1) and the distance from the *Wulff*-point to the uppermost facet of the particle (R_2) (see Figure 2.2) the interfacial energy of single-crystalline particles can be determined using [8]:

$$\frac{R_1}{R_2} = \frac{\gamma_{sp} - \gamma_{sv}}{\gamma_{pv}} \tag{2.1}$$

where γ_{sp} is the substrate-particle interfacial energy, γ_{sv} the surface energy of the substrate and γ_{pv} the surface energy of the uppermost particle facet.
Furthermore, the time τ necessary for the equilibration of a particle at a certain temperature can be estimated with the following equation determined by Nichols et al. [23]:

$$\tau = \frac{1}{24} \frac{kT}{\gamma_S D_S \nu_S \Omega_a^2} R^4 \tag{2.2}$$

with k as *Boltzmann* constant, T as absolute temperature, γ_S as surface energy, D_S as surface diffusion coefficient, ν_S as the number of atoms per unit area, Ω_a as the atomic volume and R the particle radius.

2.4 Solid-state dewetting of Au/Ni-bilayers

While the dewetting mechanism for thin metallic films is well understood, the situation regarding bilayer films is more complex. The SSD behaviour may be influenced by kinetic aspects like different melting temperatures of the different elements, segregation effects due to different surface and interface energies and the thermodynamics of the overall alloy system. Especially the Au/Ni system is a special material system due to the miscibility gap, which extends over the whole concentration range (see Section 4.1). This section is intended to provide a brief review of the state of knowledge on the solid-state dewetting of Au/Ni-bilayers.

One of the first studies that deals with the dewetting behavior of Au/Ni bilayer is the work of Wang and Schaaf [24]. In this early work, they performed SSD of Au/Ni bilayer on a SiO_2/Si substrate at 650 °C and 850 °C for 1 h in argon (Ar) atmosphere, to produce bimetallic Au/Ni nanoparticles. While the particles produced at 650 °C have a node-shaped morphology, the particles produced at 850 °C are more spherical in nature.

They also observed a change in texture from (1 1 1) to (2 0 0) by X-ray diffraction studies, which was explained with the relaxation of the strain energy induced by the alloying since (1 0 0) oriented particles possess the smallest strain energy densities.
Herz et al. continued with the fabrication of Au/Ni nanoparticles via SSD. By changing the atmosphere from Ar to an Ar/H_2 gas mixture and performing the annealing at 950 °C, which is well above the miscibility gap, they succeeded in fabricating supersaturated Au/Ni nanoparticles with a strong (1 1 1) out-of-plane structure [25]. By subsequently annealing these particles for 16 min at 650 °C, the study of phase separation with respect to the particle's equilibrium crystal shape was carried out. It was found that Ni is enriched on {1 0 0} and Au on {1 1 1} faceting planes. By performing quantum-mechanical calculations they explained the stabilization of the Ni-rich phase by the minimization of its elastic strain energy on the respective facet [26].
In addition to the studies around alloy nanoparticles (NPs), Herz et al. also investigated changes in the dewetting behaviour of Au/Ni bilayers as a function of temperature and stacking sequence of the bilayers. In the first study they examined the behaviour of Au/Ni bilayer (Ni at the bottom) by annealing the samples from 500 °C to 900 °C for 1 min. In general, with increasing temperature, an increase of the dewetted surface could be observed except at 700 °C indicating a temperature-dependent change in the dewetting mechanism. At 650 °C film rupturing occurs either via thermal grooving or void nucleation and the resulting voids are predominantly found at the phase boundaries evolving in a branch-like manner (fractal growth) due to Au segregations on the surface. This is in good agreement with earlier studies by Petersen and Mayr [27], who investigated the dewetting behaviour of immiscible Ag-Ni films. Contrary to expectations, the increase of the temperature to 700 °C led to a smaller area of the holes, which was attributed to the increased solubility of Au and Ni by means of X-ray diffraction. By further raising the temperature above the miscibility gap to 900 °C the dewetted state could be reached and elongated and flat supersaturated Au/Ni agglomerates with similar stochiometry like the inital bilayer have formed. In addition, the dewetting rate of Au/Ni bilayer is determined not only by the temperature but also by the stacking sequence. The deposition of Ni on Au leads to a less stable film due to already existing GB grooves in the Au film. In turn, Ni as the lower layer leads to better wetting of the substrate and thus to a more stable film. Exact reasons for a superior film stability with Au as an overlayer were not mentioned in the work of Herz et al. [28, 29].
Cen et al. discovered while heating Au/Ni-Bilayers at 675 °C, with Au as top layer and Ni as the bottom layer, Au diffuses along the grain boundaries to the SiO_2-substrate interface. They suggested that the reversal of the layer stacking is responsible for the

delay in dewetting observed by Herz [30, 31].
Barda et al. [32] studied the influence of a minor alloying addition of Au on the thermal stability of Ni thin films on sapphire. The doping took place in three different ways: by uniform alloying, by deposition of a Ni-Au-Ni trilayer and by depositing an Au overlayer on the Ni film. The latter showed the best retardation effect on the dewetting rate indicating that surface diffusion is the dominating factor controlling the kinetics of solid-state dewetting in the Ni(Au) system.

3 Interfaces

Interfaces play an important role with respect to the development of the microstructure of metals and alloys. The following sections first explain the three most common types of interfaces followed by a section dealing with the metal-α-Al_2O_3 interface.

3.1 Different types of interfaces

In general interfaces can be divided into three different types, which are coherent, semi-coherent and incoherent (see Figure 3.1).
The type of interface developing between two crystalline materials depends on their lattice mismatch, which is calculated as:

$$\delta = \frac{a_{Sub} - a_{Layer}}{a_{Sub}} \tag{3.1}$$

where a_{Sub} is the lattice parameter of the substrate and a_{Layer} the lattice parameter of the material (e.g. particles) on top of the substrate.
Coherent interfaces form when the lattice mismatch of two crystals is zero and the two lattices are continous across the interface (Figure 3.1a). Also for very small mismatches it is possible to form coherent interfaces by straining one ore both of the lattices. In semi-coherent interfaces (Figure 3.1b) large areas of coherency are obtained by a tensile or compressive distortion of the interfacial layers for the optimization of nearest neighbour bonding. To reduce the total elastic strain, misfit dislocation arrays are formed, separating the coherent areas [33]. The spacing of the dislocations is calculated as follows:

$$d = \frac{|\mathbf{b}|}{\delta} \tag{3.2}$$

where $|\mathbf{b}|$ is the burger's vector of the dislocations and δ the lattice mismatch.
The energy of semi-coherent interfaces arises from that of a fully coherent one plus the dislocation energies. Therefore with decreasing dislocation spacing the energy increases until the dislocation strain fields overlap. At this point the interface becomes incoherent (Figure 3.1c) since the discrete nature of the dislocations is lost [34].

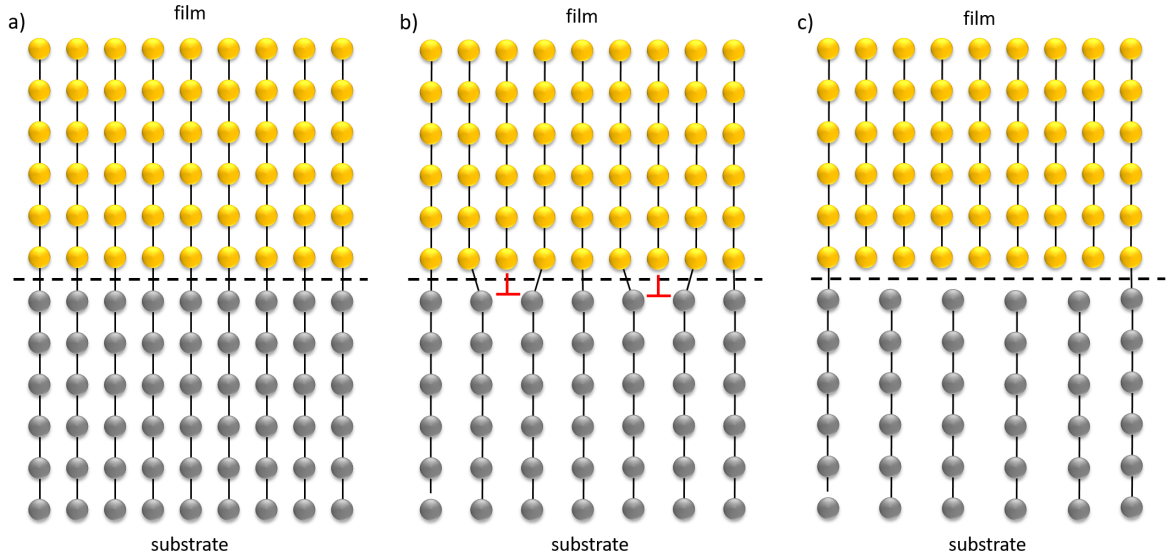

Figure 3.1: Schematic visualisation of the different types of interfaces. a) unstrained coherent interface; b) Semi-coherent interface with misfit dislocations (red); c) incoherent interface. The image is adapted from [35]

3.2 The metal-Al_2O_3 interface

Several studies of as-deposited metal-films on sapphire revealed an incoherent interface due to a large misfit between the film and the substrate [36, 37].

With incoherent interfaces it is usually assumed that the atoms at the interface retain their bulk positions up to the interface layer. Meltzman et al. [19] mentioned that this is not valid for equilibrated systems. By dewetting pure Ni on α-Al_2O_3 they showed that the terminating Ni layer rearranges its structure due to a local periodic shift of the atoms at the interface caused by stresses from both interface sides (*interface reconstruction*) (Figure 3.2a). To accomodate the strain induced by the high mismatch of the two materials, the Ni layers close to the interface buckle in a periodic manner owing to the coincidence symmetry of the two lattices. Due to the periodicity of the buckling this phenomenon is called *delocalized coherency* (Figure 3.2b).

In 2012 Pilania et al. [38] studied the semi-coherent interface of aluminium on sapphire by molecular dynamics simulation. Their analysis reveals an interface dislocation network with three sets of parallel, pure-edge dislocations with a line direction in $\langle 1\,1\,0 \rangle$ and a burger's vector of $\frac{a}{6}\langle 2\,1\,1 \rangle$. By relaxing the structure at 0 K, hexagonal shaped coherent-like areas and triangular shaped stacking-fault-like regions at the interface show up, separated by the dislocation lines (see Figure 3.2c). Further relaxation of the structure at 500 K rigidly shifts the dislocation lines leading to a change of the dislocation pattern due to a competition between the stacking fault energy and the dislocation

interaction energy at the interface. The final structure reveals triangle-shaped coherent and stacking fault like areas (see Figure 3.2d).

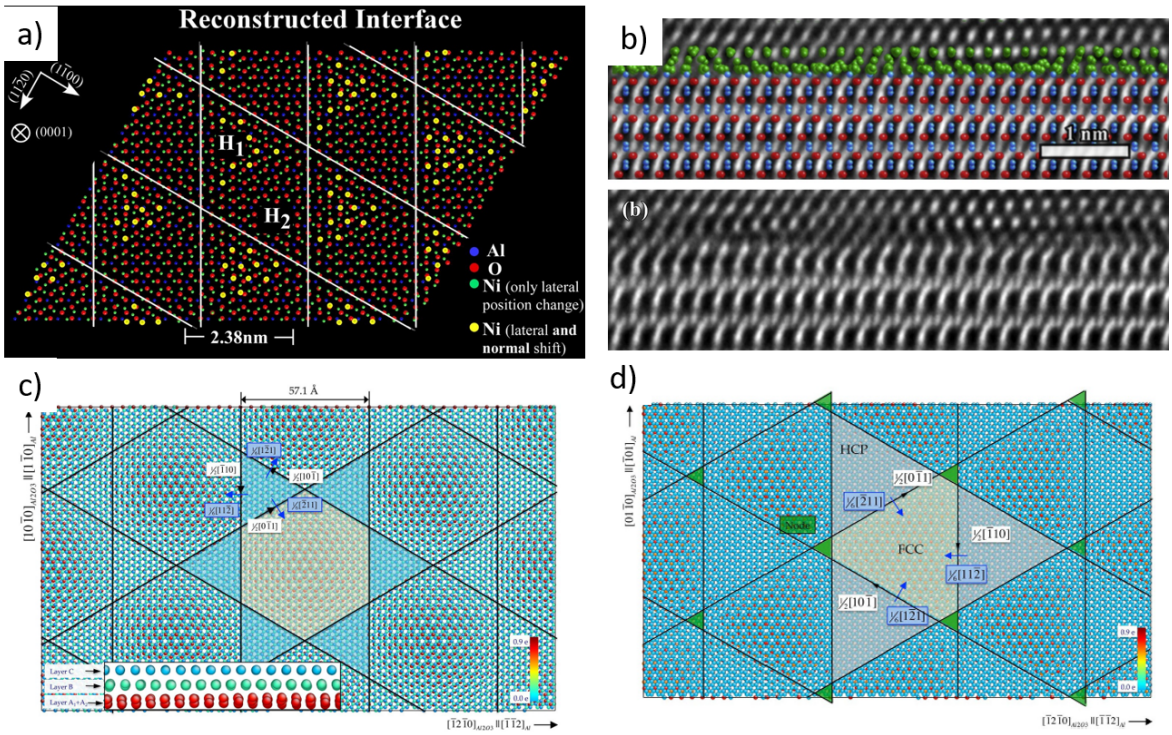

Figure 3.2: a) Interface reconstruction at equilibrated Ni on α-Al_2O_3 due to a local periodic shift of the atoms at the interface caused by stresses from both interface sides. b) Buckled Ni layer close to the interface for misfit accomodation [19]. c) Hexagonal misfit-dislocation network at the aluminium-sapphire interface. d) Triangular misfit-dislocation network at the aluminium-sapphire interface. a) and b) are reprinted from Meltzman et al. [19] and c) and d) are reprinted from Pilania et al. [38].

4 Materials and Methods

This chapter introduces the material system and methods used.

4.1 The Nickel-Gold system

The phase diagram of the binary Au/Ni system is shown in Figure 4.1. Characteristic for this system is a miscibility gap covering the whole concentration range in the solid state below 130 °C. While at lower temperatures, phase decomposition occurs into an Au- and Ni-rich phase, AuNi solid solutions can be produced by annealing the system at elevated temperature (dependent on the Au concentration) with a subsequent quenching from the high temperatures to room temperature. This makes the system very interesting for the SSD-process, since both bimetallic particles and AuNi-alloy nanoparticles can be produced (see Section 2.4).

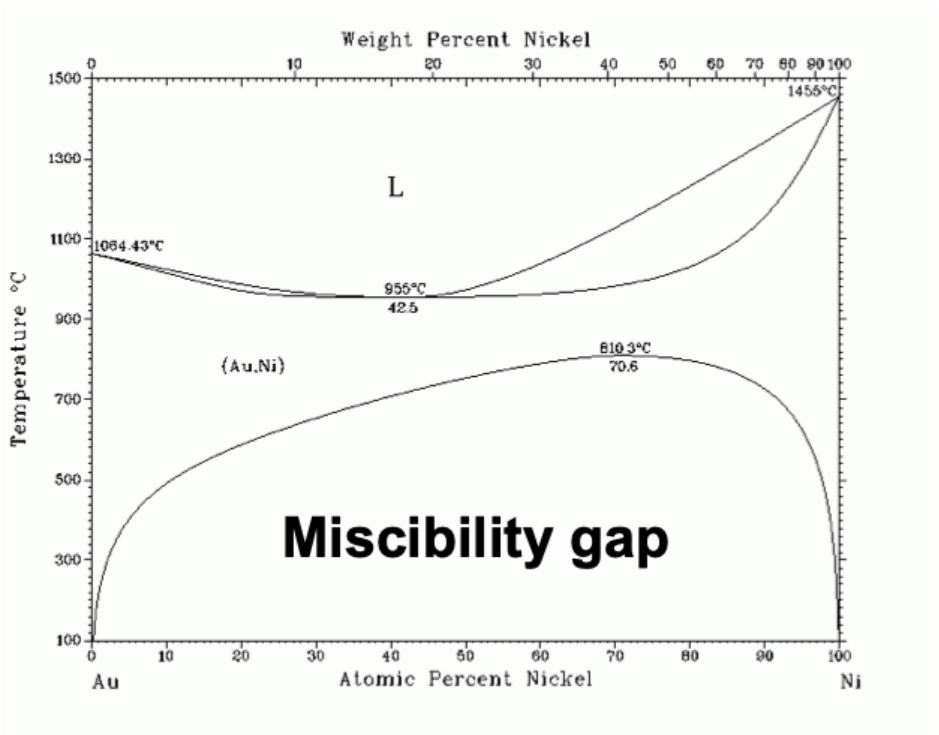

Figure 4.1: Calculated phase diagram of the Au-Ni system [39].

4.2 Electron beam evaporation

A common way to create thin metal films of high purity is via physical vapour deposition induced by an electron beam. In this process (see Figure 4.2), an intense beam of high-energy electrons, which are emitted by a cathode, is used to vaporize the material. To achieve a long mean free path of electrons and to avoid unwanted impurities, the whole PVD-process is carried out at pressures below 2×10^{-5} mbar. In order to avoid contamination by the cathode material, the cathode is placed out of sight of the material to be evaporated. The electrons are accelerated by using an electric field with a potential of 10 kV to 40 kV and are focused on the target material (anode) by help of a magnetic field. The target-material is placed in a crucible with a higher melting point. By directing the e-beam on the surface of the material, the kinetic energy of the electrons is converted into various forms due to their interaction with the atoms, like x-rays, backscattered electrons, secondary electrons of the target-material and thermal energy. For melting or sublimating of the material only a small fraction of the total energy is relevant, the thermal energy. The sublimated material is then deposited on the cooler substrate, which is mounted above the evaporation source [40].

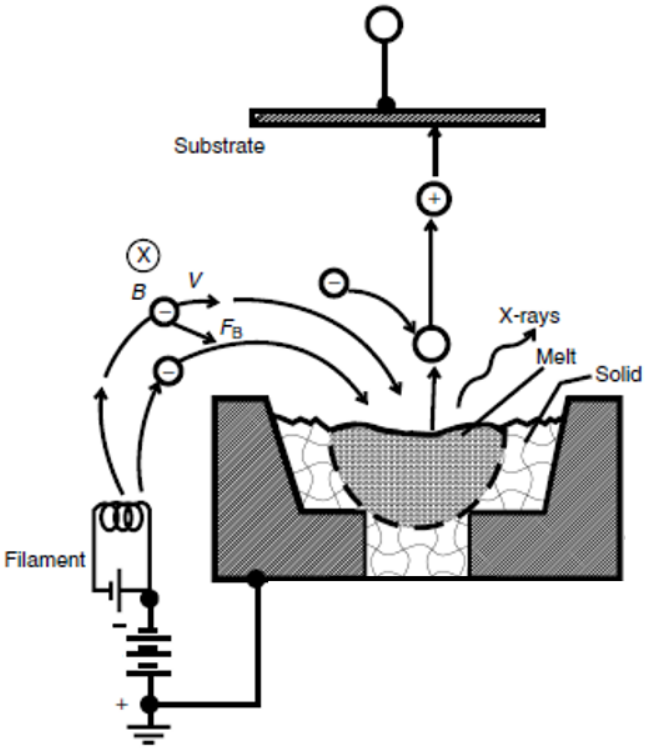

Figure 4.2: Schematic process of e-beam induced evaporation, adapted from [40].

The device used in this work for the fabrication of the Au/Ni bilayers is a Winter E-beam HVB 130, which is shown in Figure 4.3. The system is equipped with two electron guns and the corresponding set of crucibles. Only the e-gun 2 (right side) was used in this thesis. For the evaporation of the target material a acceleration voltage of 10 kV was used. The layer thickness is measured *in situ* by oscillating quartz crystals. For precise thickness measurements, the quartz crystal has to be calibarated by a tooling factor. In this work the tooling factors for nickel and gold, which had already been determined in advance, were used. For a detailed description of the sample preparation the reader is referred to Section 4.6.

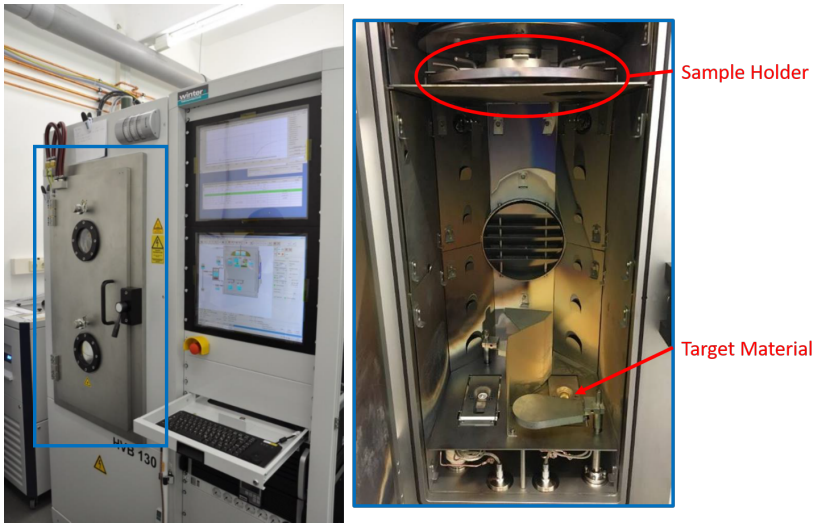

Figure 4.3: The PVD system HVB 130 from Winter used in this work.

4.3 Scanning electron microscopy (SEM) and Focused Ion Beam (FIB)

Scanning electron microscopy (SEM) is the most widely applied characterization method in materials science. In this thesis, a Helios Nanolab 660 dualbeam system from FEI (see Figure 4.4 a) is used. The electrons are emitted by a field emission gun and then accelerated with voltages in the range of 500 V to 30 kV. The beam is focused on the sample with several lenses and scanned over it using raster coils.
The dualbeam setup can be seen in Figure 4.4 b). In addition to the electron column, a Tomahawk ion column is mounted at an angle of 52° which enables deposition and processing on the nanoscale in addition to imaging using a liquid metal gallium source. Similar to the SEM the gallium ions are accelerated by a potential in the range of 500 V

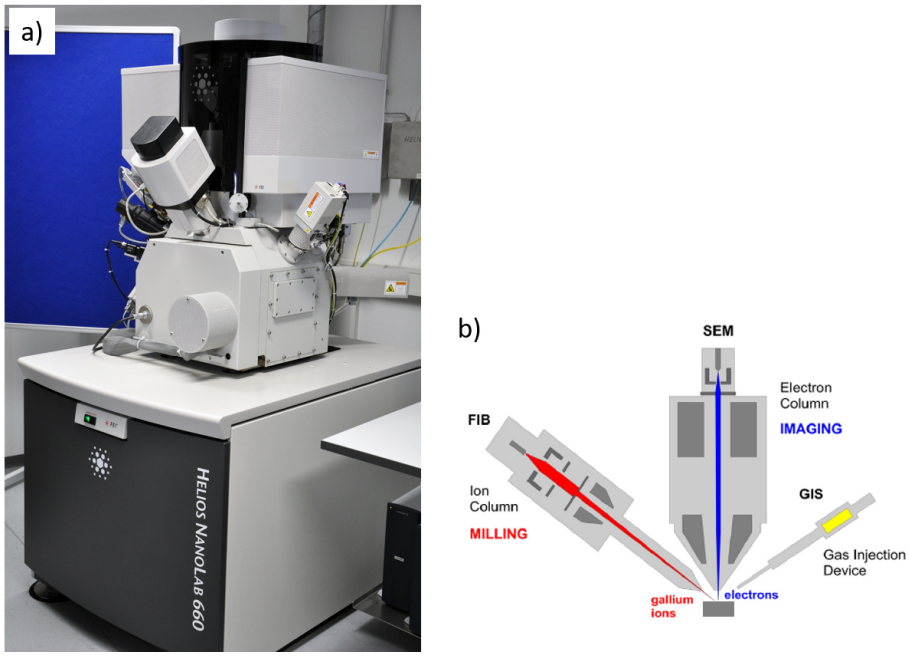

Figure 4.4: a) The Helios Nanolab 660 used in this work, b) Dual beam arrangement adapted from Rigort et al. [41].

to 30 kV and are focused on the sample via several lenses and apertures leading to a maximum resolution of 2.5 nm [42].
The principles of imaging with a SEM as well as milling and deposition with the FIB will be described in more detail in the following sections.

4.3.1 Electron-Specimen interactions in Scanning electron microscopy

The accelerated and focused electron beam interacts with the sample in a certain volume, which is called the *interaction volume* and is schematically illustrated in Figure 4.5.
The interaction between the incident electrons and the specimen can be divided in inelastic and elastic interactions, leading to different contrasts.
Secondary electrons (SE) are generated by primary electrons which are scattered inelastically in the sample. This scattering process leads to an ejection of electrons from the surface atoms, when the energy of the incident electrons is high enough. Due to the low energy of SE (up to 50 eV), their exit depth is limited to near surface-regions of approximately 50 nm. The interplay of a low exit depth, enhanced emission at edges or small particles and the shadowing effect resulting from incomplete collection is used for imaging the surface topography of the specimen. Common detectors for SE are the

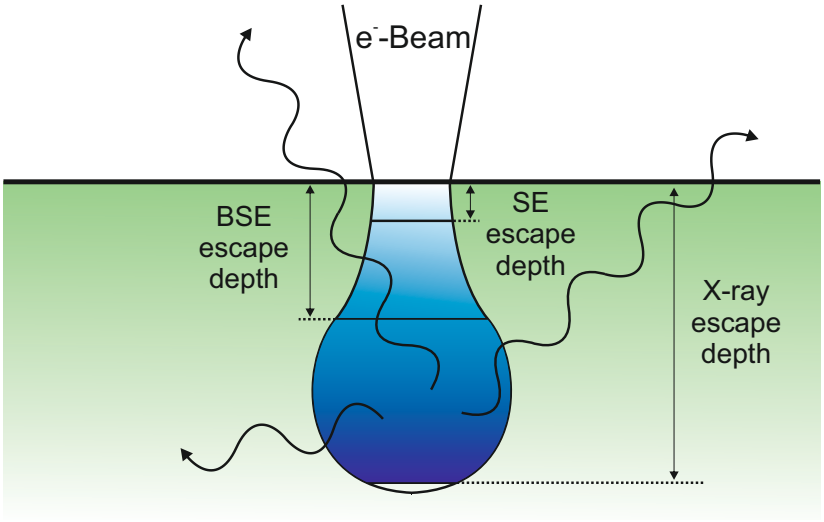

Figure 4.5: SEM interaction volume of electrons with the sample, adapted from Hafner [43].

Everhart-Thornley Detector (ETD) and the Through-Lens Detector (TLD). The TLD is located inside the column above the pole piece and is the main detector used for SE imaging in this work, as the resolution can be improved by applying a magnetic field (immersion mode) [44].

Another important signal is that of backscattered electrons (BSE) which are incident electrons leaving the specimen after elastic and inelastic scattering processes. BSE have much higher energies than SE (up to 30 keV) since they only lose a fraction of their initial energy and can therefore penetrate deeper specimen regions. The elastic processes are interactions with the electrical field of the nucleus of target atoms, whose probability depends strongly on the atomic number Z. The dependence of the contrast on the atomic number makes it possible to detect phases of different Z-values, which is why the BSE signal is mainly used for material contrast [44, 45]. Within this thesis a concentric backscatter (CBS) detector was used for the BSE-imaging, sitting directly below the pole piece. The advantage of such a ring-shaped detector lies in the higher solid angle of collection, resulting in a stronger signal compared to e.g. ETD detectors [45].

For the performance of analytical measurements the SEM is also equipped with a large area *Oxford Instrumets* energy-dispersive X-ray (EDX) detector. In this work the SEM-EDX system is used to quantify the actual gold content of each sample and to create qualitative EDX-mappings to visualize the distribution of Au and Ni. The expansion of the interaction volume plays an important role for high-quality mappings on nanostructures, which is calculated with the following empirical formula [45]:

$$R_x = \frac{64}{\rho}(E_0^{1.68} - E_c^{1.68}) \tag{4.1}$$

with R_x as the depth of X-ray production in nm, ρ as density of the sample material, E_0 as energy of the primary electron beam in keV and E_c as ionization energy of the sample-material in keV. Using the ionization energies and densities of Au and Ni [46], the expansion of the interaction volume can be calculated for Au to 50 nm ($E_0 = 5\,\text{keV}$) and 508 nm ($E_0 = 20\,\text{keV}$) and for Ni to 107 nm ($E_0 = 5\,\text{keV}$) and 1101 nm ($E_0 = 20\,\text{keV}$).

4.3.2 Electron Back Scatter Diffraction (EBSD)

In addition, the SEM is equipped with an EBSD-detector. This technique is a powerful method to link the local microstructure to the crystallography of a sample, providing a more complete picture of the sample. For example, the texture of nanoparticles on a substrate produced by SSD can be investigated by determining the orientation relationship between the particles and the substrate. For obtaining EBSD pattern in SEM, a highly tilted specimen (∼70°) is illuminated with a stationary electron beam to increase the quality of the pattern. The detector is placed close to the sample and is nearly perpendicular to the electron beam [45].

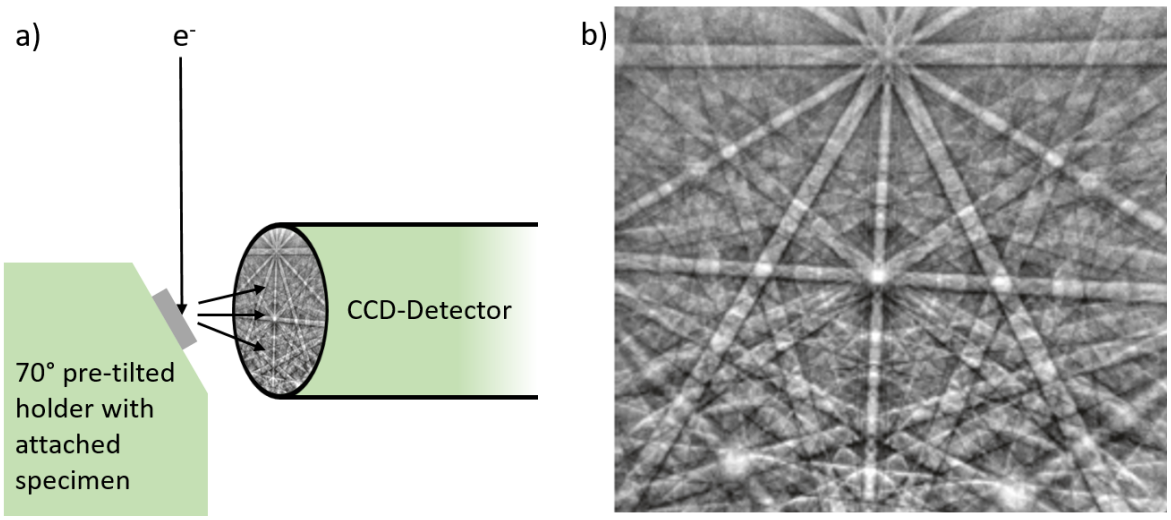

Figure 4.6: a) Schematic drawing of the experimental setup for measuring EBSD-pattern, adapted from [47]: A highly tilted sample is illuminated by the electron beam. The detector recording the pattern is placed close to the sample. b) EBSD pattern of a single-crystalline material, reprinted from [45].

After hitting the sample, the electrons are diffusely scattered and some of those scattered electrons thus satisfy the diffraction condition at certain crystalline planes of the

specimen. Those which are diffracted near the specimen-surface escape the sample and contribute to the EBSD pattern. For each diffraction-plane two intensity cones are produced ($+\theta_B$ and $-\theta_B$), since diffraction occurs for all incident directions of electrons fulfilling the Bragg condition. The cones are quite flat in nature and when they intersect with the detector two nearly straight lines separated by twice the Bragg angle for each set of planes are generated, visible as bands in the EBSD-pattern (see Figure 4.6b). The areas where the bands intersect are called zone axis (ZA). These are specific crystallographic directions within the unit cell of the crystal which are typically the most symmetric ones. Since the angles between the bands and the zone axis are specific for a certain crystal structure, the EBSD pattern can be used for a quantitative analysis of the crystallographic orientation or phase-determination of the specimen [45, 47].

4.3.3 Focused ion beam - milling and deposition

Similar to the SEM, the ions interact with the sample and generate a variety of signals such as secondary ions and electrons which can be used for imaging [48]. Imaging with ions, however, plays only a minor role. Main applications are ion beam induced ablation (milling) and deposition.

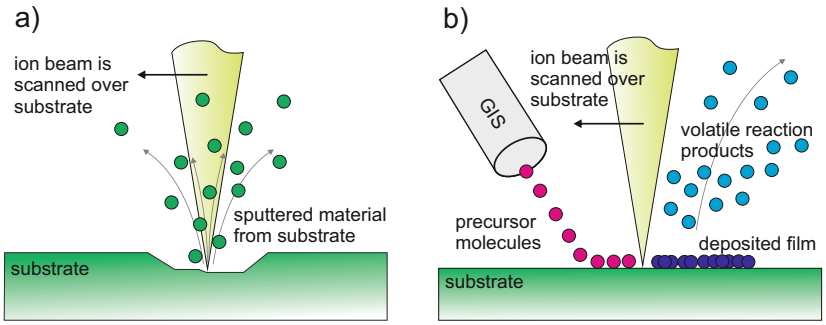

Figure 4.7: Schematic illustration of the working principles of FIB. a) The principle of FIB milling: The ion beam is scanned over the sample and removing the material by physical sputtering; b) The principle of FIB deposition: A CVD based method in which the precursor gas is adsorbed on the sample surface and then decomposed with the ion beam, resulting in a thin film of the desired reeaction products on the surface while the volatile reaction products are removed through the vacuum system [49].

FIB milling is based on physical sputtering (see Figure 4.7 a) where the etching rate depends on the ion beam current. Using a 15 position aperture strip, the current is adjustable from 0.1 pA to 65 nA. However, during the process redeposition occurs which drastically reduces the etching rate [42, 49]. The schematic of the maskless deposition of materials with the FIB can be seen in Figure 4.7 b). Therefore the organic precursor

gas is sprayed with the gas injection system (GIS) on the surface of the sample and the ion beam is scanned over the area where the material deposition is desired. The secondary electrons generated by the ion-sample interaction have the right energy to crack the precursor gas resulting in the adsorption of the products and the growing of the defined pattern while the volatile reaction products are removed through the vacuum system. Since the impact of the high-energy ions not only leads to sputtering of the material, but also to various undesirable damaging effects, a protective layer is deposited by means of an electron beam (EBID) prior to ion beam-induced deposition (IBID) [41, 48, 49].

4.4 Transmisson electron microscopy (TEM)

Transmission electron microscopy (TEM) is a widely utilized technique for the characterization of materials. In this work, a double-corrected Titan Themis 300 is used for the TEM and scanning transmission microscopical investigations. This chapter gives a brief introduction to the techniques used within this thesis.

4.4.1 Conventional transmission electron microscopy

Generally the illumination system of a TEM is similar to an optical microscope where the beam is transmitted through a thin sample. The resulting image is magnified with lenses and projected onto a screen or detectors. In difference to the optical microscopes, instead of visible light electrons are used for image generation enabling a much higher resolution owing to the smaller wavelength. The electrons are emitted by an electron gun. In contrast to the past where often thermionic emitter like tungsten were used, the usage of field-emission guns (FEG), where a strong electric field enables electrons to leave the gun by tunneling effects, is more common in modern microscopes. The emitted electrons are then accelerated with a high tension (up to 300 keV) down a high vacuum column passing several lenses controlling the shape, size and position of the beam. After passing the sample there is another set of lenses before the electrons hit the detector [50].

Figure 4.8 shows the two most common modes used in TEM analysis. In imaging mode (Figure 4.8b) the current of the intermediate lens is adjusted so that its object plane is the image plane of the objective lens, allowing the projection of an image of the specimen onto the screen/detectors. Without the usage of apertures, the contrast of the image is determined by the mass-thickness of the specimen, where thicker and

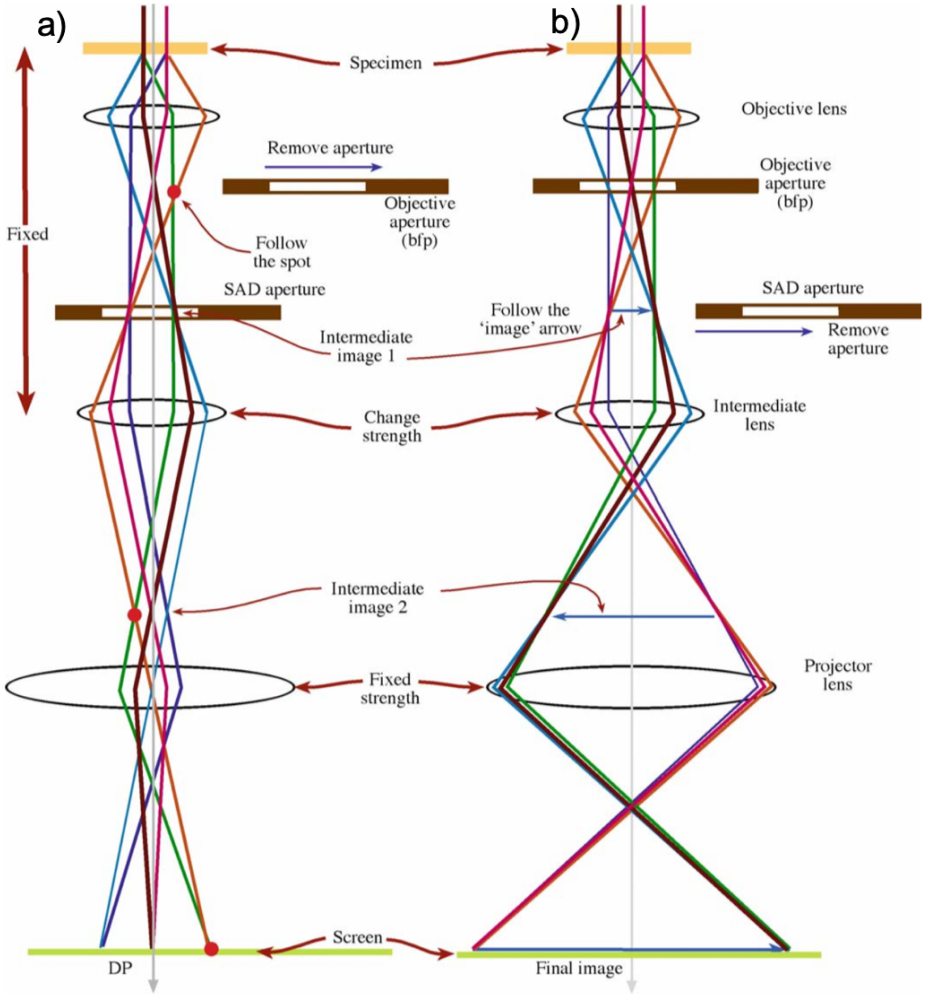

Figure 4.8: After-specimen beam path for the diffraction mode (left) and the imaging mode (right) of a TEM, reprinted from Williams and Carter [50].

areas of high Z-materials appear darker. Using an objective aperture, which is located in the back focal plane (BFP) of the objective lens, also bright field (BF) and dark field (DF) images can be generated by only using the direct beam or a diffracted beam for imaging. Taking BF- and DF-images, specific crystallographic information can be obtained [50].

In diffraction mode (Figure 4.8a) the imaging system lenses are adjusted so that the BFP of the objective lens is acting as the object plane for the intermediate lens. As a result a diffraction pattern (DP) is projected on the viewing screen/detector. Using a selected-area diffraction (SAD) aperture (located in the image plane of the objective lens), the region on the specimen from which the DP is formed can be defined. The formation of DPs is discussed in more detail in the following subsection.

4.4.2 Diffraction

Diffraction is a powerful technique to characterize crystal structures. For a single-crystalline material, the diffraction pattern consists of points each corresponding to a set of crystal planes $(h\,k\,l)$. Constructive interference, e.g. the rise of a diffraction spot in reciprocal space can be described by the *Laue condition* [51]:

$$\boldsymbol{Q} = \boldsymbol{k'} - \boldsymbol{k_0} = \boldsymbol{g_{hkl}} \tag{4.2}$$

with $\boldsymbol{Q}$ as scattering vector, $\boldsymbol{k'}$ as scattered wave vector, $\boldsymbol{k_0}$ as incident wave vector and $\boldsymbol{g_{hkl}}$ as the reciprocal lattice vector.
The basic statement of the *Laue condition* is that constructive interference occurs exactly when the change of the wave vector ($\boldsymbol{Q}$) is equal to a reciprocal lattice vector. This can be illustrated geometrically by the so-called *Ewald sphere construction* (see Figure 4.9). For this, the incident wave vector $\boldsymbol{k_0}$ with a length proportional to $\frac{1}{\lambda}$ is drawn so that it impinges perpendicularly on the origin of the reciprocal lattice. The Ewald sphere is then the sphere around the origin of $\boldsymbol{k_0}$ with a radius of $|\boldsymbol{k_0}|$ and depicts all possible elastically scatterd vectors $\boldsymbol{k'}$. All reciprocal lattice points intersected by the sphere fulfill the *Laue condition* and are visible in the diffraction pattern [50, 51].

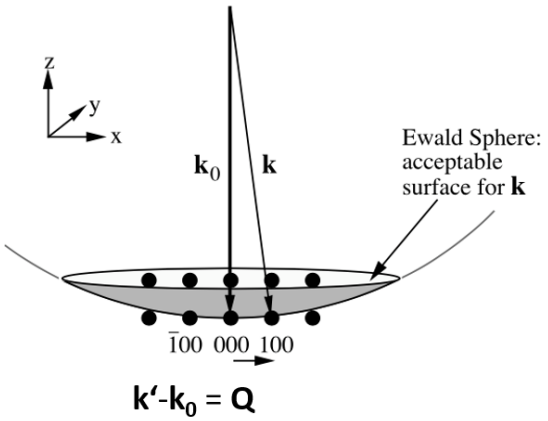

Figure 4.9: Schematic representation of the Ewald sphere construction, reprinted from [51].

4.4.3 Scanning transmission electron microscopy

Another technique used within this work is scanning transmission electron microscopy (STEM). In contrast to CTEM where the sample is illuminated with a parallel beam, a convergent beam is used. Similar to SEM the electron probe is scanned across the specimen. To guarantee homogeneous imaging conditions over the whole scanned area,

the direction of the beam has to be kept constant. The parallel scan of the convergent probe (with respect to the optical axes) is achieved using a double-deflection process done by two pairs of scan coils. As in SEM the magnification is determined by the ratio between the size of the scanned area and the screen size. Due to the absence of lenses for the formation of the image, the resolution is not affected by lense abberations (e.g. chromatic abberation) and only limited by the beam dimensions at the sample position. The arrangement of the detectors for STEM imaging can be seen in Figure 4.10. They are mounted below the specimen and image formation of BF and DF is determined by the range of the electron scattering angle (collection angle). Therefore, the BF detector collects all electrons scattered within 10 mrad with respect to the direct beam. For DF imaging so called annular dark field (ADF) and high-angle annular dark field (HAADF) detectors are used, typically covering angles larger than 10 mrad (ADF) and 50 mrad (HAADF) [50].

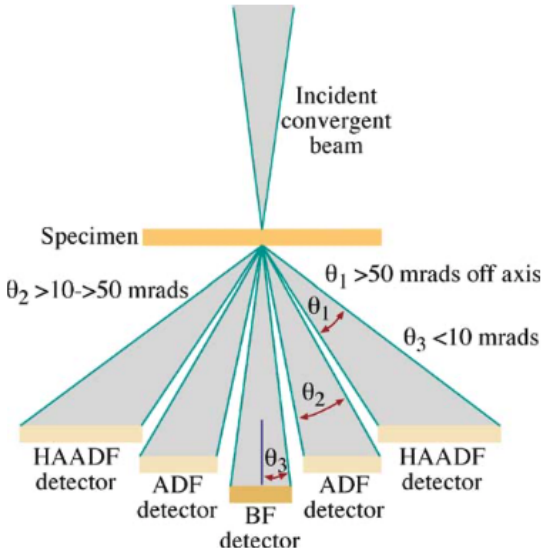

Figure 4.10: Schematic visualization of the position of annular STEM detectors, reprinted from Williams and Carter [50].

4.5 X-ray diffraction (XRD)

X-ray diffraction (XRD) is a powerful non-destructive technique for characterizing crystalline materials, as it allows unambiguous identification of crystalline phases and their structural properties such as strain, grain and particle size, and preferred orientation [52]. In the following, the basics of X-ray diffraction and the different measurement methods used in this work to characterize the nanoparticles are explained in more

detail.

In this thesis, a Rigaku SmartLab is used with a Cu-Kα cathode ($\lambda = 1.541\,\text{Å}$). For all measurements the X-rays are monochromatized with a parabolic multilayer mirror. For the in-plane measurements additionally parallel-slit collimators are used to further decrease the divergence of the X-ray beam.

4.5.1 Principles of X-ray diffraction

When electromagnetic radiation impinges on periodic structures whose geometrical variations are of the same magnitude as the wavelength, diffraction occurs [53].

A condition to describe the intensity of diffracted X-rays related to the angle between the diffracted beam and the solid is given by *Bragg's law*.

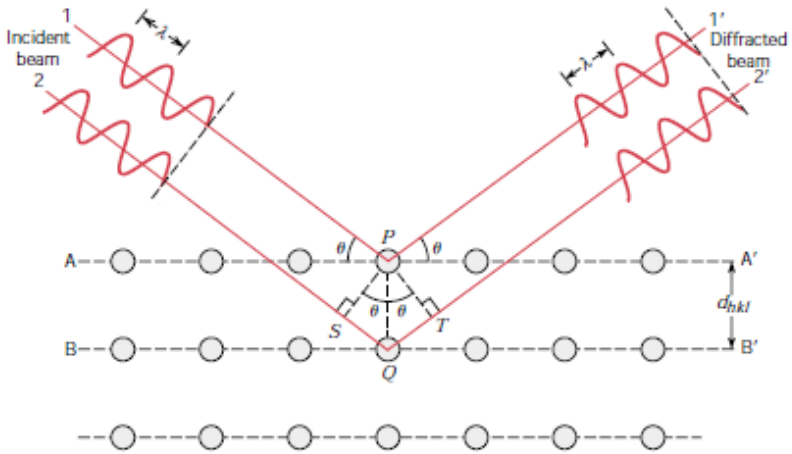

Figure 4.11: Shematic visualization of the diffraction of X-rays by crystallographic planes, reprinted from [54].

Assume that monochromatic, coherent X-rays with wavelength λ impinge under a certain angle θ on a crystal with parallel planes A-A' and B-B' which have an interplanar distance of d_{hkl} (see Figure 4.11). Two waves of the beam are scattered by the atoms P and Q in such a way that they leave the crystal at the same angle θ again. Constructive interference occurs when the two scattered waves have the same phase. This is exactly the case if the path difference between the two waves is equal to a multiple of the wavelength. With this and with some geometric relationships the *Bragg law*, which is equivalent to the *Laue equation* (see Equation 4.2), is derived as [54]:

$$\lambda = 2d_{hkl} \cdot sin(\theta_{hkl}) \tag{4.3}$$

By correlating the diffraction angle with the interplanar distances d_{hkl}, XRD can be used to determine the orientation as well as the lattice parameter of the investigated sample. Based on a cubic crystal, the lattice parameters can be determined using the data obtained by X-ray diffraction as follows:

$$d_{hkl} = \frac{\lambda}{2 \cdot sin(\theta_{hkl})} = \frac{a}{\sqrt{h^2 + k^2 + l^2}} \Leftrightarrow a = \frac{\lambda \cdot \sqrt{h^2 + k^2 + l^2}}{2 \cdot sin(\theta_{hkl})} \tag{4.4}$$

Bragg's law is a necessary but not sufficient condition for the diffraction from real crystals, since the crystal structure has a huge influence on the intensities of the diffracted beams. If the unit cell of the crystal contains more than one atom, the so-called structure factor must be taken into account to describe the intensity of the diffracted X-rays.

$$F_{hkl} = \sum_{n=1}^{N} f_n \cdot \exp\left[2\pi i(hx_n + ky_n + lz_n)\right] \tag{4.5}$$

where f_n is the atomic scattering factor and $2\pi(hx_n + ky_n + lz_n)$ the phase angle of the nth atom in the crystal with fractional coordinates $(x_n y_n z_n)$. The consideration of the structure factor leads to the fact that with the diffraction at cubic face-centered (fcc) materials only reflexes are visible where h,k and l are either all even or odd [55].

4.5.2 Out-of-plane XRD

Out-of-plane measurements are most widely used in X-ray crystallography and are performed in the Bragg-Bretano (BB) geometry, which is why this technique is generally known as $\theta/2\theta$-diffractometry [52].

Figure 4.12 visualizes the working principle of a $\theta/2\theta$ scan. The sample is positioned in the center of the instrument and the X-ray source and the detector are directed to the sample surface at an angle θ. To obtain an XRD-pattern the sample is probed by the X-ray beam over a previously defined angular range. Over the whole measurement the angle of the incoming and scattered beam remain equal ($\theta_{in} = \theta_{out}$). To understand why an X-ray diffractogram is always represented as a function of I(2θ), the scan must be understood as a variation of the exit angle with respect to the extended incident beam, which is for all measurement points 2θ. Since in this measurement method the scattering vector $\boldsymbol{Q}$ is always parallel to the surface normal ($\boldsymbol{s_3}$), only the lattice planes $(h\,k\,l)$ oriented parallel to the surface can fulfill the Bragg condition. This is also the reason why this measurement method is called out-of-plane XRD because the lattice planes aligned parallel to the surface are probed [53, 56].

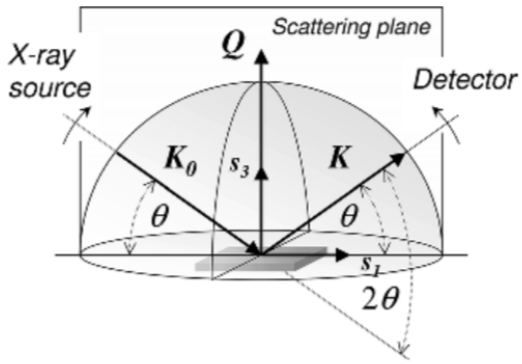

Figure 4.12: Shematic representation of a $\theta/2\theta$ scan, reprinted from Birkholtz et al. [53].

4.5.3 In-plane XRD

To provide a full picture of the texturing of thin films or nanoparticles attached on a substrate, it is necessary to perform in-plane measurements in addition to the out-of-plane measurements.
The schematic of an in-plane XRD measurement could be seen in Figure 4.13. First a parallel incident X-ray beam which is collimated in horizontal and vertical directions is required. To study the lateral structure of a film, respectively performing in-plane diffraction, X-rays may only penetrate a few nanometers into the film so that an X-ray wave is created that is parallel to the surface. Therefore, the X-rays have to impinge on the specimen at an angle below the critical angle, which is in our case (sapphire substrate, Cu K_α irradiation) equal to 0.27°. The generated evanescent wave propagates along the surface of the substrate and can then be diffracted by a set of crystal planes perpendicular to the sample surface. In this geometry, the scattering vector $\boldsymbol{Q}$ is always parallel to the film surface and changes its direction in-plane with the scanning of $\varphi/2\theta_\chi$, making it possible to measure directly the lateral crystal-structure parameters like film orientation, lattice constants etc [57].

Before the actual measurement can be started, a so-called φ-scan is carried out to orient the sample. For this purpose, $2\theta_\chi$ is set to the value of the $(3\,0\,\overline{3}\,0)$-peak of α-Al_2O_3. The sample is then rotated around φ until the diffraction peak is detected. Then the actual measurement takes place by a small variation of the angular range (about ±10° $2\theta_\chi$) around the $(3\,0\,\overline{3}\,0)$ α-Al_2O_3 reflection.

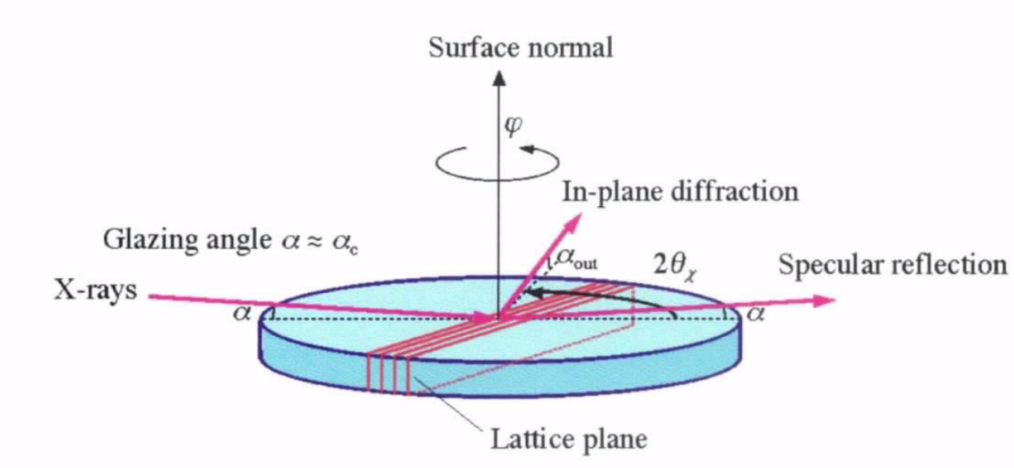

Figure 4.13: Shematic representation for X-ray in-plane diffraction, reprinted from Omote et al. [57]. The X-rays impinge on the sample at a grazing angle (0.27°) and are diffracted by a set of crystal planes perpendicular to the sample surface.

4.5.4 Pole figures

In contrast to the previously introduced XRD methods, pole figure measurements are an XRD method in which the diffraction angle 2θ is fixed. The diffracted intensity is collected by varying the tilt angle α and the rotation angle β. By rocking the sample with a fixed scattering vector ($\boldsymbol{Q}$), the trajectory of the end of $\boldsymbol{Q}$ will trace out a sphere (Figure 4.14a). For evaluation the data is plotted on a stereoscopic projection with polar coordinates α and β (Figure 4.14b) [58].

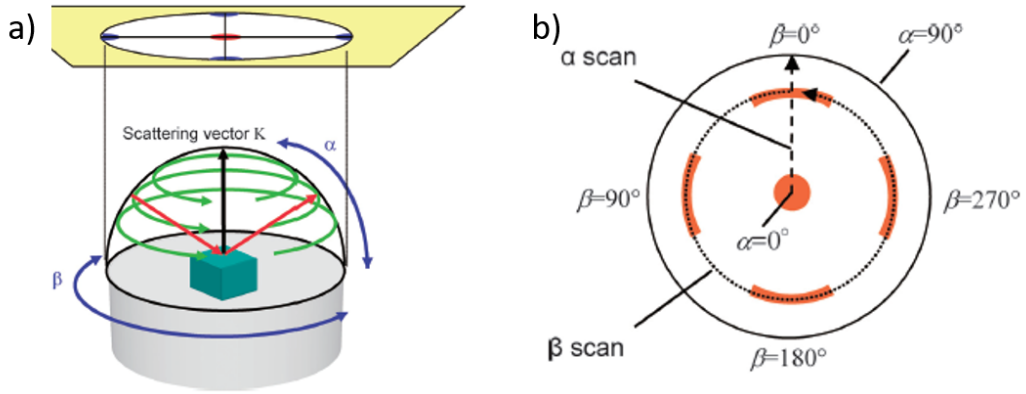

Figure 4.14: Schematic representation of XRD pole figure measurements. a) Sphere obtained by rocking the sample with fixed scattering vector. b) Stereoscopic projection of the measured intensity, showing the definition of α and β, reprinted from Nagao et al. [58].

In this thesis, the in-plane arm of the Rigaku Smart Lab is used to measure the pole figures. Therefore the β-scan is done with a φ-rotation at each α-angle, while α (tilt angle of the sample) is controlled by the combination of 2θ and $2\theta_\chi$ (Figure 4.15a-

c). The usage of the in-plane arm for measuring pole figures has two advantages in comparison with other methods (e.g. Schulz reflection method), since a complete pole figure from $\alpha = 0°$ to 90° can be recorded and it is not required to tilt the sample [58].

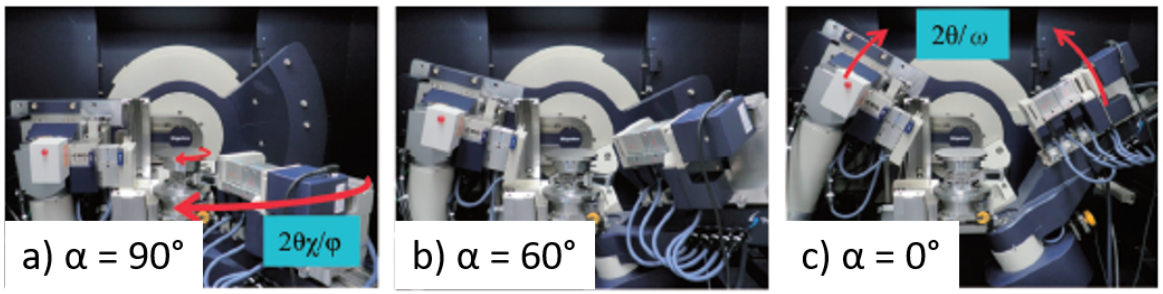

Figure 4.15: Visualization of the movement of the goniometer in in-plane pole-figure measurements from $\alpha = 90°$ to 0°, reprinted from Nagao et al. [58].

Considering the measurement of e.g. $\{1\,1\,1\}$ pole figures of faceted metallic nanoparticles showing a $\{1\,1\,1\}$-out-of-plane orientation, the central peak at $\alpha = 0$ would be related to the $\{1\,1\,1\}$ planes since they are parallel to the surface. By scanning the whole hemisphere also the $\{1\,1\,1\}$ planes inclined to the surface plane show up in the stereoscopic projection under a certain angle α, which can be determined as follows:

$$\cos(\alpha) = \frac{\mathbf{a} \cdot \mathbf{b}}{|\mathbf{a}||\mathbf{b}|} \tag{4.6}$$

where $\mathbf{a}$ and $\mathbf{b}$ are the normal vectors of two different lattice planes and $|\mathbf{a}|$ and $|\mathbf{b}|$ their absolute values. For the example mentioned above, α is calculated to 70.52°.

4.6 Sample preparation and precalculations

In the following, the details of sample preparation including the expected Au content for lattice matching and the relationship between individual layer thickness and Au content are summarized.

4.6.1 Determination of the Au-content for lattice-matching

The aim of the work is to investigate the influence of the Au-content on the dewetting behaviour of Au/Ni-bilayer, including the special case of a lattice matching of the Au/Ni alloy and the sapphire substrate. Previous research has shown that for a lattice matching, the d-spacing of the $\{2\,2\,0\}$-planes of Ni must correspond to that of the $\{3\,\bar{3}\,0\,0\}$-planes of sapphire [59]. With a d-spacing of sapphire of $d_{3\bar{3}00} = 1.375\,\text{Å}$ and

the formula for the lattice parameter of cubic systems (see Equation 4.4) the estimated lattice parameter for the Au/Ni-alloy is 3.89 Å.
Figure 4.16 shows the lattice parameter as a function of the Au concentration. To determine the required concentration of Au, previous data [59] were linearly extrapolated (green line). In addition, the lattice parameters for Au/Ni bulk alloys were taken into account (purple line) [60] and the lattice parameters at room temperature of a substitutional solid solution were determined with Vegard's law (blue line) [61, 62]:

$$a_{NiAu} = x_{Ni} \cdot a_{Ni} + (1 - x_{Ni}) \cdot a_{Au} \tag{4.7}$$

where a_{NiAu} is the lattice parameter of the Au/Ni solid solution, a_{Ni} the lattice parameter of nickel, a_{Au} the lattice parameters of gold and x_{Ni} the percentage of nickel. For a lattice parameter of $a = 3.89$ Å the atomic percentage of Au is estimated to:

- linear interpolation out-of-plane: ~ 46 at.%
- quadratic interpolation Bulk: ~ 59 at.%
- linear dependence of the lattice constant according to Vegard: ~ 66 at.%

Based on these values, a lattice matching in a concentration range of 45 at.% to 60 at.% can be expected, which is the reason for relatively fine increments in the gold concentrations in this range.

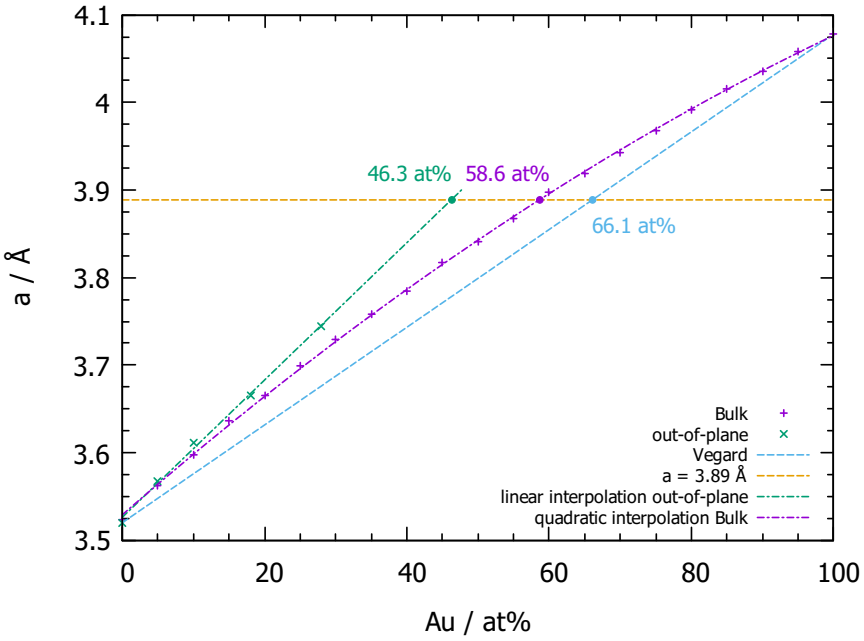

Figure 4.16: Influence of the Au-ratio of Au/Ni-alloys on the lattice parameter. The data for Bulk is from Crawley et al. [60] and the out-of-plane measurements from previous work done by J. Will and P. Herre [59]. The orange line indicates a lattice parameter of 3.89 Å needed for lattice-matching.

4.6.2 Layer deposition and calculation of the layer thicknesses

The Au/Ni bilayer films are deposited on the substrates via E-Beam PVD (for details see Section 4.2). Quadratic (0 0 0 1)-oriented α-Al_2O_3-wafer of size 5 mm × 5 mm × 0.5 mm (CrysTec Kristalltechnologie) are used as a substrate. Before the deposition of the bilayers, the wafers are subjected to different cleaning steps. First the wafers are cleaned in an ultrasonic bath with acetone, followed by a rinsing in isopropyl and ethanol. Second, a plasma cleaning process is used, whereby the wafers are treated with an Ar/O_2 (3:1) plasma for 2 min (Binder Labortechnik Plasma Cleaner TPS 316). Figure 4.17 schematically shows the arrangement of the bilayer system. To prevent oxidation the Au layer is deposited over the Ni layer. The total thickness of all films is 40 nm. The variation of the Au content is controlled by the thickness of the Au layer. In a first step, the volume percentage is calculated from the desired atomic percentage of gold as follows:

$$\text{vol.}\%_{Au} = \left(1 + \frac{\text{at.}\%_{Ni} \cdot m_{Ni} \cdot \rho_{Au}}{\text{at.}\%_{Au} \cdot m_{Au} \cdot \rho_{Ni}}\right) \tag{4.8}$$

where $\text{at.}\%_x$ is the atomic percent, m_x the atomic weight and ρ_x the density of the corresponding element.

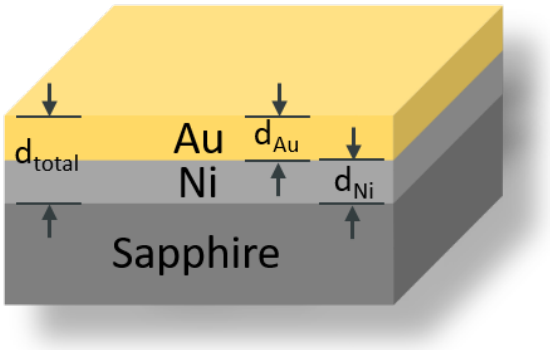

Figure 4.17: Schematic representation of the as-deposited Au/Ni bilayers on (0 0 0 1)-oriented Sapphire-wafer. The total thickness of all samples is 40 nm and the variation of the Au content is controlled by d_{Au}. In order to prevent oxidation, the Au layer is on top the Ni layer.

The associated film thickness is then calculated as:

$$d_{Au} = \text{vol.}\%_{Au} \cdot d_{total} \tag{4.9}$$

where $\text{vol.}\%_{Au}$ is the volume percentage of Au and d_{total} the total film thickness.
To continue the measurement series of J. Will and P. Herre [59], two measurement series are fabricated (ERL and ILM), where the Au concentration variations are performed as displayed in Table 4.1 and Table 4.2.

Table 4.1: Variation of the gold content of the bilayer layers and the resulting layer thicknesses for the measurement series ERL.

$\text{at.}\%_{Au}$	$\text{at.}\%_{Ni}$	d_{Au} / nm	d_{Ni} / nm
0	100	0	40
15	85	8.6	31.4
28	72	15	25
41	59	20.7	19.3
43	57	21.6	18.4
45	55	22.4	17.6
47	53	23.2	16.8
49	51	23.9	16.1
55	45	26.2	13.8
70	30	31.3	8.7
85	15	35.9	4.1
100	0	40	0

Table 4.2: Variation of the gold content of the bilayer layers and the resulting layer thicknesses for the measurement series ILM.

$at.\%_{Au}$	$at.\%_{Ni}$	d_{Au} / nm	d_{Ni} / nm
28	72	15	25
35	65	18.2	21.8
40	60	20.3	19.7
45	55	22.4	17.6
50	50	24.3	15.7
52.5	47.5	25.3	14.7
55	45	26.2	13.8
57.5	42.5	27.1	12.9
60	40	28	12.0
62.5	37.5	28.8	11.2

4.6.3 Thermal treatment

For thermal processing of the samples rapid thermal annealing (RTA) with the AS-ONE 100 furnace from ANNEALSYS (see Figure 4.18 a) is carried out. First, a parameter study is done to determine the cooling rates of the furnace and to find the appropriate parameters for the production of AuNi nanoparticles. To obtain Au/Ni particles using SSD, the samples are equilibrated for 120 s at 935 °C above the miscibility gap (see Figure 4.1). In order to avoid phase separation and precipitation during cooling, the samples are quenched using the fast-cooling option with cooling rates of around 200 °C s^{-1} (see Figure 4.18 c). During heating a gas-flow of 400 sccm Ar and 20 sccm H_2 (ratio of 20:1) is set.

For a second measurement series samples are also thermally processed at the TU Ilmenau in a Jipelec Jetstar 100 furnace (Semco, France). The heating is performed at 935 °C above the miscibility gap of the Au-Ni system for 120 s (same temperature and time as ERL) followed by a fast cooling. Although the maximum achievable cooling rate, as determined earlier by Herz et al. [25], is with 9 °C s^{-1} significant lower, the maximum gas flow rates of 2000 sccm for Ar and 100 sccm H_2 (same ratio) are a factor of five higher. Thus, segregation during cooling but also a higher degree of texturing are expected for the ILM series. In the future the advantage of a fast cooling and a high gas flow should be exploited, which was not possible with the existing instrumentation configuration available during this thesis.

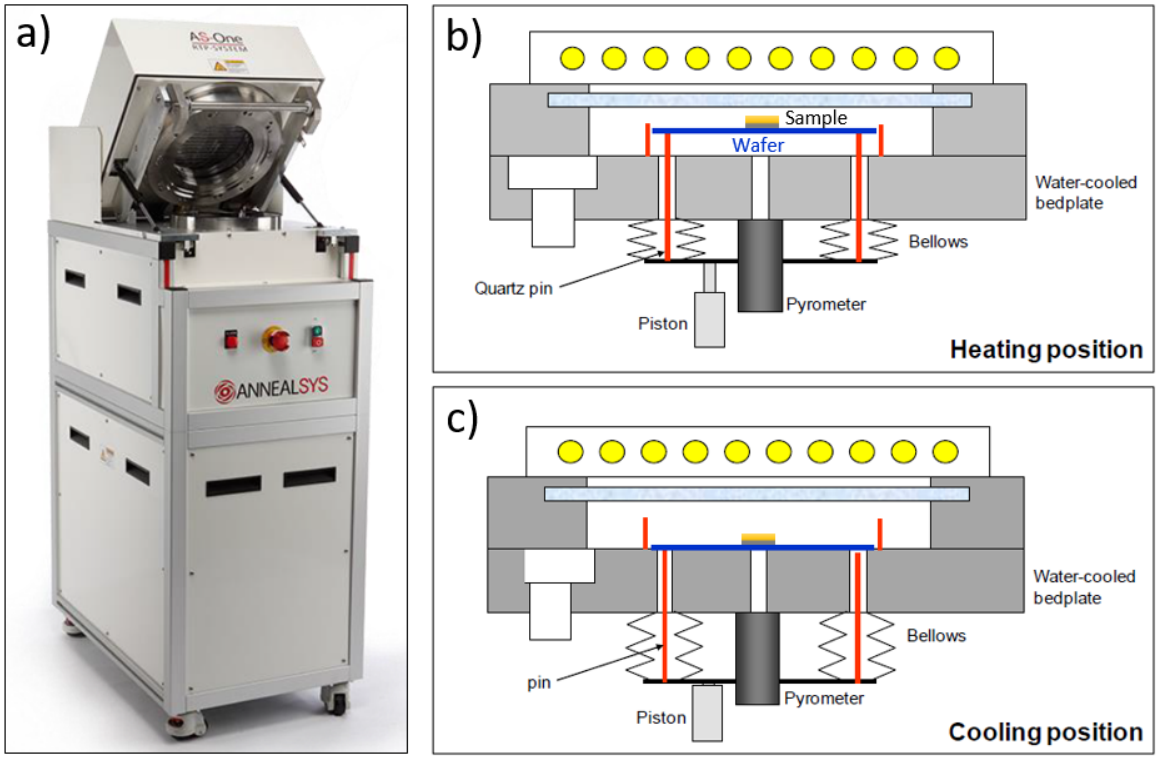

Figure 4.18: a) AS-ONE 100 RTA furnace from ANNEALSYS, reprinted from [63]. b) Schematic cross-section of the heating chamber during the heating process. The samples are placed on a Si wafer which is supported by quartz pins. c) In order to achieve quenching of the samples, rapid cooling takes place after heating. Therefore, the quartz pins move to the lower position, so that the wafer rests on the water-cooled bed plate, adapted from [64].

4.6.4 FIB lamella preparation

To check the relative lattice parameter, the orientation of the particles with respect to that of the substrate and to investigate the particle-substrate interface in more detail, a plan-view lamella is prepared via FIB-milling. The EBSD pole figures reveal that the two marked particles are two twin variants of an orientation relation $\{1\,1\,1\}\ \langle 1\,1\,0\rangle$ AuNi $\parallel (0\,0\,0\,1)\langle 1\,0\,\bar{1}\,0\rangle$ α-Al_2O_3 (see Figure 4.19).

After checking the NPs for the right orientation sample is brought to the eucentric height. This is a necessary step to ensure that the selected sample location is not lost during tilting and that the electron beam and ion beam are focused on the same sample location. Before milling, a protective carbon layer is deposited on top of the NPs to avoid ion beam induced damage. This is done in two steps: first a thin layer is deposited via EBID to decrease the implantation of ions in the NPs. Afterwards the actual protection layer ($7\,\mu m \times 3\,\mu m \times 0.8\,\mu m$) is deposited via IBID.

The sample is then tilted by 52° and a large area is cut free around the area of the lamella using the *Cleaning Cross-Section* tool (acceleration voltage: 30 kV, current:

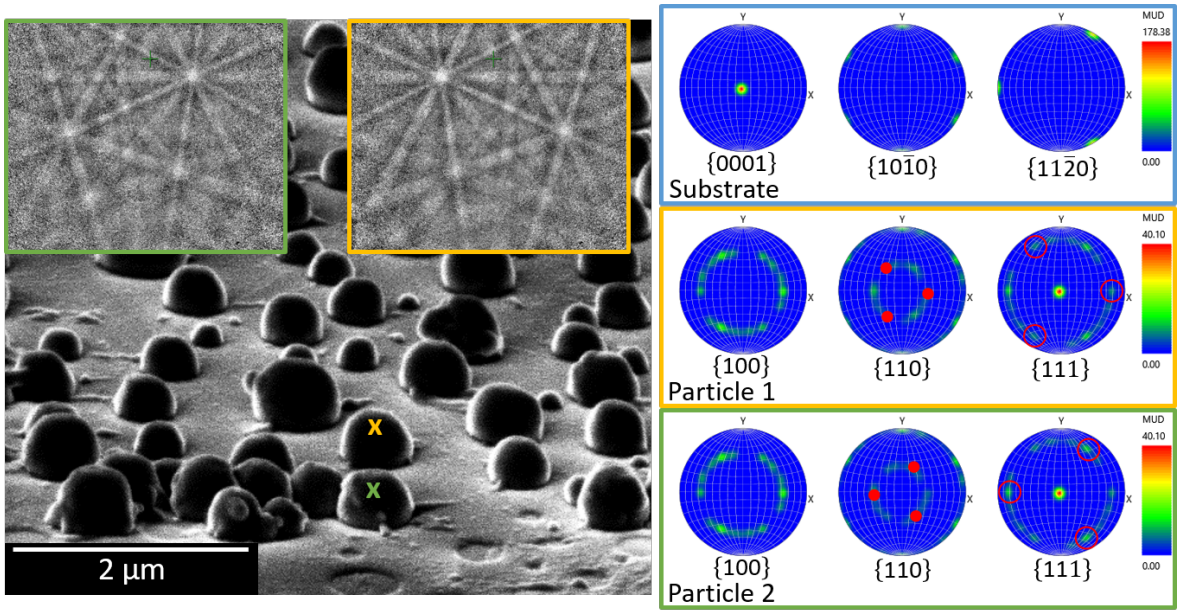

Figure 4.19: EBSD pattern of the two AuNi NPs included in the plan-view lamella. The pole-figures clearly confirm the orientation relationship $\{1\,1\,1\}\ \langle 1\,1\,0\rangle$ AuNi $\parallel (0\,0\,0\,1)\langle 1\,0\,\bar{1}\,0\rangle$ α-Al_2O_3 of the NPs and the substrate.

0.43 nA) (see Figure 4.20a). The sample is then tilted back to 0° and after attaching the *EasyLift* micromanipulator tip the lamella is completely cut free and transferred to a vertical oriented TEM grid (Figure 4.20b). The sides of the lamella are then cleaned by one-time milling to see the particle-substrate interface. So far this is a standard procedure producing thin cross-sectional lamellas via FIB-milling. To produce a plan-view lamella, thus thinning from the top and the bottom side, the lamella has to be rotated by 90°. This is done by dismounting the lamella and reattaching it at the TEM grid after the grid is mounted in the sample holder horizontally. For better stability, the lamella is attached on both sides (Figure 4.20c) on the grid which is realized by first milling a V-cut into the grid-finger.

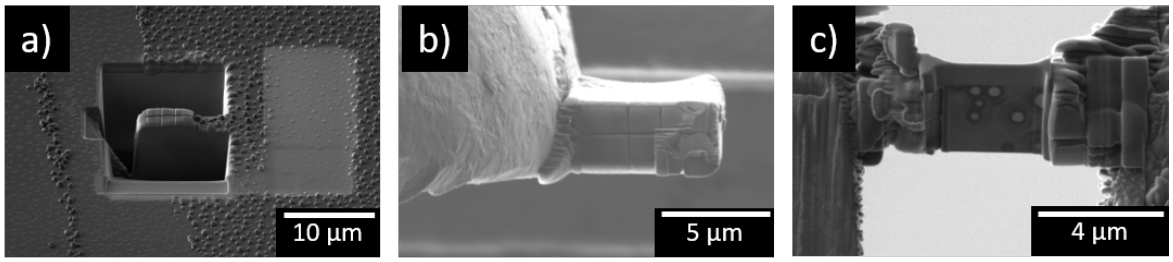

Figure 4.20: a) Generously cut free lamella area. b) Lamella attached on a vertical grid for cleaning the sides, making the interface visible. c) Final attachment of the lamella in a V-cut, horizontal grid.

Finally the lamella has to be thinned from both sides, making it electron transparent for the TEM studies. Down to a thickness of about 500 nm milling is done with 30 kV and 0.23 nA at a tilt angle of 52°. From 500 nm to 200 nm thinning takes place with 16 kV and 0.15 nA. Therefore the sample is over-tilted by ±0.5°. To further decrease the depth of FIB-damage 8 kV and 66 pA are used for the thinning down to about 130 nm (over-tilt ±3°). The final thinning is done at 5 kV/66 pA and an over-tilt of ±4.5° until a final thickness of about 120 nm is reached. Lastly, the lamella is showered on both sides with 2 kV/23 pA for 5 min each.

After first investigations showed that the lamella is still slightly too thick and the surface is damaged by FIB, the lamella was additionally polished with low energy Ar ions (< 2 keV) for 5 min using the *Fischione Model 1040 NanoMill* system.

5 Results

In this chapter the results of all experiments carried out are listed. It starts with parameter studies to determine sufficient cooling rates and optimal conditions for the production of AuNi nanoparticles. Subsequently, the electron microscopic and XRD investigations of the two measurement series ERL and ILM are described.

5.1 Parameter study for the RTA furnace

One decisive factor for the production of AuNi-particles is a high cooling rate. A parameter study was carried out to quantify the cooling rate in Erlangen. For this study all samples had the same composition with layer thicknesses of 15 nm Au and 25 nm Ni.

5.1.1 Heating and fast cooling in vaccuum

In a first experiment the heating and cooling of the Au/Ni bilayer was carried out in a vacuum of 1×10^{-4} mbar. Two different heating experiments were performed, a one-step heating in which the samples were equilibrated at 950 °C for two minutes (Figure 5.1 a, b, c) and a two-step heating in which they were equilibrated at 950 °C for one minute and at 820 °C for another minute (Figure 5.1 d, e, f).
In Figure 5.1 a) and d) the temperature profiles during cooling are displayed. The cooling rate was determined by linearly fitting the curve in the fast-cooling range and is (36.1 ± 1.2) °C/s for the one-step heating cycle and (35.1 ± 0.7) °C/s for the two-step heating cycle. Figure 5.1 b) and e) show SEM images of the rapid thermal treated samples. In both cases, the bilayer films are completely dewetted and spherical particles have formed which clearly show an Au-rich phase (bright) and a Ni-rich phase (dark). It is noticeable that in the one-step heated sample the Au-rich phase is much more pronounced than the Ni-rich phase, whereas in the two-step heated sample the phase fraction of both phases is inverted. The one-step treated sample shows a monomodal distribution with a mean particle radius of (167 ± 56) nm (Figure 5.1 c). The two-step processed sample has a bimodal particle distribution with mean radii of (56 ± 32) nm for the small particles and (210 ± 36) nm for the bigger particles (Figure 5.1 f).

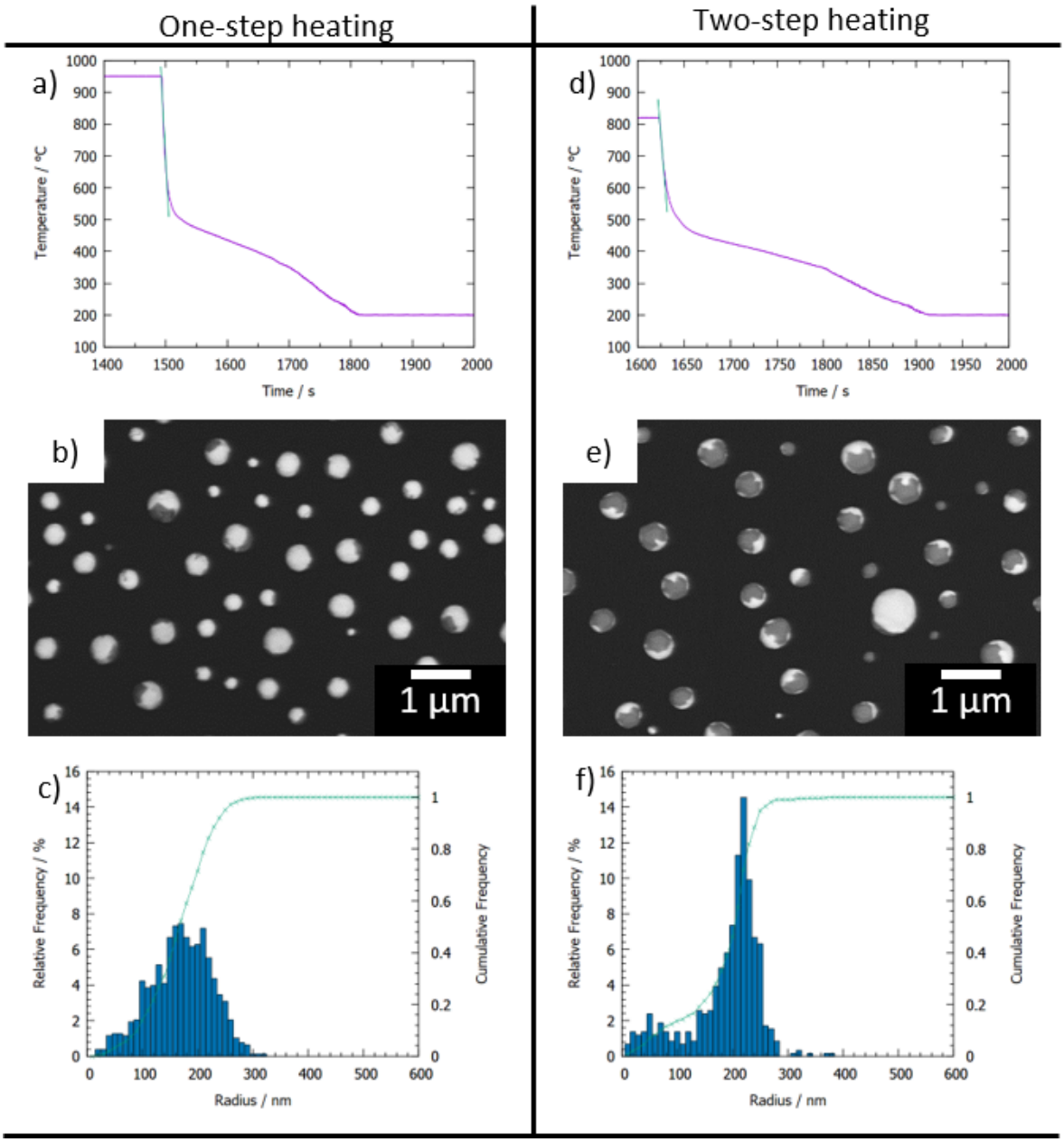

Figure 5.1: One-step (a,b,c) and two-step (d,e,f) heat treatments at 950 °C in vacuum. The temperature reduction before the fast-cooling has no influence on the cooling rate (a,d). The BSE images clearly show that the alloy formation wasn't succesful (b,e). The particle size distribution can be found in c and f: The one-step treated sample shows a monomodal size distribution with a mean particle radius of 167 nm. The two-step treated sample shows a bimodal size distribution with a mean particle radius of 210 nm (large particles) and 56 nm (small particles).

5.1.2 Gas injection for fast cooling

In an attempt to achieve a better cooling rate, a constant Ar gas flow of 400 sccm was set before rapid cooling. For the parameter study blank sapphire wafers were used as dummy samples and were heated for 30 s, 60 s, 90 s and 120 s. The heating profiles are shown in Figure 5.2. The cooling rates were determined by linear fits of the fast-cooling regime and are:

- 30s: $(235 \pm 11)\,°C/s$
- 60s: $(205 \pm 10)\,°C/s$
- 90s: $(208 \pm 2)\,°C/s$
- 120s: $(209 \pm 8)\,°C/s$

According to the profile, for the 30 s sample a direct cooling from 935 °C to 200 °C takes place. As the heating time increases, there is an increase in the temperature to which direct cooling takes place. Thus, with a heating time of 60s the temperature is cooled down to 300 °C, with 90s to 420 °C and with 120s to only 480 °C. It can be assumed that this is a measurement artifact and that in reality the sample is cooled to room temperature in all cases. For a detailed discussion the reader is referred to Section 6.1.

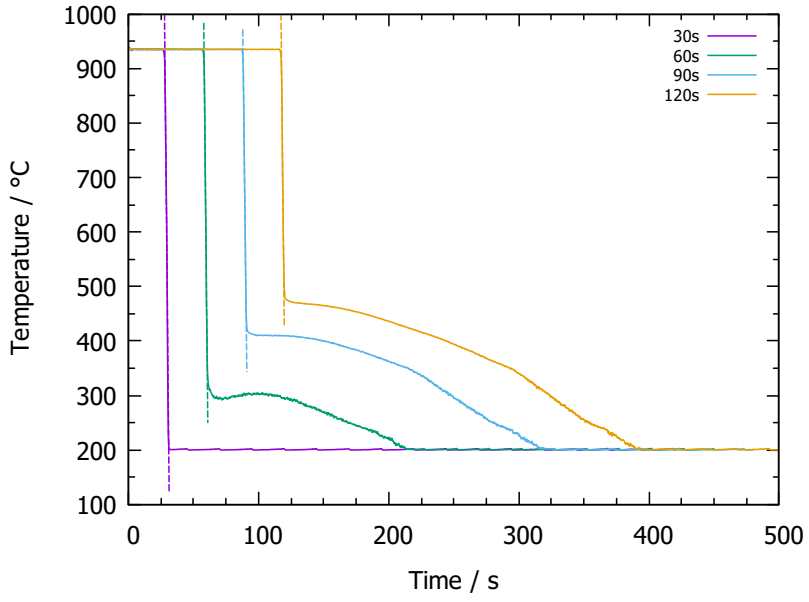

Figure 5.2: Cooling profiles for the dummy sample (blank Sapphire wafer) heated at 935 °C for different times. Before fast-cooling, an Ar gas flow of 400 sccm was set.

5.2 Parameter study for the production of Au/Ni alloy nanoparticles

After a sufficiently high cooling rate has been achieved, the next step is a parameter study regarding the processing. For this purpose, temperature, heating time and atmosphere were varied.

5.2.1 Variation of dewetting temperature and time

In order to achieve the final goal of this work, alloy nanoparticles over a concentration range of 0 at.% to 100 at.% Au, the correct aging temperature and time have to be determined. Since the Au-Ni system has an asymmetric miscibility gap, a temperature must be found which is above the miscibility gap but below the liquidus line over the entire concentration range. In addition, the temperature must be high enough for particle formation to occur. For this purpose, heating tests were carried out at 920 °C and 935 °C for 30 s, 60 s, 90 s and 120 s respectively. Before heating, the process chamber was pumped down to 1×10^{-4} mbar. During heating a continuous gas flow of 500 sccm was set, which was raised to 1000 sccm for fast-cooling. The results of the heating tests are shown in Figure 5.3.
On the left are the samples heated at 920 °C. Already after 30 s the effect of dewetting can be seen clearly, since islands exist instead of a continuous film, but no NPs have formed. While after further 30 s no change of the dewetting state could be observed, at the sample heated for 90 s first isolated nanoparticles can be recognized. After a thermal processing time of 120 s wire-like islands and isolated nanoparticles are present. The BSE contrast indicates that the islands and the nanoparticles are mostly in alloyed condition and only show isolated Ni-rich spots (dark). To get a qualitative impression of the element distribution an EDX-mapping was carried out, which can be seen in Figure 5.4. The mapping confirms the first impression of the BSE images since the homogeneous distribution of Au and Ni is clearly visible and no enrichments of one of the elements could be detected. Also in the triangular shaped dark areas and the dark areas on the edges, no enrichment of Ni could be observed.
The right side of Figure 5.3 shows the samples processed at 935 °C. The rise of the temperature has a significant influence regarding the dewetting state of the Au-Ni system. Already after 30 s the film is completely dewetted and beside isolated wire-like islands mainly nanoparticles have formed. While the nanoparticles which have formed after 30 s and 60 s have a flat surface, the particles formed after 90 s and 120 s are

more round in shape. All particles show crystallographic facets, even if these are not strongly pronounced. According to the Z-contrast of the BSE-images similar to the samples heated at 920 °C an alloying took place but also dark areas, mostly on the side facets of the particles, are visible, indicating the segregation of Ni at the respective areas. By contrast, the EDX-mappings do not show any phase separation and facet-related enrichment of Ni anywhere (see Figure 5.5). As the Ni enriched regions are very small, one reason for not detecting them in the EDX-mappings could be a too large interaction volume of the electrons in the sample (see Section 4.3.1).

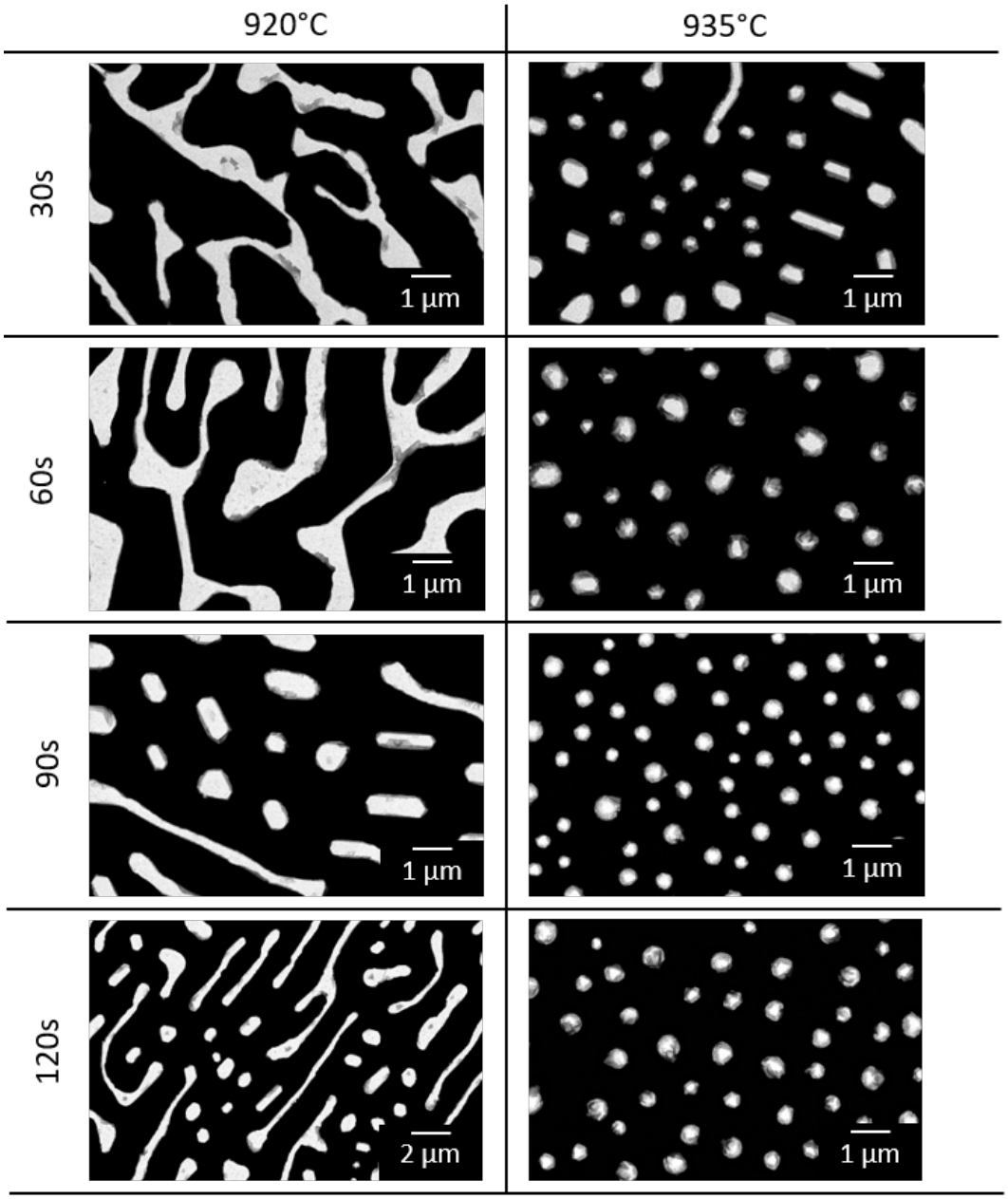

Figure 5.3: Variation of the dewetting temperatur and time.

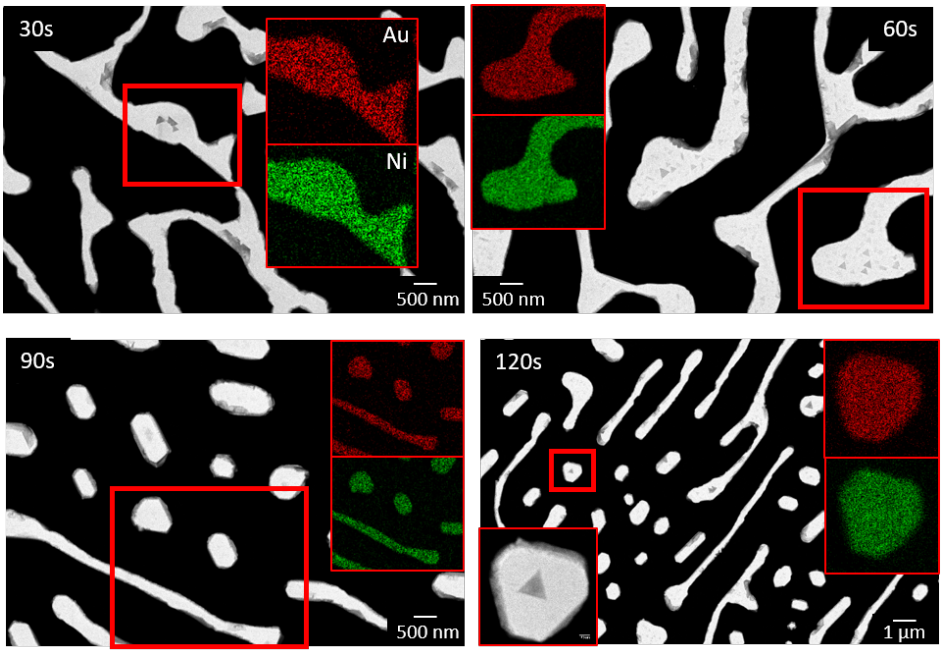

Figure 5.4: BSE-images of the samples heated at 920 °C with qualitative EDX-mappings of the areas marked with the red box. While within the BSE-images triangular dark spots are visible, indicating a Ni-rich area, the elemental mappings show no enrichment of Ni in these areas.

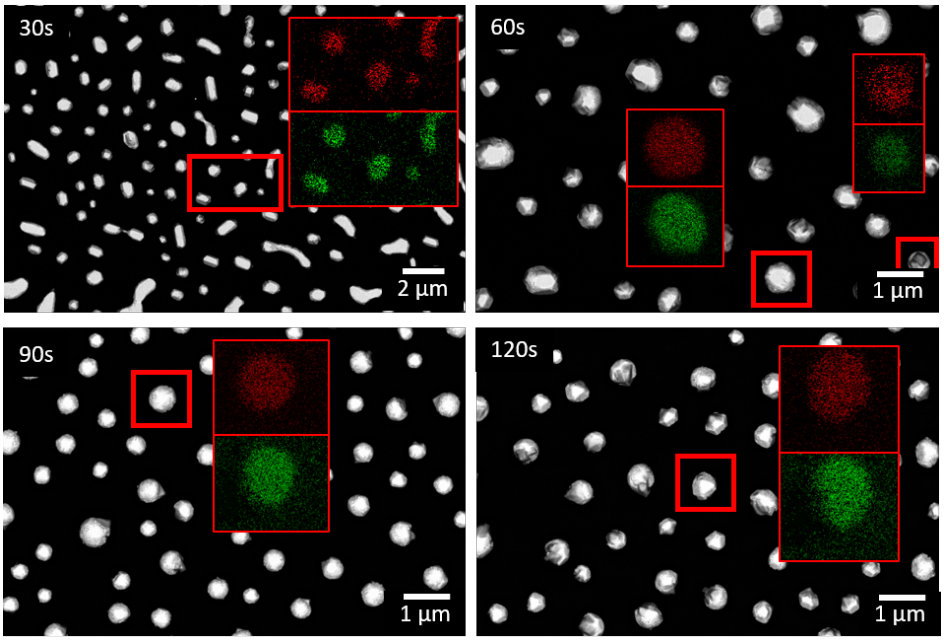

Figure 5.5: Qualitative EDX-analysis of the samples heated at 935 °C for different times. While the BSE-images indicate a segregation of Ni on the side facets, the elemental mappings show no enrichment of Ni.

5.2.2 Influence of the hydrogen content on the alloying process

The previous parameter study has shown that it is possible to produce NPs by processing at 935 °C. However, the particles produced in the vacuum show only a low formation of crystallographic facets, which is why an additional study of the atmosphere during heating was carried out. Therefore bilayers with a nominal concentration of 28 at.% were heated at 935 °C for 30 s, 90 s and 120 s respectively. In contrast to the previous measurement series, the chamber was flooded to atmospheric pressure before heating. During heating the following gas flows were adjusted: 400 sccm of Ar with 20 sccm of H_2 (20:1) and 400 sccm of Ar without H_2. The Ar flow was increased to 1000 sccm for fast cooling.

The results of the electron microscopic investigations can be seen in Figure 5.6. By comparing the images of the samples with and without a gas flow of the reducing agent (H_2) a significant influence of the reducing agent is visible. The samples processed with a flow of H_2 have formed round nanoparticles showing crystallographic facets. Furthermore, no phase decomposition is visible. The situation is slightly different for samples that have been thermally treated without H_2. While at a short heating time of 30 s no visual difference is present for the sample with H_2, the particles with a heating time of 90 s are rather irregularly shaped and have a dark tail, which indicates a phase separation. After 120 s dark "ice cone" shaped regions show up with bright "scoops" on one side. This also indicates a phase separation where the dark "ice cones" should contain Ni and the bright "scoop" are made of gold. An EDX-mapping at the sample processed for 120 s supports this hypothesis since signal from Au (red) only shows up in the "scoop". Nickel, on the other hand, can only be found in the "ice cones". When looking at the oxygen map it is noticeable that besides the substrate oxygen is also contained in the "ice cones", which indicates that the dark "ice cones" are probably nickel oxide.

To clarify which phases are present in the sample, XRD out-of plane measurements were done and are presented in Figure 5.7. According to the diffractogram for the samples processed with H_2 (black line Figure 5.7a-c), AuNi alloy nanoparticles have formed, since sharp peaks at 41.4° (AuNi (1 1 1)) and 48.2° (AuNi (2 0 0)) appear. After 30 s only a small influence of the atmosphere can be detected during the heating process, since both diffractograms are nearly identical independent of the H_2 content. The only difference is a slightly broadened AuNi (2 0 0) peak. As the heating time increases, the influence that the reducing atmosphere has on the process also becomes

more apparent. After 90 s the AuNi (1 1 1) peak, originally at 41.4°, splits into two peaks, a small one with a slight shift of 0.1° to 41.3° and a wider peak with its center at 38.8°. In addition new peaks arise at 37.3° and 43.3° which correspond to the NiO (1 1 1) and NiO (2 0 0) lattice planes. Due to the oxidation of nickel, less nickel is available for alloy formation. This leads to an increase in the lattice parameter which explains the shift of the AuNi peaks to smaller angles. After 120 s of heating without H_2 the Ni has oxidized completely, since the existing peaks are pure gold (Au (1 1 1) at 38.3° and Au (2 0 0) at 44.4°) and NiO.

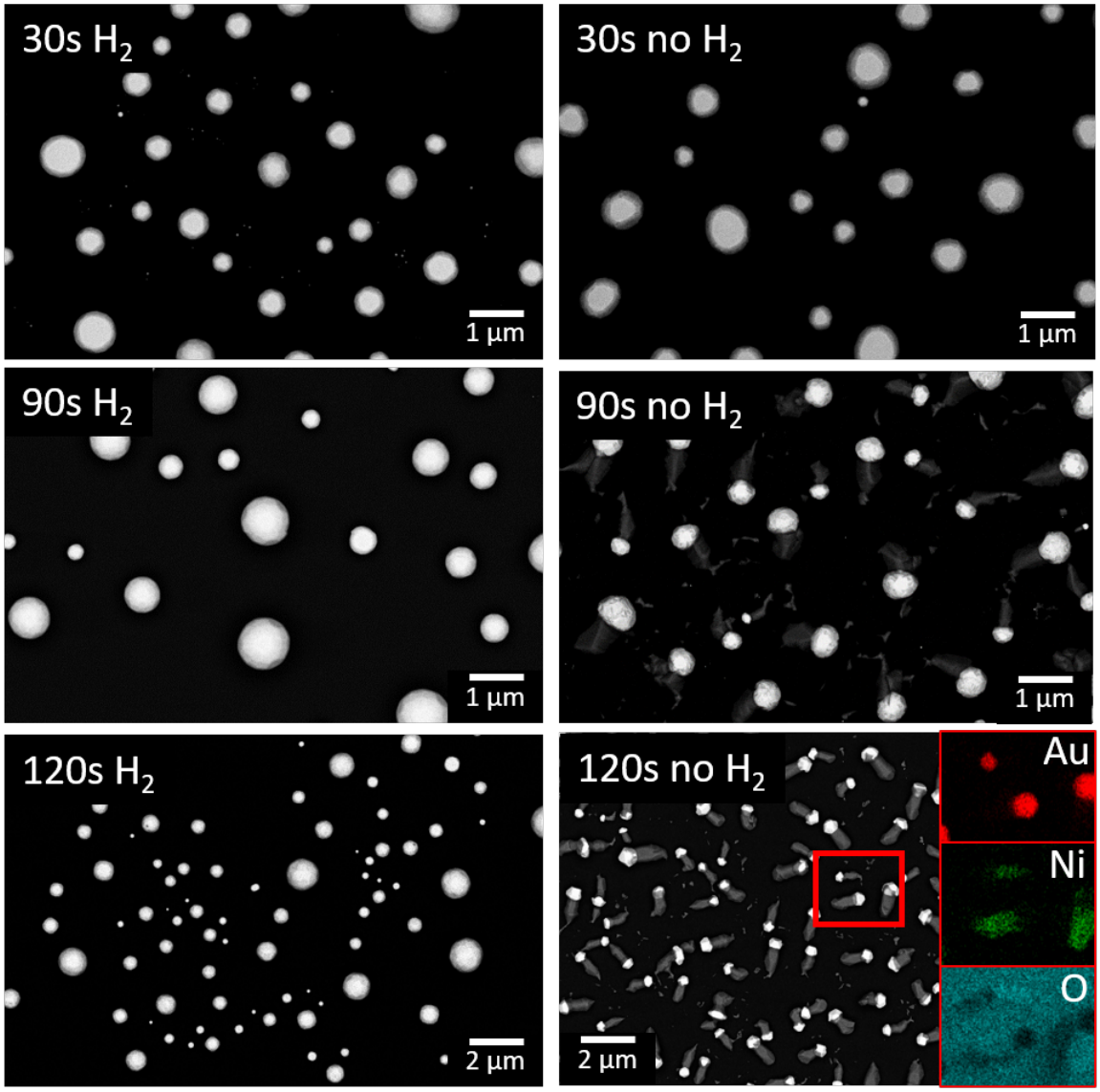

Figure 5.6: SEM BSE-images of $Au_{28}Ni_{72}$ alloy nanoparticles produced with and without reducing atmosphere. For a heating time of 30 s no difference can be found. For longer heating times (90 s and 120 s) the BSE contrast indicates an oxidation of the Ni due to the dark cones visible in the samples processed without H_2. A qualitative EDX mapping at the 120 s sample reinforces these observations (red boxes). The usage of a reducing atmosphere surpresses the oxidation since for all heating durations spherical, highly alloyed particles are formed (homogeneous Z-contrast).

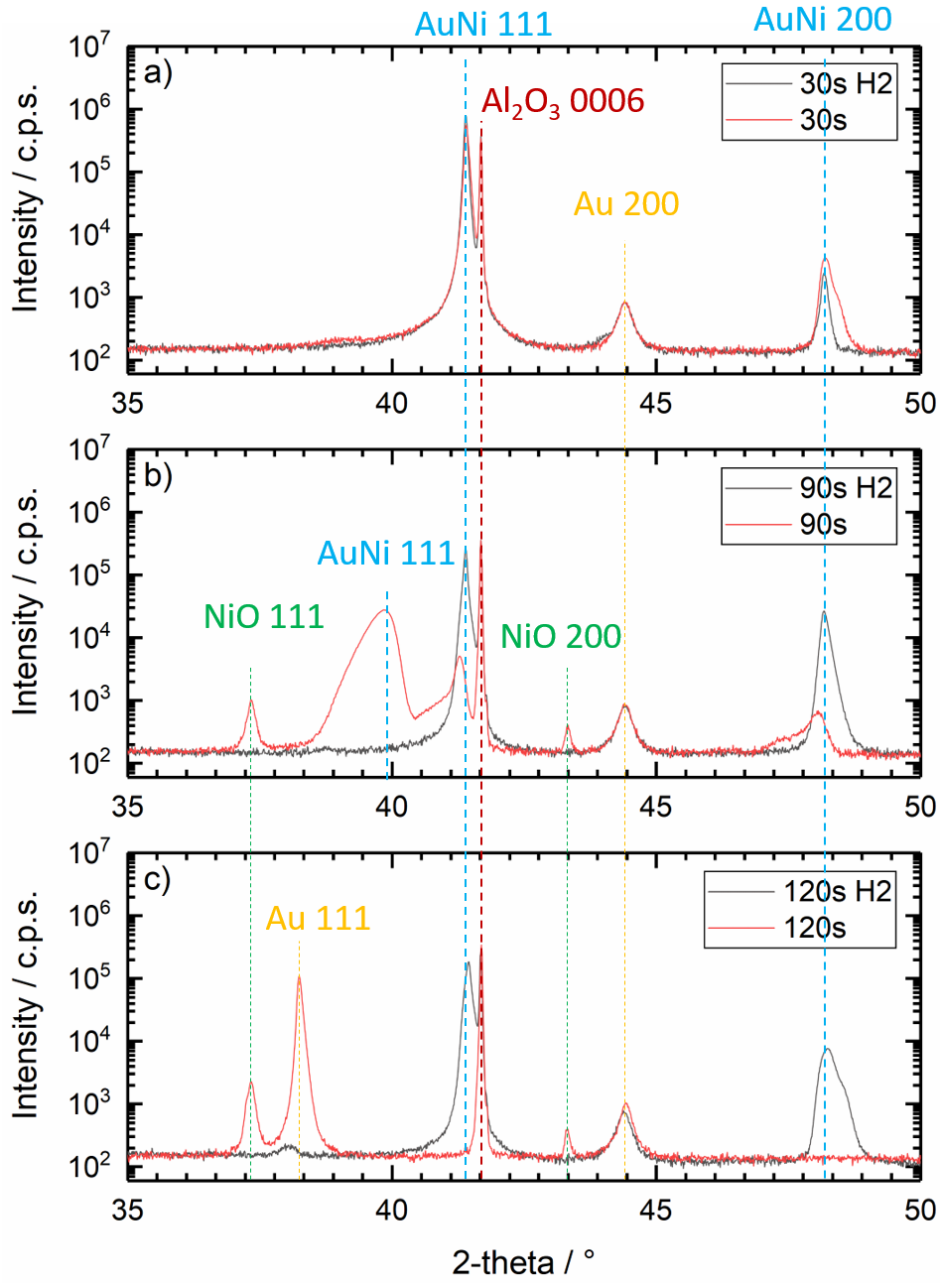

Figure 5.7: XRD out-of-plane measurements of samples with a nominal Au concentration of 28 at.%, dewetted in different atmospheres. The absence of a reducing agent leads to the formation of NiO. The longer the heating time, the stronger the oxidation.

5.3 Production of Au/Ni alloy nanoparticles

After optimizing the parameters for the thermal processing of AuNi alloy nanoparticles, two measurement series were carried out to produce them. For this purpose, AuNi bilayers were thermally processed at the Chair of Micro- and Nanostructure Research (WW9) of the FAU Erlangen-Nürnberg using an RTP system of the company AnnealSys (measurement series ERL). In addition, a measurement series was produced at the TU Ilmenau at the Institute of Materials Engineering in cooperation with Dr.-Ing. Wang, as there was the possibility of a 5 times higher H_2 gas flow, however at the cost of a slower cooling rate (measurement series ILM). A more detailed description of the respective measurement series can be found in Section 5.3.1 and Section 5.3.2.

5.3.1 Measurement series ERL

AuNi bilayers with a gold content of 0 at.% to 100 at.% (see Table 4.1) were dewetted using the RTP system described in Section 4.6.3 to produce AuNi alloy-nanoparticles. For this purpose the samples were treated at 935 °C for 120 s at atmospheric pressure with a gas flow of 400 sccm of Ar with 20 sccm of H_2 (20:1) during heating and 1000 sccm of Ar with 20 sccm of H_2 during fast-cooling.

5.3.1.1 SEM characterization

After thermal processing of the AuNi bilayers, SEM-investigations took place to characterize the morphology of the formed particles. Therefore an acceleration voltage of 5 keV was used. The BSE-images can be seen in Figure 5.8. In the pure Ni sample, in addition to the mainly elongated, flat particles, round and faceted particles are visible. The 3-fold symmetry of the facet pointing upwards suggests a (1 1 1) out-of-plane texturing. The samples with a gold content of 15 at.% to 70 at.% have formed spherical particles which do not show any Z-contrast, indicating that no phase separation has occured. A closer look at the particles reveals that the spherical shape consists of poorly developed nano-facets. Besides particles with a (1 1 1) orientation, particles are observed where the facet which is parallel to the substrate shows a 4-fold symmetry, indicating a (1 0 0) out-of-plane orientation. A further increase in the Au concentration up to a nominal concentration of 85 at.% leads to irregularly shaped particles which are larger compared to the particles with lower Au concentration. A thermal treatment with the parameters used here leads to complete dewetting of pure gold films, but the particle-state is not reached yet. The reason for this could be the lower surface energy

of Au compared to Ni (e.g. AuNi alloys).
Figure 5.9 a-k displays the particle size-distribution of the particles. It should be noted that for the sample with 85 at.% the particle radius was determined using a circle of the same area as the irregularly shaped particles. The particle sizes tend to follow a monomodal log-normal distribution. According to Figure 5.9f the mean particle radius is nearly constant in the range of 0 at.% to 50 at.% and then increases with increasing Au content.

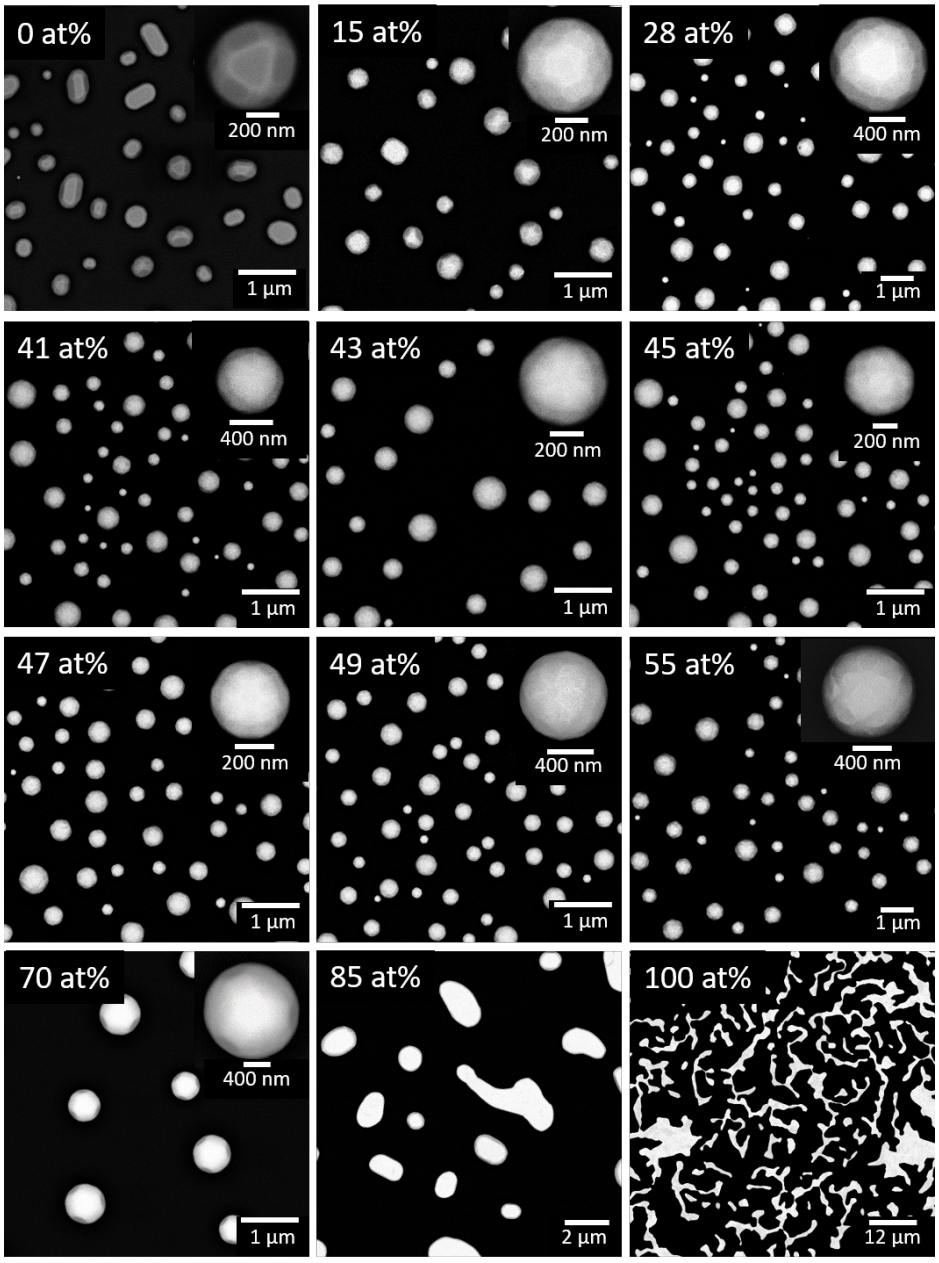

Figure 5.8: SEM BSE-images of the measurement series ERL. The Z-contrast indicates that all samples (15 at.% to 85 at.% are highly alloyed. Furthermore the equilibrated state has been reached for the pure Ni sample and the AuNi samples for Au concentrations up to 70 at.%. For the sample with 85 at.% and the pure Au sample the equilibrated state couldn‘t be reached.

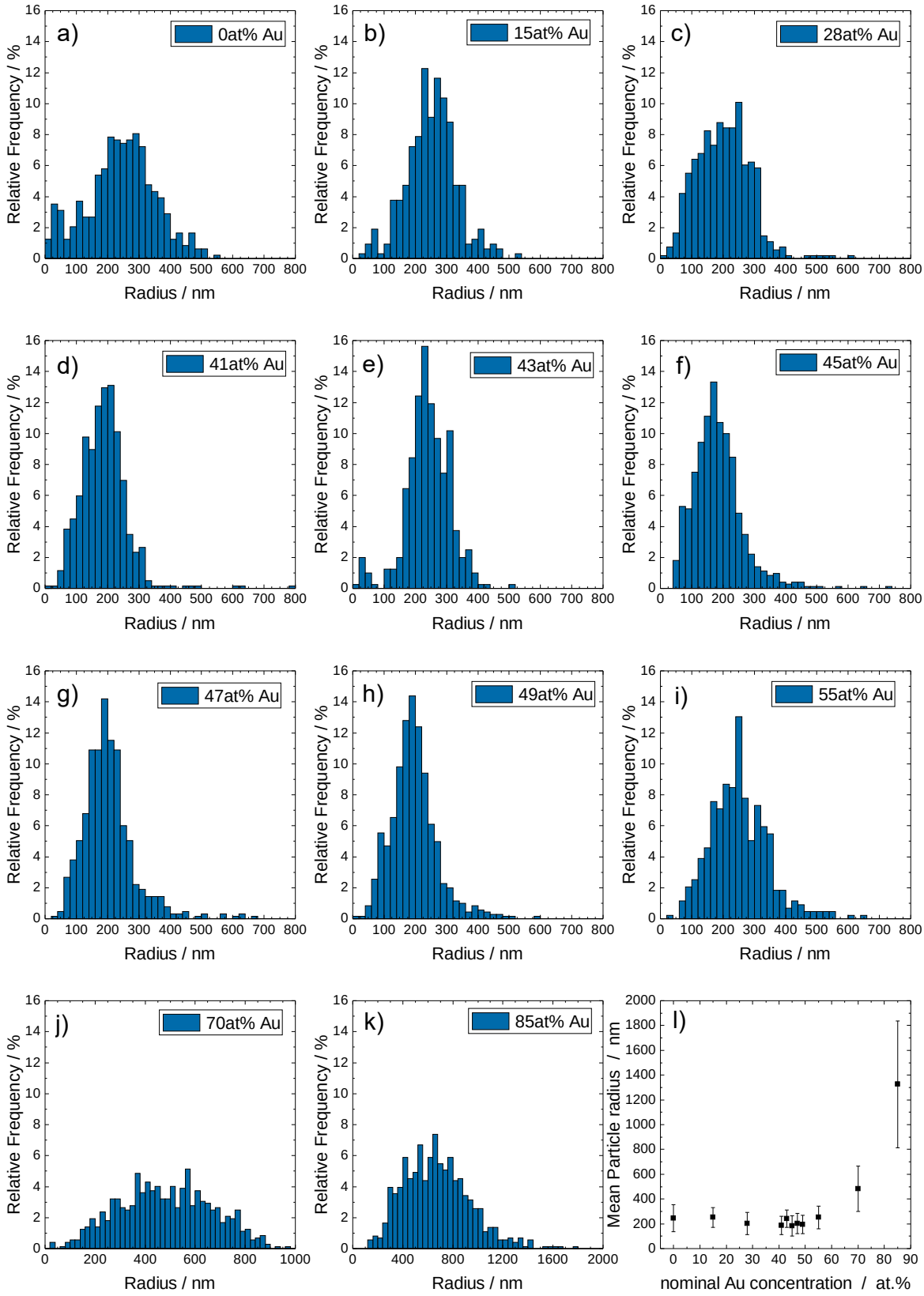

Figure 5.9: a-k) Particle size distribution of the measurement series ERL. The particles show a monomodal size distribution over the whole concentration range. l) Mean particle radius over the Au concentration. No significant influence of the Au concentration on the mean particle radius can be found up to 50 at.%. Afterwards an approximately linear increase of the particle size with increasing Au concentration is observed.

5.3.1.2 Qualitative and quantitative EDX characterization

To verifiy the formation of an AuNi solid solution, qualitative EDX-mappings were prepared. For the mapping, an accelaration voltage of 20 keV was used. The mappings can be seen in Figure 5.10 and Figure 5.11 and confirm the impression of alloy formation created by the BSE images, as no regions within the particles can be identified with the accumulation of any of the elements. Both Au (red) and Ni (green) are homogeneously distributed in all particles. This finding is in line with the homogeneous contrast in the BSE images compiled in Figure 5.8.
To quantify the Au content, EDX point measurements were performed on five particles each, with an acceleration voltage of 20 keV and a current of 0.80 nA. The results can be seen in Table 5.1.

Table 5.1: Comparison of the nominal Au-content and the Au-content measured by EDX-point measurements of the measurement series ERL.

nominal Au content / at.%	measured Au content / at.%	Deviation / at.%
15	22.0 ± 0.5	7.0
28	42.1 ± 0.7	14.1
41	50.0 ± 0.6	9.0
43	54.0 ± 0.9	11.0
45	54.0 ± 0.6	9.0
47	60.4 ± 1.8	13.5
49	62.4 ± 0.9	13.4
55	69.0 ± 0.5	14.0
70	80.6 ± 0.3	10.6
85	90.4 ± 0.3	5.4

It can be seen that the values quantified by point measurements show a relatively high deviation from the nominally determined Au content with a mean deviation of (10.7 ± 3.1) at.%. Reasons for overestimating the gold content could include absorption of the Ni signal due to the gold, or, more likely, incorrect tooling factors of the E-Beam PVD system resulting in an incorrect nominal value. In order to avoid confusion, the samples are labeled according to the nominally determined composition in the further course of the work.

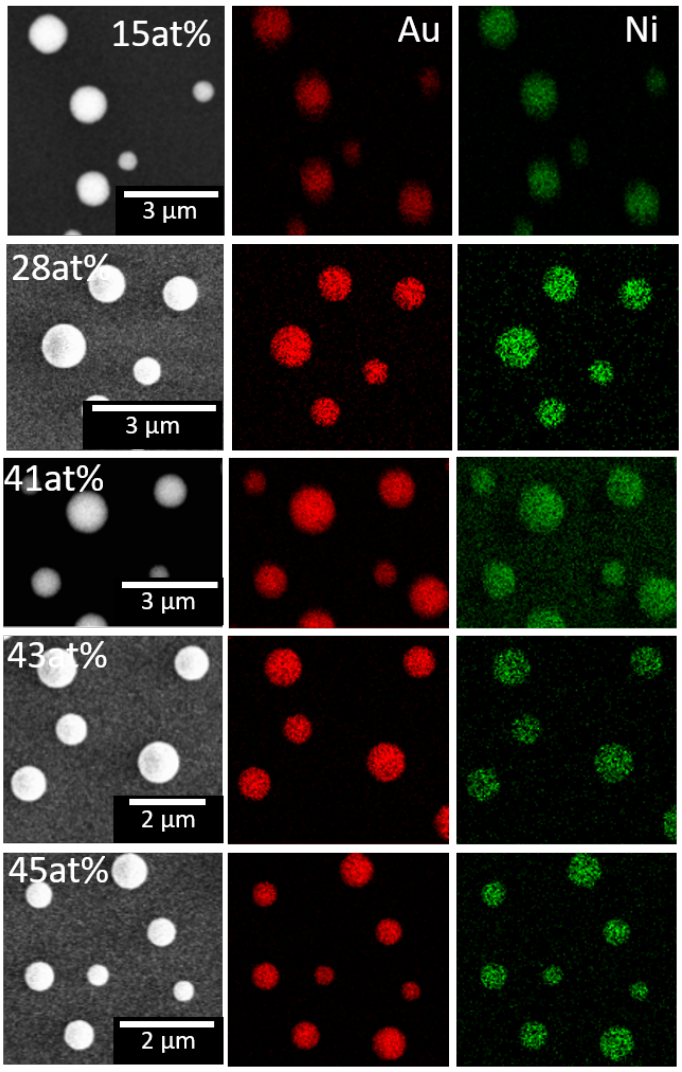

Figure 5.10: Qualitative EDX-mappings of the AuNi-particles with the nominal composition of 15 at.%, 28 at.%, 41 at.%, 43 at.% and 45 at.%. Both elements, Au (red) and Ni (green), are homogeneously distributed within the particles, confirming the successful formation of AuNi-alloy nanoparticles.

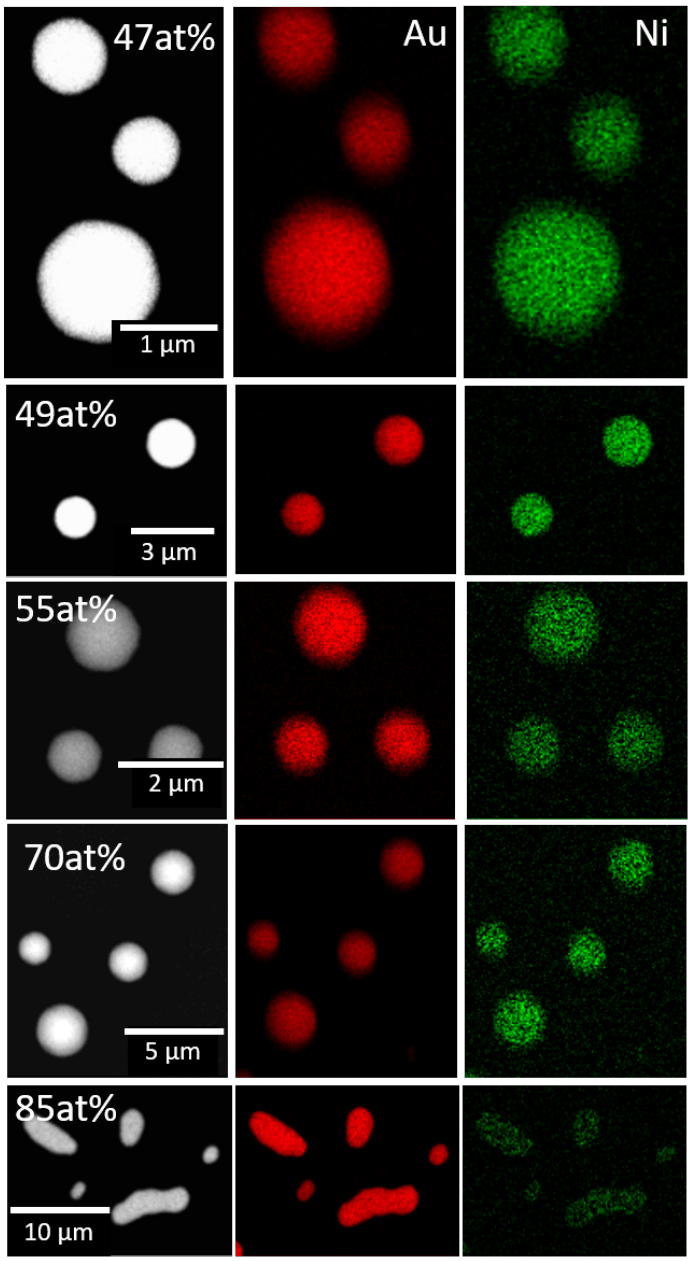

Figure 5.11: Qualitative EDX-mappings of the AuNi-particles with the nominal composition of 47 at.%, 49 at.%, 55 at.%, 70 at.% and 85 at.%. Both elements, Au (red) and Ni (green), are homogeneously distributed within the particles, confirming the successful formation of AuNi-alloy nanoparticles.

5.3.1.3 XRD characterization

In correlation to the SEM-investigation XRD out-of-plane and in-plane measurements were carried out to determine on one hand the orientation, texturing and alloyed state of the particles and on the other hand the required Au concentration for lattice matching between the AuNi alloy NPs and the substrate.

As described in Section 4.5.2, by performing out-of-plane XRD measurements it is possible to determine the orientation of the lattice planes which are parallel to the surface. The diffractograms can be seen in Figure A.1a. When viewing the diffractogram, peaks in an angular range from 64.7° to 72.8° can be detected. The peak at 64.7° corresponds to the Au (2 2 0) planes and the peaks from 66.4° to 72.8° are attributed to the (2 2 0) planes of the AuNi-phase (see Table A.1). Figure 5.12a shows an enhanced view of the 2-theta range of 35° to 55°. The (1 1 1) and (2 0 0) peaks of Ni and Au can be clearly identified. By subsequently increasing the Au content in the samples, there is a left-shift of the peaks to lower 2-theta values, indicating an increase in the lattice constant due to alloying. Figure 5.12b shows the integrated peak intensity ratio (1 1 1)/(2 0 0) for the Au, Ni and AuNi samples. It is noticeable that both the pure Ni and the pure Au sample show a strong (1 1 1) texturing. The addition of small amounts of gold (nominal 15 at.%) results in a strong decrease in (1 1 1) texturing, since the ratio of (1 1 1)/(2 0 0) is almost 1:1. A further increase of the gold content to nominal 28 at.% leads first to an increase of the (1 1 1) texturing. Subsequently, for samples with a nominal gold content of 41 at.%, 43 at.%, 45 at.%, 47 at.% and 49 at.%, there is a steady decline of the preferred (1 1 1) orientation with increasing gold content until a local minimum is reached at 49 at.%. Afterwards, there is another increase, whereby the sample with nominal 85 at.%-Au has the maximum (1 1 1) texturing.

The in-plane diffractogram is shown in Figure 5.12c and supports the impression of alloy formation due to the left-shift of the {2 2 0} AuNi peaks with increasing Au content. The strong appearence of the {2 2 0} reflections for pure Ni and alloys with a nominal Au concentration of 15 at.%, 70 at.% and 85 at.% indicates an in-plane texturing following an orientation relationship of $\langle 1\,1\,0 \rangle$ AuNi $\parallel$ $\langle 1\,\bar{1}\,0\,0 \rangle$ α-Al_2O_3. Interestingly no in-plane peaks are visible for the samples with 41 at.%, 43 at.%, 45 at.% and 49 at.% Au at first sight. The red box in Figure 5.12c shows an enhanced view of the angular range around the $(3\,\bar{3}\,0\,0)$ peak of the substrate. In this enhanced view, peaks for the samples with 41 at.% and 43 at.% can be seen at the right of the peak (see blue arrows) indicating only a small deviation of the lattice spacings of the substrate and

the nanoparticles. Due to the absence of in-plane peaks for the alloys with 45 at.% and 49 at.% it can be assumed that matching of the two d-values of the particles and the substrate has nearly occurred.
With the exact positions of the peaks (thus the 2θ-values) and Equation 4.4 the lattice parameters of the AuNi-alloys can be calculated. The results are listed in Table A.2. As already mentioned before, for lattice matching of the (2 2 0)-AuNi lattice planes and the $(3\,\overline{3}\,0\,0)$ planes of sapphire, a lattice parameter of 3.89 Å is needed, which is achieved with a nominal Au concentration of 49 at.%. This is also visualized in Figure 5.12d. Based on the nominally determined gold content, a deviation of the theoretical values determined according to Vegard as well as from the values for bulk alloys [60] can be seen. However, when plotting the lattice parameters using the quantified gold concentrations, an adjustment is made to the bulk values. Furthermore, the lattice parameters of pure Ni and the alloys with 15 at.%, 70 at.% and 85 at.% Au content could be determined from the in-plane peak positions. Due to the overlap with the out-of-plane values a tetragonal distortion of the particles can be excluded.

In conclusion, the XRD measurements supplement the SEM findings well, namely, the alloyed state and the relative poor texturing of the NPs. Moreover, the nominal Au film thickness necessary for lattice matching could be determined.

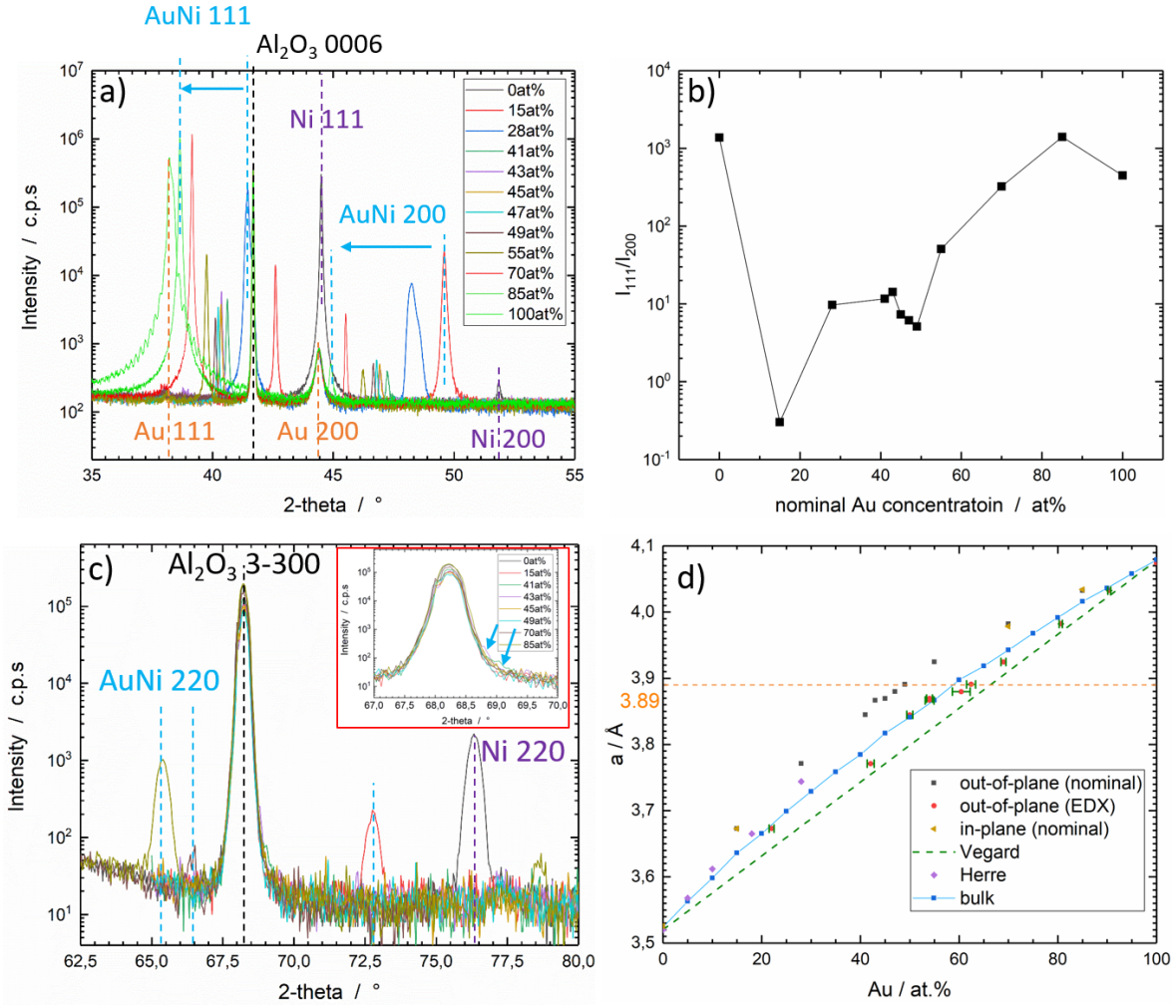

Figure 5.12: a) XRD out-of-plane pattern of the the measurement series ERL. For all samples the (2 0 0) and (1 1 1)-peaks can be clearly identified. The shift of the peaks to smaller scattering angles as a function of the Au concentration indicates that alloying has taken place. b) Intensity ratio (1 1 1)/(2 0 0) of the whole measurement series. While the pure elemement samples show a highly pronounced (1 1 1) texture, the alloyed samples show reduced texturing. c) In-plane XRD-measurements. The {2 2 0}-peaks of pure Ni and samples with 15 at.% and 85 at.% Au are clearly visible. For samples with 41 at.%, 43 at.% and 70 at.% only low-intensity peaks can be identified revealing a lack of in-plane texturing. The absence of the peak for samples with 45 at.% and 49 at.% Au indicating a lattice matching of the particles and the substrate. d) Lattice parameters of the AuNi-alloy system over the Au concentration. According to the nominal Au-values a deviation from Vegard [61] and bulk values [60] is visible. After quantifying the gold content, this deviation becomes smaller and an adjustment is made to the quadratic progression of the bulk values. The overlap of the in-plane and out-of-plane values allows an exclusion of a tetragonal particle distortion.

5.3.2 Measurement series ILM

As already mentioned in addition to the measurement series ERL, a second series was thermally processed at the same temperature and time at the TU Ilmenau. The different compositions are listed in Table 4.2. However, in contrast to the previous measurement series, the Ar-gas flow was increased to 2000 sccm and the H_2-gas flow was increased to 100 sccm during heating. For cooling the gas flow of Ar was increased to 4000 sccm while the gas flow of H_2 was kept constant. Despite the higher gas flow during cooling, the cooling rate of about $9\,^{\circ}\mathrm{C\,s^{-1}}$ is much lower in this case.

5.3.2.1 SEM characterization

Figure 5.13 shows BSE-images of the dewetted bilayers. As can be seen, spherical particles are formed after the annealing process. The enhanced view of the particles reveal that they, similar to the ERL particles, consist of poorly developed nano-facets. The Z-contrast indicates that segregation has taken place in isolated particles, but the majority of the particles are present as AuNi-alloy particles.
Figure 5.14 a-j show the particle distribution of the different samples. It can be seen that from a concentration of 45 at.% there is a change in the particle distribution. While samples with a composition of 28 at.%, 35 at.% and 40 at.% show a monomodal particle distribution, samples with a composition of 45 at.% and above show a bimodal distribution. The mean particle radius over the nominal Au content is shown in Figure 5.14k. Starting at 28 at.% with a mean particle radius of 180 nm up to a concentration of 45 at.% a small increase to 211 nm of the mean radius is observed with increasing gold content. While an increase in the Au-content by 5 at.% in this area shows a maximum increase in the mean radius by 4 nm, a further increase to 50 at.% interestingly leads to a jump to 290 nm. The reason for this jump could be a lattice matching at 45 at.%. It can be seen that in the further course up to a concentration of 57.5 at.% the mean radius increases and afterwards the value decreases again with increasing Au-content. Furthermore, the particle density of the respective samples was determined (see Figure 5.14l). From 28 at.% to 57.5 at.% there is a decrease of the particle density, whereby at 57.5 at.% a global minimum is reached and the particle density increases again afterwards. Based on the mean particle radius, this was to be expected since the same area was evaluated for each sample. Thus the larger the particles the fewer particles can be found per area.

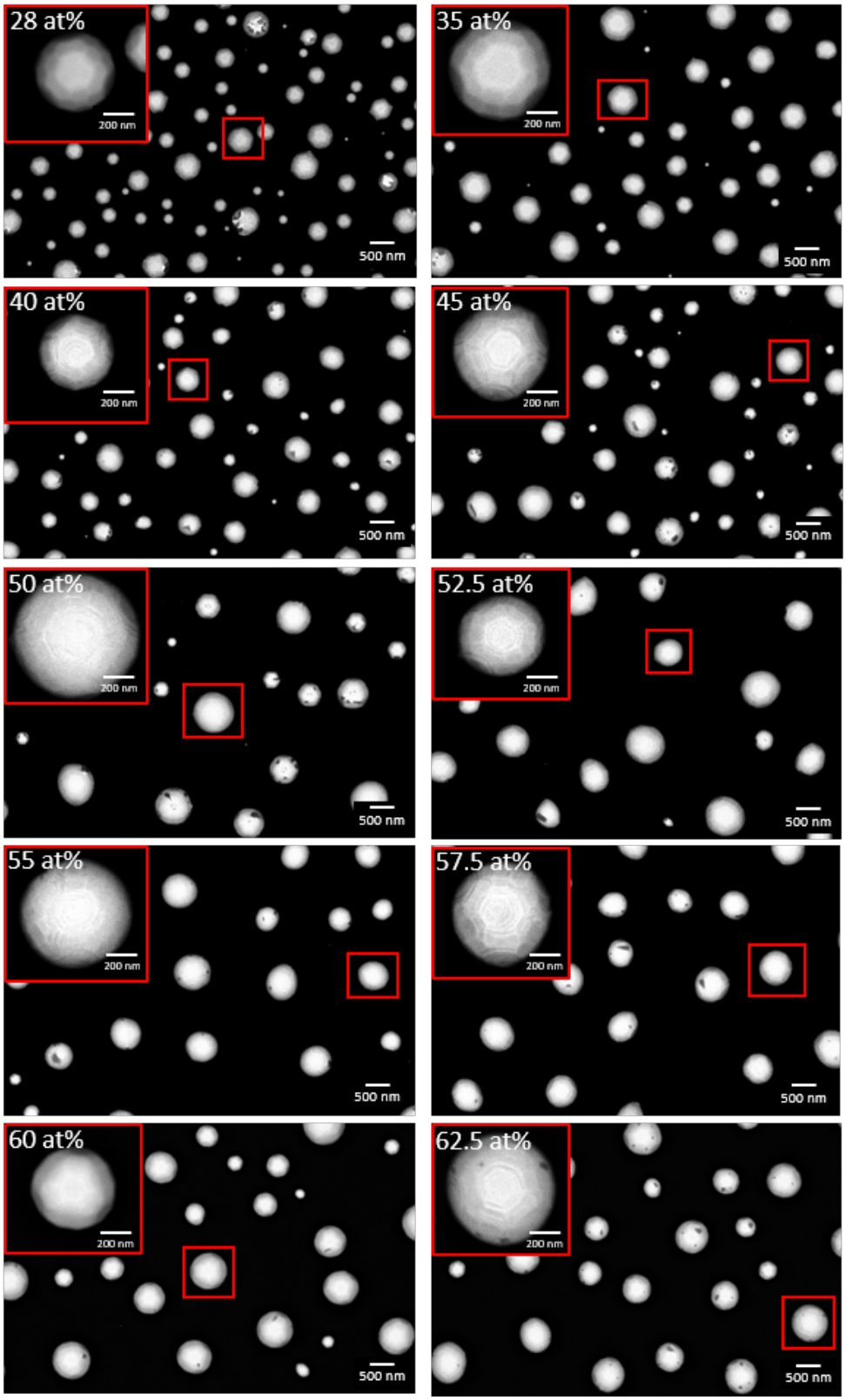

Figure 5.13: SEM BSE-images of AuNi-bilayers of different compositions. The samples were processed in Ilmenau at 935 °C for 2 min. The Z-contrast typical for BSE gives a qualitative impression of alloy formation with isolated Au (light) and Ni microsegregations (dark).

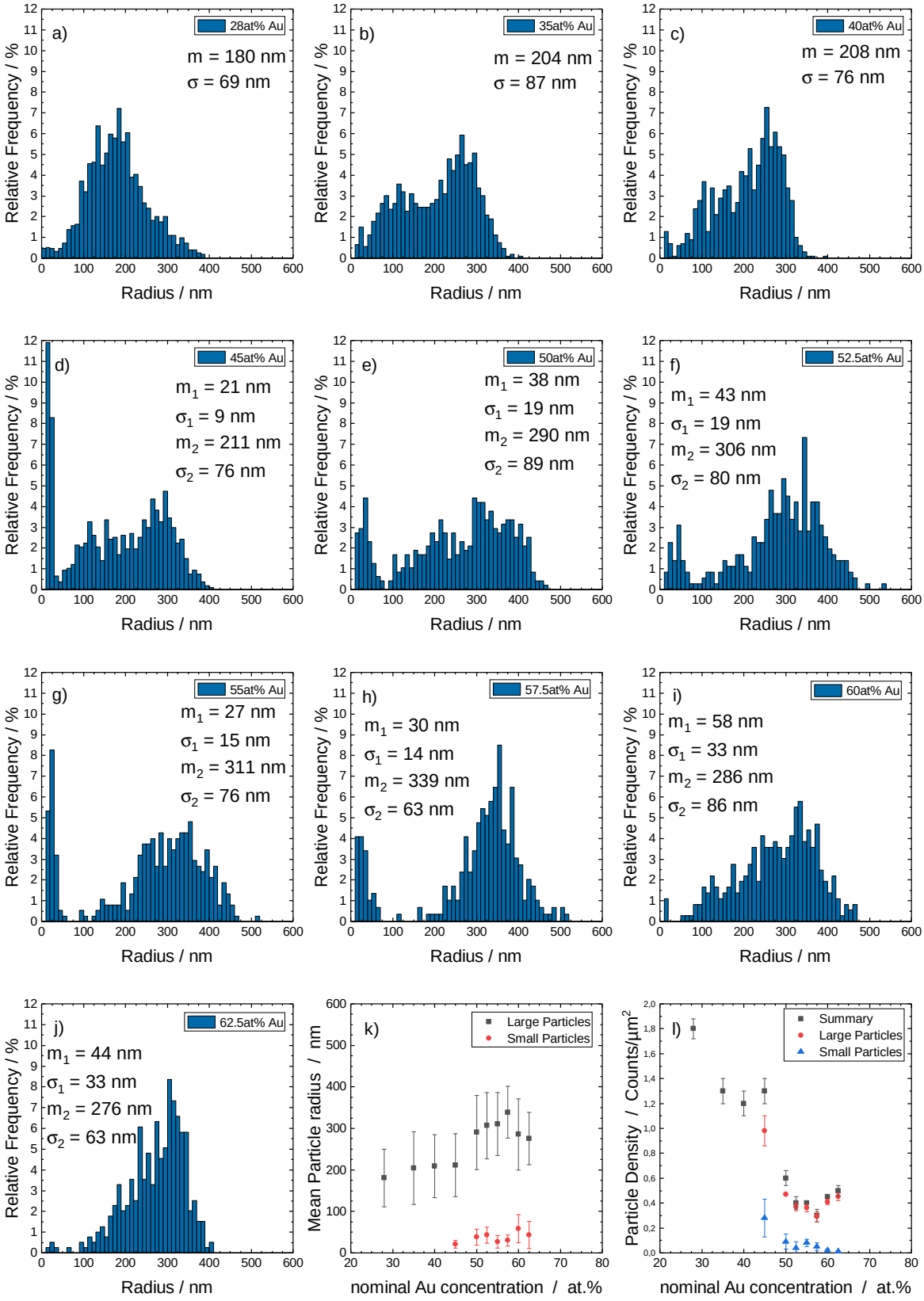

Figure 5.14: a-j) Particle size distribution of the measurement series ILM. With increasing Au-concentration a change in the particle distribution from monomodal to bimodal is noticeable. k) Mean particle radius over the Au concentration. The jump of the mean particle radius of 80 nm from 45 at.% to 50 at.% is a first indication that lattice matching is achieved for an Au-concentration of 45 at.%. l) Particle density over the Au concentration. The evolution of the particle density is complementary to the evolution of the mean particle size, as expected.

5.3.2.2 Qualitative and quantitative EDX characterization

The SEM characterization gave the impression that although Au and Ni microsegregations are visible in individual particles, the majority of the NPs are present as AuNi alloys. To verify this, qualitative EDX mappings were performed (see Figure 5.15 and Figure 5.16). According to the mappings, both elements are distributed homogeneously within the particles, confirming the successful formation of an alloyed state. The nanoscale segregations visible in the SEM images could not be resolved by EDX mapping. This could be explained by a too large interaction volume of the electrons with the sample (see Section 4.3.1).

As in the previous measurement series, EDX point measurements were performed on five nanoparticles each to check the exact gold content of the samples. The measurement results and the deviation from the nominal sample composition are shown in Table 5.2. In almost all samples a systematic deviation from the nominal values can be detected. Only the sample with 55 at.% shows a higher deviation than the others and cannot be included in the systematic shift. The mean deviation from the nominally determined composition is (9.9 ± 1.7) at.%.

Table 5.2: Comparison of the nominal Au-content and the Au-content measured by EDX point measurements of the measurement series ILM.

nominal Au content / at.%	measured Au content / at.%	Deviation / at.%
28	37.6 ± 1.6	9.6
35	44.1 ± 1.2	9.1
40	49.0 ± 0.6	9.0
45	54.8 ± 0.3	9.8
50	59.9 ± 0.4	9.9
52.5	62.2 ± 1.2	9.7
55	69.5 ± 0.5	14.5
57.5	67.2 ± 0.3	9.7
60	68.9 ± 0.7	8.9
62.5	71.4 ± 0.4	8.9

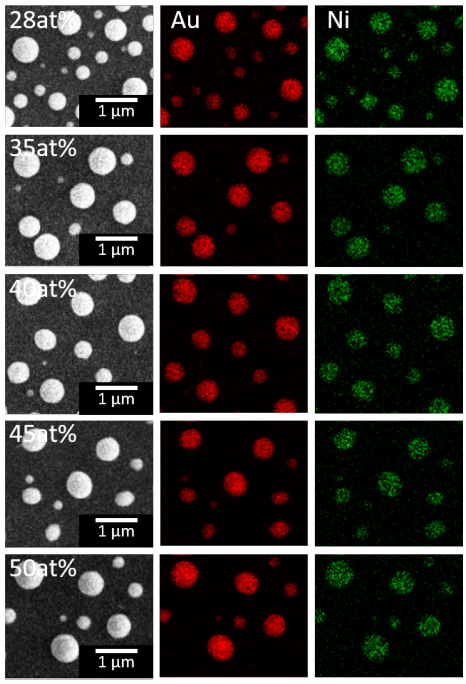

Figure 5.15: SE-images and qualitative EDX-mappings of the AuNi-particles ILM with the nominal composition of 28 at.%, 35 at.%, 40 at.%, 45 at.% and 50 at.%. Both elements, Au (red) and Ni (green), are homogeneously distributed within the particles, confirming the successful formation of AuNi-alloy nanoparticles.

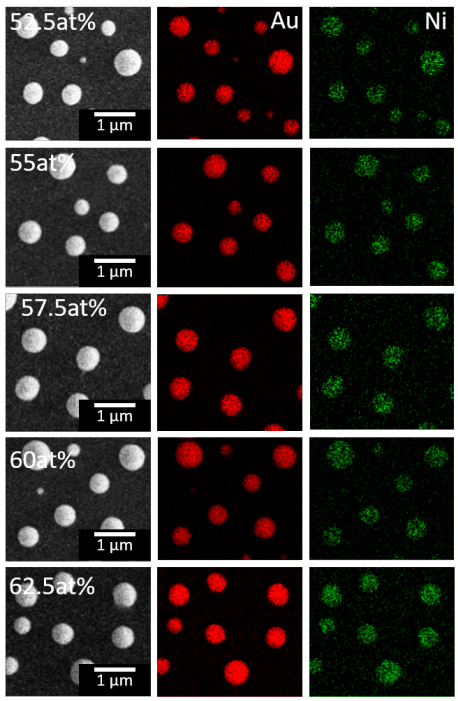

Figure 5.16: SE-images and qualitative EDX-mappings of the AuNi-particles ILM with the nominal composition of 52.5 at.%, 55 at.%, 57.5 at.%, 60 at.% and 62.5 at.%. Both elements, Au (red) and Ni (green), are homogeneously distributed within the particles, confirming the successful formation of AuNi-alloy nanoparticles.

5.3.2.3 XRD characterization

As in the ERL series, XRD out-of-plane and in-plane measurements were performed to investigate the orientation of the NPs and to find out at which concentration lattice matching was achieved.

Figure A.1b) illustrates the out-of-plane diffractogram with an angular range of 30° to 80°. It is noticeable that, as in the ERL measurement series, the Au (2 2 0) peak is visible, but unlike the previous measurement series, no AuNi (2 2 0) orientation can be found, which is a first indication of higher (1 1 1) texturing. This first impression is confirmed by looking at the angular range of 35° to 50° (see Figure 5.17a). Hardly any AuNi particles with a (2 0 0) orientation are present. Only for samples with a gold content of 28 at.%, 35 at.% and 40 at.% peaks of very low intensity can be identified, which correspond to the (2 0 0) lattice spacing of the AuNi-phase. Furthermore strong (1 1 1)-peaks are present for all compositions.

Similar to the measurement series ERL, the grade of (1 1 1)-texturing is quantified by plotting the ratio of the integrated intensity of the (1 1 1)-peak and the (2 0 0)-peak over the nominal Au concentration (see Figure 5.17b). It can be seen that at 35 at.% the texturing is the lowest, attributed to the rise of particles with a {2 0 0} out-of-plane orientation. A further increase in the gold content leads to an increase in {1 1 1} texturing until saturation occurs from 50 at.% and the degree of texturing remains approximately constant.

When comparing the AuNi peaks with the Al_2O_3 peak, it is noticeable that the peaks are both widened and asymmetrical, which indicates a strained particle lattice. Due to the peak positions the lattice parameters of the alloy nanoparticle are calculated, which are listed in Table A.3. As expected, the lattice parameters increase with increasing gold content. Based on the quantified gold content, the evolution of the lattice parameter over the gold content follows the model for bulk samples (see Figure 5.17d). With lattice parameters of 3.88 Å for the $Au_{45}Ni_{55}$-alloy and 3.90 Å for the $Au_{50}Ni_{50}$-alloy, there are two candidates where lattice-matching is nearly achieved.

For an exact statement whether a matching between the {2 2 0} planes of the AuNi alloy particles and the {3 $\bar{3}$ 0 0} planes of the substrate has taken place, the in-plane measurements, which can be seen in Figure 5.17c, must be considered. For the samples with 55 at.% and 60 at.% Au a clear AuNi (2 2 0) peak could be observed on the left of the (3 $\bar{3}$ 0 0) peak of Al_2O_3 indicating a larger lattice-plane distance, e.g. a larger lattice-constant. Also for 35 at.% and 40 at.% Au a clear shoulder on the right of the

sapphire peak is visible, due to smaller lattice constants. As expected, no in-plane peak is recognizable for the samples with 45 at.% and 50 at.% Au, since according to the out-of-plane measurement the lattice parameter has only a small deviation from the lattice parameter where matching of the AuNi (2 2 0) planes and the Al_2O_3 ($3\,\bar{3}\,0\,0$) planes is considered. Nevertheless, a small difference between the two samples can be seen. Therefore the diffuse signal below the peaks has to be considered, which could be an indicator for strained particles or for surface strain in the substrate. It can be assumed that the more precisely lattice matching is achieved, the lower the strain and thus the diffuse background signal should be, so that it can be assumed that the sample with 45 at.% has reached the closest lattice matching. A detailed discussion of the in-plane results can be found in Section 6.4.

Figure 5.18a) shows the {1 1 1} AuNi pole figures for particles with a nominal composition of 35 at.%, 45 at.%, 60 at.% and 62.5 at.% Au and Figure 5.18b) the corresponding α line cut. For indexing the peaks to the corresponding lattice planes Equation 4.6 was used. The central peak in all pole figures arises from the (1 1 1) AuNi planes which are parallel to the surface. The additional diffraction peaks at $\alpha = 70°$ stem from the {1 1 1} side facets of the particles which are inclined to the (1 1 1) surface plane. In all samples, six reflections separated by 60° are visible, indicating that two orientation variants which are rotated by 180° with respect to each other are present (see Figure 5.19). Comparing the positions of the AuNi peaks with {0 0 0 6} pole figures of the substrate (see Figure A.3) these particles have an orientation relationship to the substrate of $\{1\,1\,1\}\pm\langle 1\,1\,0\rangle$ AuNi $\parallel (0\,0\,0\,1)\langle 1\,0\,\bar{1}\,0\rangle\alpha$-$Al_2O_3$ (OR1). Interestingly additional peaks beside the two twin variants arise with a rotation around the $\langle 1\,1\,1\rangle$ axis of ± 18° with respect to twin variant 1. According to simulated diffraction patterns of AuNi and sapphire (see Figure A.2), the rotation could lead to an orientation relationship of $\{1\,1\,1\}\pm\langle\bar{3}\,2\,0\rangle$ AuNi $\parallel (0\,0\,0\,1)\langle 1\,0\,\bar{1}\,0\rangle\alpha$-$Al_2O_3$ and is labeled as OR2. It seems that this orientation becomes more favorable with increasing Au content, since the intensity ratio of OR1 and OR2 shows an exponential decrease (Figure 5.19b). An analysis of the FWHM of the {1 1 1} reflections along the β-direction at $\alpha = 70°$ reveals values of 2° for OR1 and 4° for OR2.

At an angle of $\alpha = 56°$ another ring of individual reflections arises. These reflections could belong to the {1 1 1} reflections of particles which have a {1 0 0} out-of-plane orientation. When comparing the four pole figures, it is noticeable that with increasing Au content the peaks of these reflections lose intensity, which is in good agreement with the out-of-plane diffractograms which have shown that with an increasing amount of Au the {1 1 1} texturing arises. While it can hardly be seen in the pole-figures, the α

linescan (Figure 5.18b) reveals a third low-intensity peak at 38°. This peak could arise from particles with a $\{2\,1\,0\}$ out-of-plane orientation. For a detailed discussion of the orientation relationships the reader is referred to Section 6.6.

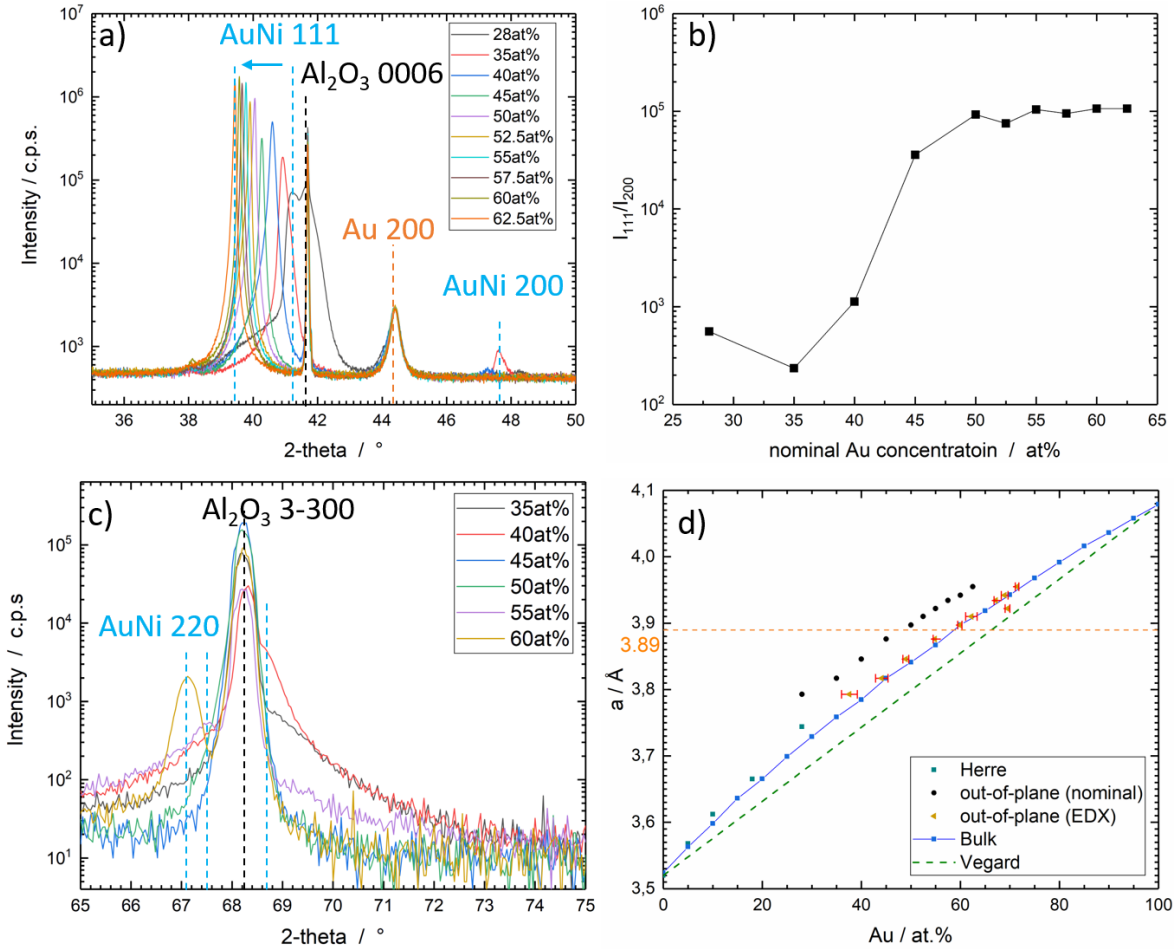

Figure 5.17: a) XRD out-of-plane diffractogram of the measurement series ILM. Strong (1 1 1) reflections are visible for all samples. Samples with a nominal Au concentration of 28 at.%, 35 at.% and 40 at.% also show low intensity-reflections of particles with a (2 0 0) orientation. The shift of the peaks to smaller scattering angles with increasing Au concentration confirms the formation of AuNi alloy nanoparticles. b) Intensity ratio (1 1 1)/(2 0 0) over the Au concentration. The texturing shows a local minimum at an Au concentration of 35 at.%. Afterwards it increases with increasing Au concentration up to 50 at.%. From 50 at.% to 62.5 at.% no further increase of the texturing is recognizable. c) In-plane diffractogram of the measurement series ILM, showing the presence of a diffuse signal symmetrically distributed around the particle-peaks, resulting from a buckling of the terminating AuNi layer. The absence of the diffuse signal reveals a change in the particle-substrate interface structure for the sample with a nominal Au concentration of 45 at.%. d) Extracted evolution of the lattice parameter from the XRD out-of-plane measurements. According to the nominal Au-values a deviation from Vegard [61] and bulk values [60] is visible. After quantifying the gold content, this deviation becomes smaller and an adjustment is made to the quadratic progression of the bulk values.

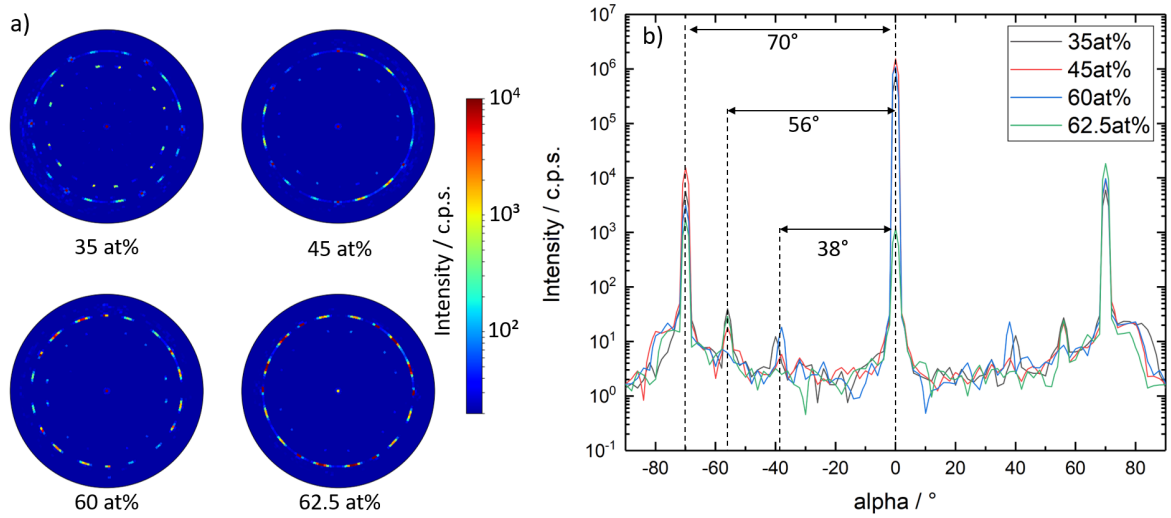

Figure 5.18: a) {1 1 1} XRD pole-figures of the AuNi particles on sapphire with nominal Au concentration of 35 at.%, 45 at.%, 60 at.% and 62.5 at.%.b) Corresponding α-linescan of the pole figures. Three peaks are observed at 70°, 56° and 38° which correspond to the inclined {1 1 1} planes of particles with the {1 1 1}-, {1 0 0}- and {2 1 0}-planes parallel to the substrate.

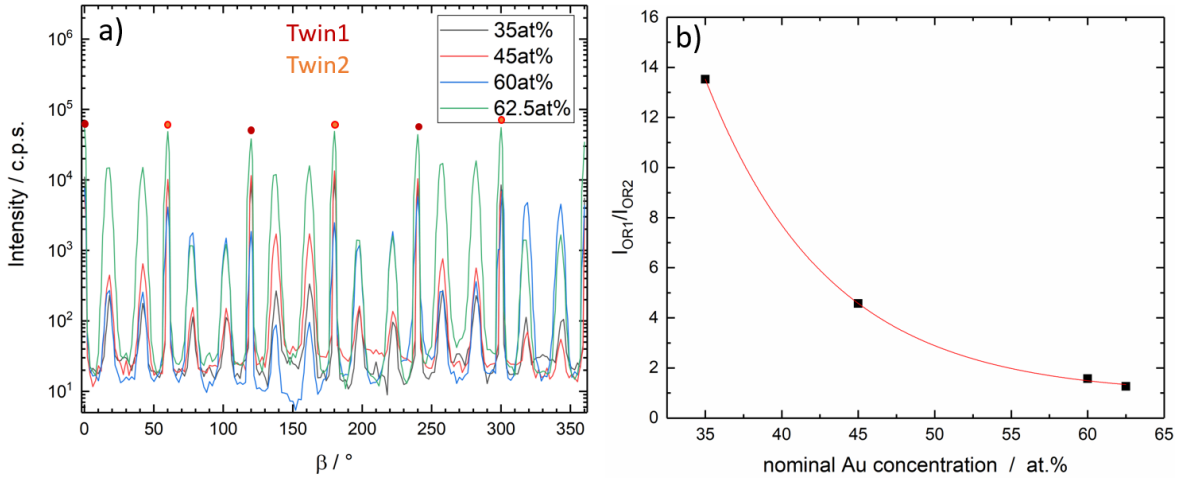

Figure 5.19: a) Circular linecut at α=70° representing the {1 1 1} side-facets of the particles which are inclined to the (1 1 1) surface plane. Six main peaks could be observed with an angular deviation of 60° to each other. The six reflections belong to the two twin variants with an orientation relationship of $\{1\,1\,1\}\pm\langle 1\,1\,0\rangle$ AuNi $\parallel$ $(0\,0\,0\,1)\langle 1\,0\,\bar{1}\,0\rangle\alpha$-$Al_2O_3$ (OR1). Two additional twin formations could be found with a rotation of ± 18° with respect to Twin 1 (OR2). b) Ratio of the integrated Intensity of OR1 and OR2. With increasing Au content the ratio follows an exponential decrease.

5.3.2.4 TEM characterization

To supplement the in-plane XRD measurements and to get a deeper understanding of the interface TEM investigations were performed. For this purpose a plan-view lamella was prepared as described in Section 4.6.4. Figure 5.20a shows a CTEM overview of the lamella. As can be seen in Figure 5.20b and Figure 5.20c the lamella contains particles of the two symmetrical equivalent twin variants with the orientation relationship of $\langle 1\,1\,1\rangle \parallel \langle 0\,0\,0\,1\rangle$ and $\langle 1\,1\,0\rangle \parallel \langle 1\,0\,\bar{1}\,0\rangle$.

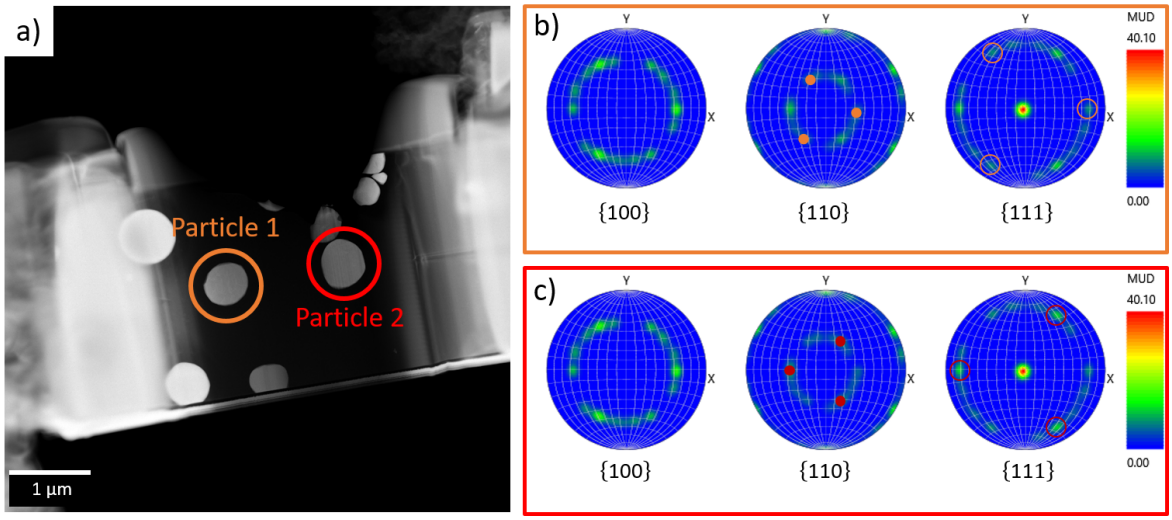

Figure 5.20: a) TEM-overview of the plan-view lamella of the sample with a nominal composition of 45 at.%. b) and c) EBSD pole figures of both particles clearly showing the (1 1 1) out-of-plane orientation. It can also be seen that the two particles are two symmetrical equivalent twin variants, since the patterns differ by a 180° rotation around the $\langle 1\,1\,1\rangle$ surface normal.

In Figure 5.21 and Figure 5.22 the [1 1 1] AuNi ZA $\parallel$ [0 0 0 1] α-Al_2O_3 ZA SAED-patterns of the two particles can be seen. Using line cuts (blue lines), the {2 2 0} lattice plane distance of the AuNi alloy was determined to $(7.29 \pm 0.03)\,\mathrm{nm}^{-1}$ (Particle 1) and $(7.27 \pm 0.03)\,\mathrm{nm}^{-1}$ (Particle 2), which corresponds to lattice parameters of 3.88 Å and 3.89 Å. In addition, no splitting of the {2 2 0}-AuNi and $\{3\,\bar{3}\,0\,0\}$-peak of sapphire is visible. At the given time it can therefore be concluded that with a nominal concentration of 45 at.% a lattice maching of the AuNi nanoparticles to the substrate has successfully taken place.

In addition to the CTEM SAED investigation, STEM was used to investigate the two particles. Figure 5.23 shows ADF images of both particles. Interestingly in both particles several features can be detected. Particle 1 shows hexagonal features with a mean line distance of (95 ± 3) nm which is indicated in Figure 5.23a. This could be an indication for a {1 1 1} dislocation network.

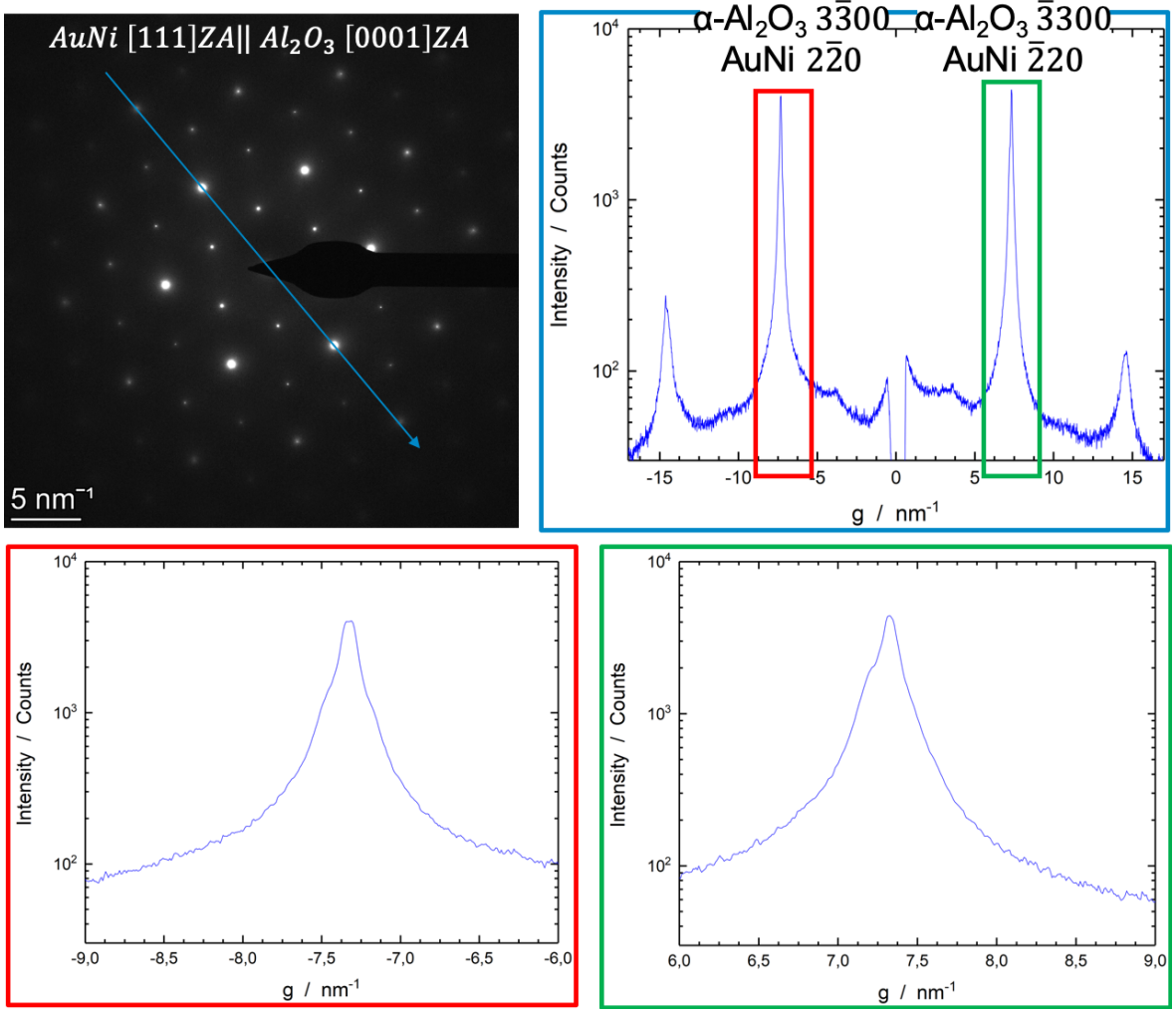

Figure 5.21: SAED pattern of Particle 1 showing the AuNi [1 1 1] and Al_2O_3 [0 0 0 1] zone axis. The blue line cut showing the $\{3\,\bar{3}\,0\,0\}$-reflections of α-Al_2O_3 and $\{2\,2\,0\}$-reflections of AuNi. The lattice-parameter of the AuNi-alloy is calculated to 3.88 Å. Due to this and the overlapping of the $\{2\,2\,0\}$-peak and $\{3\,\bar{3}\,0\,0\}$-peak lattice matching is achieved.

In Figure 5.23b the ADF-STEM image of Particle 2 is shown. Triangularly shaped features are visible which could be an indication for edge type dislocations with a line direction in $\langle 1\,1\,0\rangle$ and a Burgers vector of $\frac{a}{6}\langle 2\,1\,1\rangle$ (see Section 3.1). Additionally two-beam STEM investigations were performed on Particle 2, showing periodic lines with a mean distance of 45 nm (Figure 5.24). Due to the invisibility in a two-beam condition with the $[2\,0\,\bar{2}]$ reflection excited, the periodic lines are another indication for the formation of a misfit dislocation network. A detailed discussion can be found in Section 6.8.

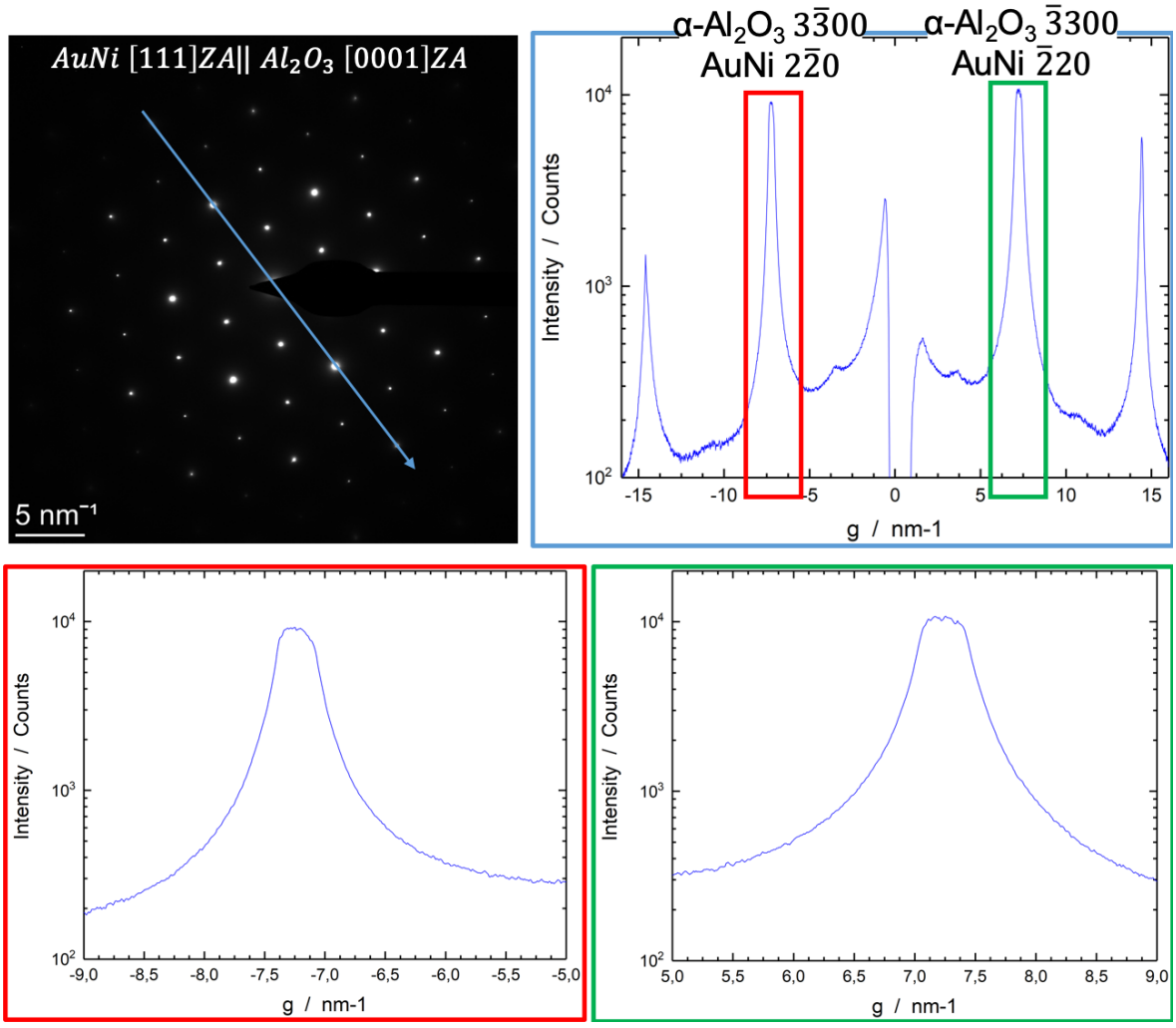

Figure 5.22: SAED pattern of Particle 2 showing the AuNi [1 1 1] and Al_2O_3 [0 0 0 1] zone axes. The blue line cut showing the $\{3\bar{3}00\}$-reflections of α-Al_2O_3 and $\{220\}$-reflections of AuNi. The lattice-parameter of the AuNi-alloy is calculated to 3.89 Å. Due to this and the overlapping of the $\{220\}$-peak and $\{3\bar{3}00\}$-peak lattice matching is achieved.

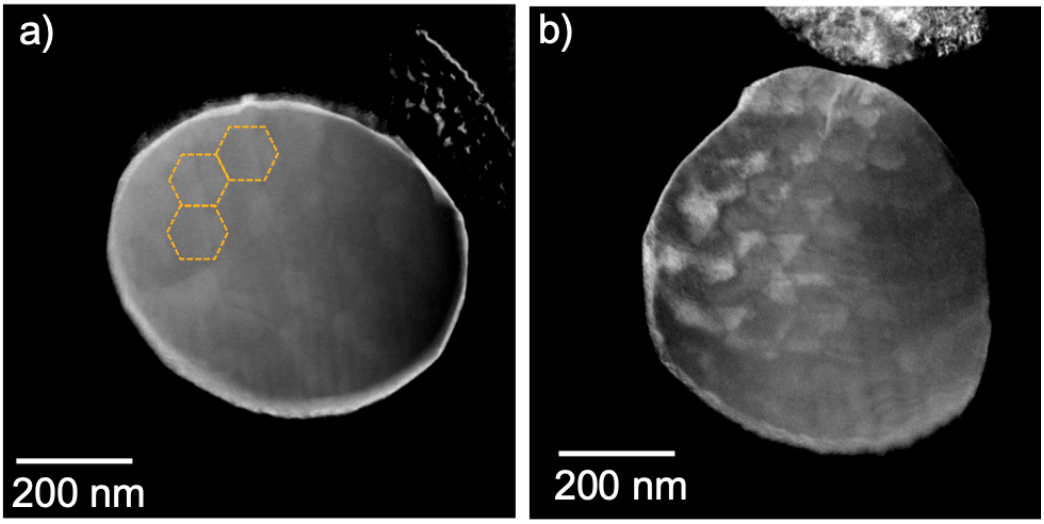

Figure 5.23: a) ADF-STEM image of Particle 1 showing hexagonally arranged lines. The mean distance of the lines parallel to each other is (95 ± 3) nm. b) ADF-STEM image of Particle 2 showing triangularly shaped features.

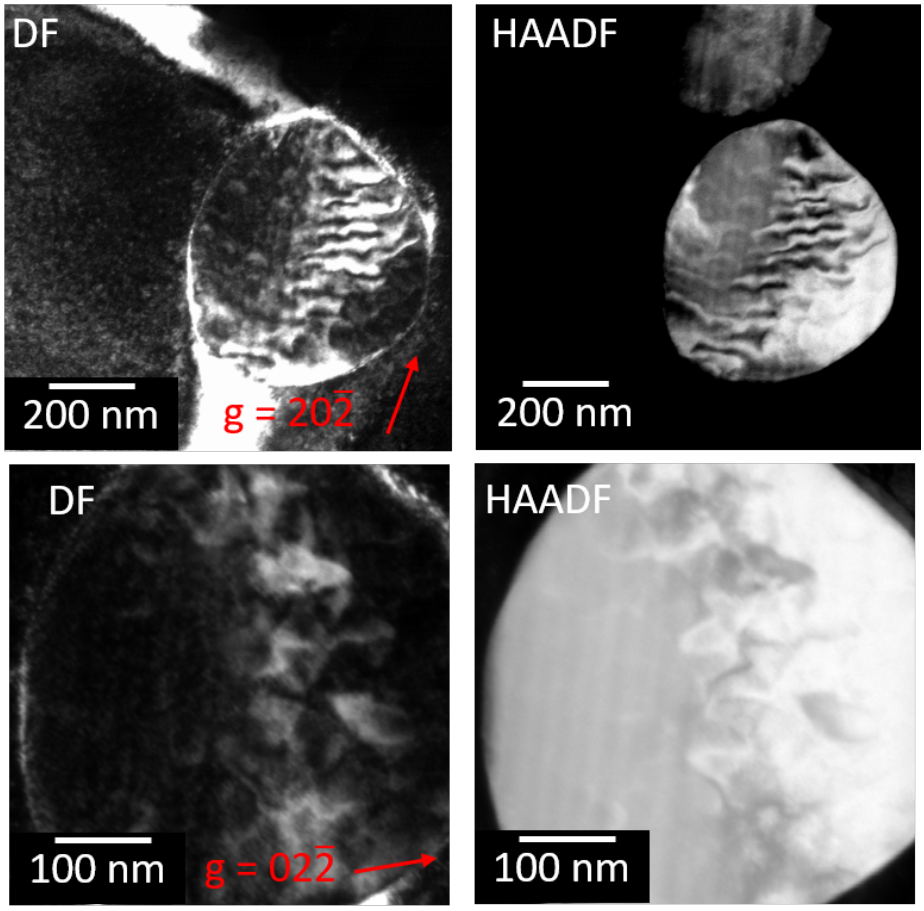

Figure 5.24: Two-beam STEM images of Particle 2. By imaging with $g = [2\,\bar{2}\,0]$ periodic lines are visible with an average spacing of 45 nm. The lines are invisible for an imaging condition with the $g = [0\,2\,\bar{2}]$.

6 Discussion

The following paragraphs summarise the results and provide possible explanations for the observations made.

6.1 Cooling rates of the RTA furnace

Before a successful production of AuNi alloy nanoparticles could be achieved, a parameter study had to be carried out with regard to a sufficiently high cooling rate to avoid segregation of the particles. It was shown in Section 5.1.1 that the cooling rate in vacuum is about $35\,^{\circ}\mathrm{C\,s^{-1}}$ down to a temperature of about 500 °C and then slows down. Although the setting of a gas flow before cooling leads to a clear increase of the cooling rate to over $200\,^{\circ}\mathrm{C\,s^{-1}}$, however, at first sight the cooling rate seems to drop from a certain temperature also here with heating times exceeding 30 s (see Section 5.1.2).
The reason for the decrease in the cooling rate may be a measurement artifact. In the RTP system used here, the temperature is measured by optical pyrometers. The measuring range of the high temperature pyrometer is at temperatures of 400 °C to 1300 °C [64]. In addition the emissivity of the Si-wafer, on which the sample is placed, decreases with decreasing temperature. Thus at low temperatures, also the temperature of the quartz window which is mounted between the sample and the heating lamps (see Figure 4.18) has to be considered. As a result, at low temperatures, both the wafer and the quartz window contribute to the measured temperature. With increasing heating time, the quartz window is getting hotter, which may lead to the observed effect that the cooling rate decreases at temperatures around 400 °C, since the quartz window is not cooled as fast as the wafer (e.g. sample) and influences the measured temperature of the pyrometer.
Zhao et al. [65] developed time-temperature-transformation (TTT) diagrams for an $Au_{50}Ni_{50}$-alloy and an $Au_{40}Ni_{60}$-alloy. According to this work, the onset for discontinuous precipitation at 600 °C leads to an annealing time of 300 s and spinodal decomposition starts at 150 °C after 17 min. Herz et al. [25] argued that for substitutional alloys such as AuNi-alloy, grain boundary diffusion and not volume diffusion is the dominant mechanism in discontinous decomposition, so the TTT diagrams for bulk alloys are also applicable to nanoscale particles. Furthermore, they showed that a cooling rate of

about 9 °C s^{-1} is sufficiently high to produce AuNi alloy particles.
However, as shown in Section 5.1.1, not all particles are completely alloyed despite a cooling rate of over 30 °C s^{-1}. The reason for this could be that without gas flow the heat dissipation on the particle side is slower and thus segregation on the facets and interfaces starts to occur.

6.2 Influence of atmosphere

The influence of the atmosphere during the thermal processing of AuNi bilayer on the NPs has been observed for several cases. While the overall shape of particles treated in vacuum and at atmospheric pressure is the same (see Figure 5.1b,e and Figure 5.8) significant dealloying was observed for the vacuum-treated samples. When processing in vacuum, cooling can only occur via conduction from the substrate. Due to the absence of an atmosphere no convection processes on the particle side are possible which could slow down the cooling process and therefore promote dealloying.
Furthermore in Section 5.2.2 the influence of H_2 on the alloy formation was shown. In difference to the vacuum treated samples, before heating an atmospheric pressure was set using the purging function of the RTP system. Although according to specifications the purging of the chamber takes place by means of inert gas [66], heating times of 90 s and 120 s result in a strong oxidation of Nickel during processing without H_2 (see Figure 5.7), which is attributable to possible oxygen impurities in the gas pipe. In contrast, forming gas consisting of argon and hydrogen (20:1) completely supresses oxidation and round, highly alloyed particles form. The diffractogram has shown that beside the {1 1 1}-oriented particles also {1 0 0}-oriented particles are present. For the discussion of the influence of reducing agents on the out-of-plane texturing of particles processed via solid-state dewetting the reader is referred to Section 6.4.

6.3 Particle shape

Figure 5.8 has visualized that for pure Au and pure Ni a heating time of 120 s at 935 °C is too short to reach the equilibrated state. While the pure Au sample has not reached the particle state at all, the Ni sample is dewetted completely but the majority of the particles are elongated. Smaller particles show a rounder shape, but due to the different aspect ratios of the upward pointing {1 1 1}-facet the ECS is not reached (see Figure 6.1). Several studies on the dewetting behaviour of pure fcc metals like Au [8] and Ni [19, 67] have shown that the time to reach the ECS is much longer.

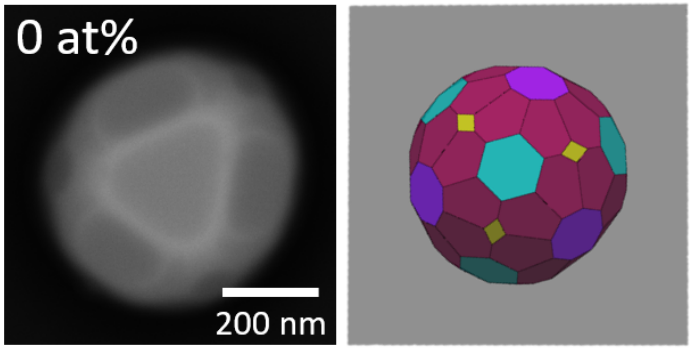

Figure 6.1: Comparison of a pure Ni particle processed in ERL with the simulated ECS of Ni. The ECS of Ni was made using the *Wulffmaker* tool [68] with parameters for equilibrated Ni particles found by Meltzman et al. [69]. By analysing the shape of the facets it is obvious that pure Ni is not equilibrated completely.

The morphological evolution of the alloyed nanoparticles is slightly different. While for a nominal Au concentration of 15 at.% particles with a flat surface can still be seen, particles which have reached the ECS can already be found here. For higher Au concentrations (28 at.% to 70 at.% Au) the shape of the NPs becomes more uniform. As the SEM analysis has shown and was confirmed by the XRD out-of-plane measurements, the particles of the measurement series ERL are not strictly {1 1 1} textured, since particles with a {1 0 0} out-of-plane texture are also present. For indexation of the crystallographic nanofacets the ECS was simulated with the *Wulffmaker* tool [68] (see Figure 6.2b,d). It can be seen that beside the commonly observed {1 1 1} and {1 1 0} facets also higher indexed {1 1 3} facets are present. This is in good agreement with previous studies [67].

Comparing the particle shape from the measurement series ERL (Figure 5.8a-j) and ILM (Figure 5.13a-j) it is noticeable that, although there are also isolated particles that have reached the ECS, the facets of the majority are less pronounced and the particles appear to be more spherical, especially for compositions of 50 at.% and more. One reason for this could be the particle size jump (see Figure 5.13k), since the time required to reach the ECS increases with increasing particle size (see Equation 2.2).

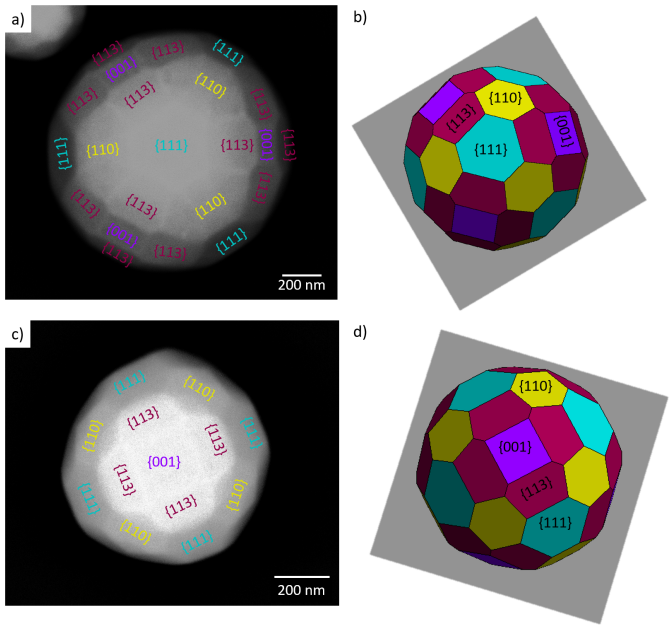

Figure 6.2: BSE-SEM top-view images of alloy nanoparticles with a nominal composition of $Au_{28}Ni_{72}$ showing the two main out-of-plane orientations of {1 1 1} (a) and {1 0 0} (c). The crystallographic facets were indexed using simulated ECS using the *Wulffmaker* tool [68] ((b) and (d) respectively).

6.4 Texture evolution as a function of the Au concentration

Using XRD out-of-plane and in-plane measurements, it was possible to statistically strengthen the observed correlation between the textural evolution of the AuNi particles and the Au concentration. In Figure 5.12b and Figure 5.17b the Bragg-Brentano XRD measurements for the two measurement series were presented. First it can be seen that for all samples (1 1 1)-reflections show up which indicates a (1 1 1) out-of-plane texturing of the particles, which is the energetically favored texture for pure fcc metals on (0 0 0 1)-oriented α-Al_2O_3 [18, 69].

To quantify the grade of texturing the ratio of the integrated intensities of the (1 1 1)- and (2 0 0) AuNi peaks were determined and compared in Figure 6.3 for the two measurement series. Considering the ERL-series, the addition of Au to pure Ni leads to an increase in particles which are ⟨1 0 0⟩ oriented in out-of-plane direction. The reason for the decrease in {1 1 1} texturing could be the increase in alloy-induced stress, since the fcc-lattices of Ni and Au have a large lattice mismatch of about 15 % [70] which can induce a large strain energy during the alloying. To minimize the total energy the

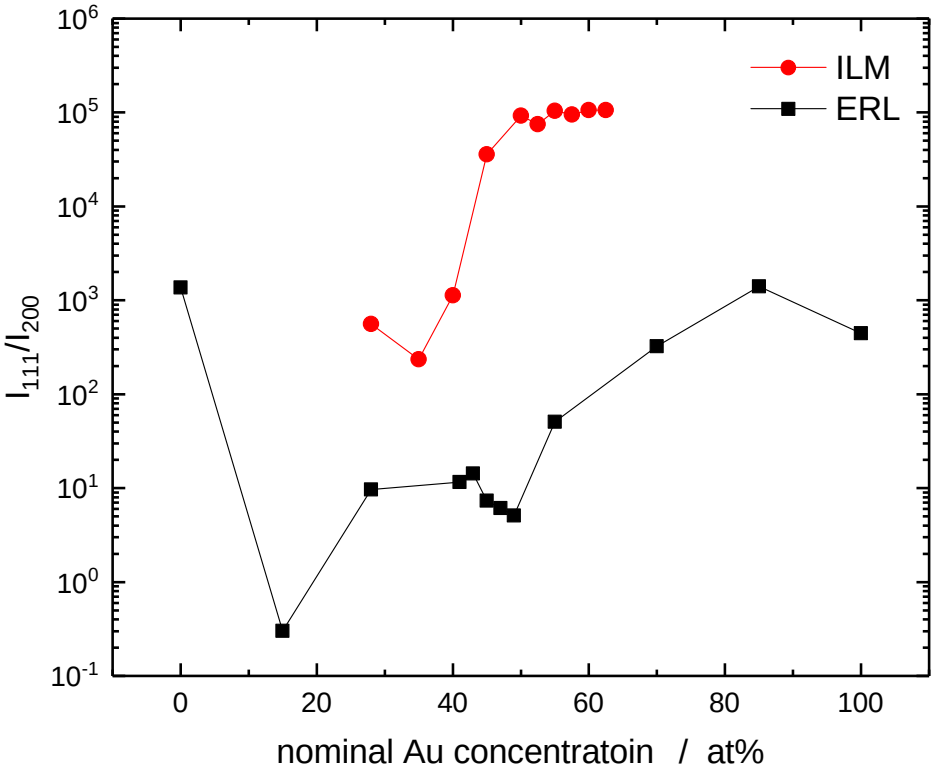

Figure 6.3: Comparison of the grade of texturing of measurement series ERL (black) and ILM (red).

induced strain energy has to be relaxed, which can be done by changing the texture from {1 1 1} to {1 0 0}, since particles with this orientation have the smallest strain energy density [24, 71–73]. Additionally, a significantly higher texturing of the ILM series can be seen. Since there are hardly any {1 0 0} oriented particles in this series of measurements, but the material system is the same, there must be another reason why there is a change in texturing. As already mentioned, the difference between the two measurement series is the H_2 gas flow during thermal processing. While it was 20 sccm for the measurement series ERL, it was raised up to 100 sccm for the measurement series ILM. Previous works have shown that oxygen adsorption can significantly alter the surface energy anisotropy of metals, which can lead to different faceting [74, 75]. Seriani and Mittendorfer [76] have shown that the shape of metallic nanoparticles depends on the oxygen partial pressure during heating. Thus, the typical {1 1 1} faceting without oxygen adsorption occurred in silver and copper, whereas with oxygen adsorption other facets such as {1 0 0} were increasingly formed. Ye and Thompson [77] also showed that the reducing gas flow rate has an influence on which types of facets are present in dewetted Ni films, where at high gas flows {1 1 1}-facets have formed earlier and more distinctly and at low gas flows {2 1 0}-facets are more pronounced. In

Section 5.2.2 it could be shown that without H_2-flow oxidation of nickel occurs. It is therefore obvious that oxidation of the samples can be avoided at low gas flows, but residual oxygen in the process chamber can lead to oxygen adsorption on the samples and thus to reduced {1 1 1}-texturing.

Furthermore, the out-of-plane measurements were used to confirm the impression of alloy formation, which was created by the BSE images. Increasing the Au content leads to a systematic shift of the (1 1 1) reflections to lower scattering angles in both measurement series (see light blue arrows in Figure 5.12b and Figure 5.17b), which is equivalent to an increase in lattice spacing (see Equation 4.4). Another difference between ERL and ILM can be seen in the peak shape. While the peaks of the ERL-series are symmetrical, the XRD profiles of ILM show a more assymetrical form due to a broadening to the Au side. As the SEM analysis has shown (Figure 5.13) some of the particles manufactured in ILM show segregations of Ni. This could lead to an increase of the lattice distances in some of the particles and therefore to the formation of a shoulder of the peaks to the Au-side, since the method used here averages all particles on the wafer.

The in-plane data also support the statement which was made on the basis of the out-of-plane data regarding the alloy formation due to the shift of the (2 2 0) reflections to lower scatering angles. Further important information can also be obtained. First the lattice matching of the $Au_{49}Ni_{51}$ (ERL) and $Au_{45}Ni_{55}$ (ILM) could be confirmed since the (2 2 0) AuNi peak-position is matching with the $(3\,\bar{3}\,0\,0)$ Al_2O_3 peak. It has to be considered that the quantified Au concentrations of these two specific samples differ from each other by about 8 at.% while the difference in the lattice parameter obtained by the out-of-plane measurements is only 0.1 Å. The reason for this could be the Ni precipitates in the ILM measurement series. While in EDX measurements the precipitates contribute to quantification and thus reduce the gold content of the particles, the precipitates are not taken into account in XRD measurements. The absence of Ni in the alloy thus results in a larger lattice parameter being measured.

Moreover the evolution of the lattice-parameter related to the Au concentration could be shown. For the measurement series ERL it was shown that the lattice parameters derived form out-of-plane and in-plane data are overlapping (see Figure 5.12d), which makes the exclusion of a tetragonal distortion of the particles possible. Furthermore the evolution of the lattice paramter of both series shows a deviation from Vegard‘s law and fits very well to the data for bulk AuNi-alloys obtained by Crawley et al. [60].

It is a common phenomenon that there is a deviation from Vegard's law [78].

6.5 Diffuse background of in-plane measurements

In the in-plane diffractogram of the measurement series ILM a diffuse background can be seen symmetrically distributed around the {2 2 0} peaks of the particles (Figure 5.17c). In 2012 Meltzman et al. introduced the theory of delocalized coherency regarding the interface of equilibrated Ni particles on sapphire. It is mentioned that the terminating Ni layer buckles in a periodic manner according to the coincidence symmetry of the involved lattices to reduce strain energy, which could not be minimized by misfit dislocations due to the high lattice mismatch [19]. Herre mentioned, according to WBDF images, that also in equilibrated AuNi-particles with a mismatch of 4 % to the substrate a reconstructed interface is present [67]. Due to the high surface sensitivity of in-plane measurements the buckled terminating AuNi-layer of the particles could be the reason for the diffuse background. Interestingly, the background almost disappears at a nominal gold content of 45 at.%. By TEM diffraction it was shown that the misfit of these particles and the substrate is close to zero and thus the terminating AuNi layer should't be buckled anymore since the formation of misfit dislocations is energetically preferable.
The absence of the diffuse background in the measurement series ERL reveals a lack of interaction between the particles and the substrate. It was shown that the ERL-particles have a lower {1 1 1}-texturing and therefore a lower in-plane interaction of the {2 2 0} AuNi-planes and the $\{3\,\bar{3}\,0\,0\}$-planes of sapphire.

6.6 Preferred orientation relationship between substrate and particles

Using XRD pole figures, the orientation relationship between the particles and the substrate was obtained. It is shown that the main orientation relationship for the AuNi nanoparticles and the substrate is $\{1\,1\,1\}\pm\langle 1\,1\,0\rangle$ AuNi $\parallel (0\,0\,0\,1)\langle 1\,0\,\bar{1}\,0\rangle\alpha$-$Al_2O_3$ (OR1) (see Figure 6.4a), where the "±" indicates the two symmetrical equivalent twin variants differing by a rotation of 180° around the $\langle 1\,1\,1\rangle$ surface normal (also see red marks in Figure 5.19a). This is in good agreement with earlier studies for similar material systems like Cu and Al thin films on sapphire [17, 18, 79] and for equilibrated Ni particles on sapphire [19]. In these studies beside this orientation relationship (OR1)

a second one was investigated which is shifted about 30° with respect to OR1, which could not be identified for the AuNi-particles investigated in this thesis. Instead it was shown in the pole figures that beside the twins with OR1 there are two further pairs of twins, rotated by ± 18°. According to the simulated diffraction pattern (see Figure A.2) a rotation of 19.11° would lead to an orientation relation of $\{1\,1\,1\}\pm\langle\bar{3}\,2\,0\rangle$ AuNi ‖ $(0\,0\,0\,1)\langle1\,0\,\bar{1}\,0\rangle\alpha$-$Al_2O_3$. The analysis of the FWHM of the pole-figure reflections has shown that the rotated particles show a rotation of $(18 \pm 2)°$ and therefore it can be assumed that an in-plane relation of AuNi $\langle\bar{3}\,2\,1\rangle$ ‖ α-Al_2O_3 $\langle1\,0\,\bar{1}\,0\rangle$ exists (see also Figure 6.4b).

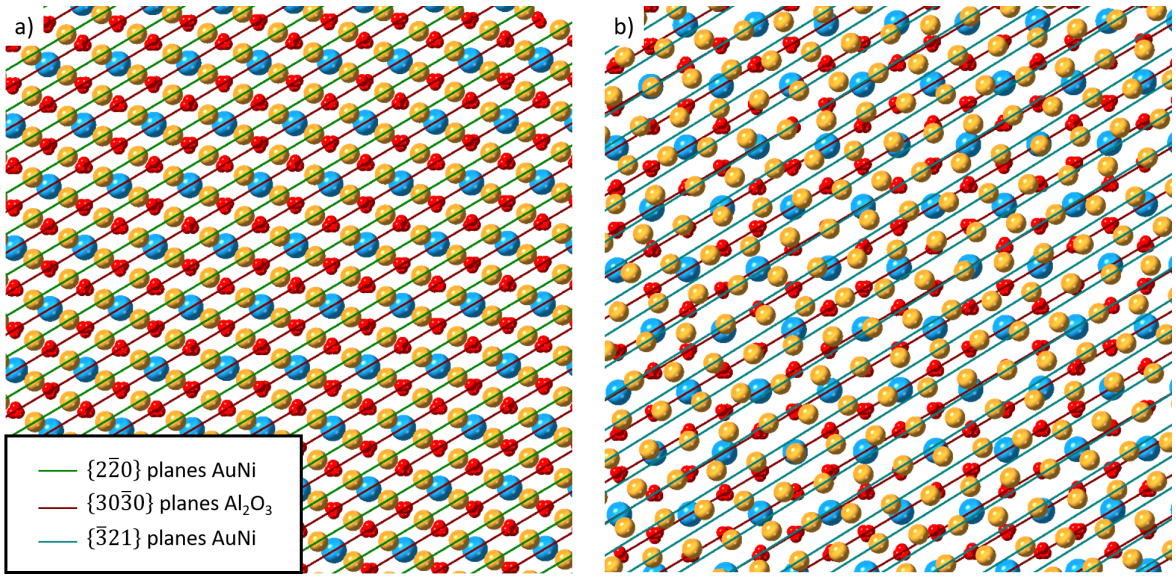

Figure 6.4: Schematic visualization of the two different orientation relationships: a) OR1 where the AuNi $\{2\,\bar{2}\,0\}$ planes are parallel to the α-Al_2O_3 $\{3\,0\,\bar{3}\,0\}$ planes. b) OR2 where the AuNi $\{\bar{3}\,2\,1\}$ planes are nearly parallel to the α-Al_2O_3 $\{3\,0\,\bar{3}\,0\}$ planes.

6.7 TEM investigations

Based on the XRD investigations it was shown that particles of the measurement series ILM with a nominal gold concentration of 45 at.% achieved lattice matching. However, since these investigations averaged over all particles on the substrate, correlated TEM investigations were carried out on two particles to check the significance for individual particles.

The linescans of Particle 1 (Figure 5.21) reveal a small shoulder at the AuNi $(\bar{2}\,2\,0)$ spot at a smaller g-value. However, this is not due to a difference in lattice spacing, otherwise splitting to smaller g-vectors would be observed at all spots. When looking

at the AuNi spots (Figure 6.5), however, it can be seen that this is not the case. Nevertheless, it was shown that dislocation lines have formed in the particle due to the low misfit. Since a small SAED aperture was used for the diffraction image, so that only diffracted rays from the particle center contribute, it can be assumed that the splitting is due to a misfit dislocation.

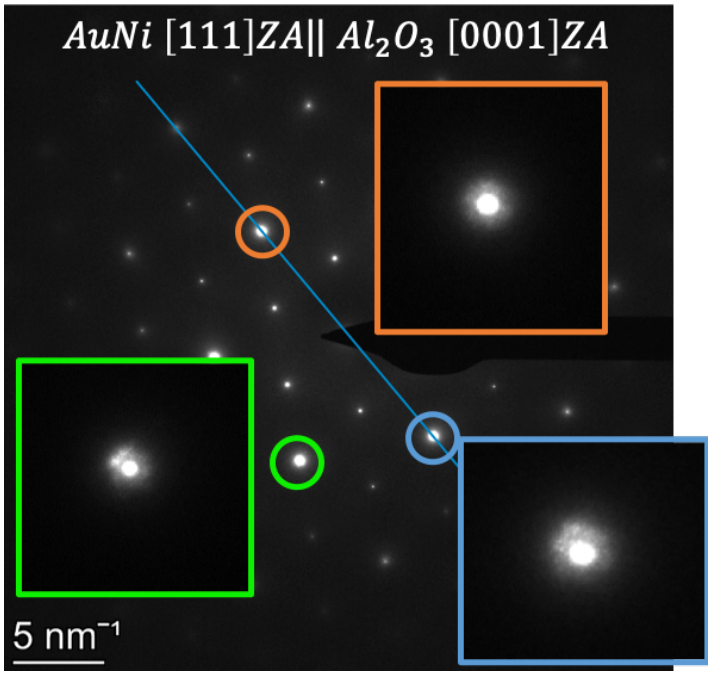

Figure 6.5: Enhanced view of three overlapping AuNi $\{2\,2\,0\}$/α-Al_2O_3 $\{3\,0\,\bar{3}\,0\}$-reflections. The splitting of the peaks is not attributed to a difference in the lattice parameter of the particles and the substrate as there is no regular splitting to smaller or larger g-values.

Thus, according to the SAED-pattern showing the $[1\,1\,1]$ AuNi-ZA ∥ $[0\,0\,0\,1]$ α-Al_2O_3-ZA (see Figure 5.21 and Figure 5.22), it can be concluded that no splitting between the AuNi $\{2\,2\,0\}$ spots and the α-Al_2O_3 $\{3\,0\,\bar{3}\,0\}$ spots can be found and therefore it could be confirmed that the investigations done by XRD are also valid for single particles and lattice matching is achieved.

6.8 Formation of misfit dislocations

It has already been discussed that the absence of the diffuse signal in the in-plane diffractogram of the sample ILM45 indicates a change in the interface structure due to the absence of the diffuse signal. Additionally in Section 5.3.2.4 hexagonal (Particle 1) and triangular (Particle 2) features show up in the STEM images of the correspondig particle.

By comparing the features with the MD-investigations on semi-coherent interfaces of the Al/α-Al_2O_3-system done by Pilania et al. [38] (see Figure 3.2) the impression gained by in-plane XRD is reinforced. Their simulations have shown that a misfit dislocation network of pure edge-dislocations is formed with line directions in $\langle 1\,1\,0\rangle$ and Burgers vectors of $\frac{a}{6}\langle\overline{2}\,1\,1\rangle$. The relaxed structure model showed hexagonal coherent areas which are separated by the dislocation lines from triangularly shaped stacking-fault areas. Regarding the hexagonal features visible in Particle 1, the mean distance of the lines is about 95 nm. By using Equation 3.1, with a Burger's vector of $\frac{a}{6}\langle\overline{2}\,1\,1\rangle$ the mismatch of Particle 1 and the substrate is calculated to 0.2 %, leading to a lattice parameter of 3.87 Å which is in good agreement with the SAED and the XRD results. For Particle 2 also two-beam STEM was done (Figure 5.24) showing periodic lines with a mean distance of 45 nm, which are invisible for imaging with a g-vector of $[0\,2\,\overline{2}]$. Following Pilania et al. the dislocations are of pure edge-character, which is why it can be assumed that they are located in the $(1\,1\,1)$ plane of the particles. Therefore a second invisibility criteria for the dislocation line should be an image-condition with the $[1\,1\,1]$ g-vector. Thus, the Burgers vector of the dislocations of Particle 2 are parallel to the $[\overline{4}\,2\,2]$ direction. The most stable configuration would therefore be a Burgers vector of $\frac{a}{6}\langle\overline{2}\,1\,1\rangle$. Then, by again calculating the lattice mismatch with Equation 3.1 to 0.35 %, a lattice parameter of 3.88 Å is calculated, matching very well to the experimental results of 3.89 Å (SAED) and 3.88 Å (XRD).
The difference in the pattern showing up (hexagonal and triangular) could be due to different equilibrated states of the particles, since a further equilibration of the misfit dislocation pattern leads to a rigid shift of the dislocation lines forming a triangularly shaped pattern of coherent and stacking-fault areas [38]. Whether the different twin variant of OR1 plays a major role here, has to be tested statistically by additional lift-outs of plan-view lamellas.

It has to be stated that the observations made here are no proof for the formation of a misfit dislocation network, but nevertheless through the absence of the diffuse signal in the in-plane measurements and the features showing up in the STEM-investigations the assumption of a change in the interface structure from a delocalized semi-coherent interface to a semi-coherent where the strain at the interface is accomodated by dislocations is very obvious.

7 Summary and outlook

In this work, Au_xNi_{1-x} alloy nanoparticles were succesfully produced via the solid-state dewetting of AuNi bilayers. For this reason the bilayers were rapid thermal annealed at 935 °C for 120 s with a subsequent quenching. By correlative XRD and SEM investigations it was shown that the atmosphere during heating has a strong influence on both the alloy formation and the texturing of the particles. While the absence of a reducing agent during processing leads to a complete oxidation of Ni, Au_xNi_{1-x} nanoparticles were produced using a reducing atmosphere. The homogeneity of the particles was confirmed by EDX, BSE and XRD in a correlative manner. The average size of the particles is in the range of 400 nm. However, the stability of the thin films increases with the Au content, and in particular for Au contents above 50 % larger particles are observed. By varying the Au concentration, the lattice parameter of the NP was systematically controlled. XRD out-of-plane measurements reveal a predominant (1 1 1) texturing for high H_2-flow rates, while samples produced with low H_2-flow rates have only a low (1 1 1) texturing. The combination of XRD out-of-plane and in-plane measurements reveal a pronounced AuNi (1 1 1) [1 $\bar{1}$ 0] ∥ α-Al_2O_3 (0 0 0 1) [1 0 $\bar{1}$ 0] orientation relationship (OR1) for the samples produced at high H_2 flow rates (ILM). Additional (1 1 1) AuNi XRD pole figures of these samples reveal the existance of two twin variants within OR1. In addition, two further twin variants can be found where the particles are rotated by ±18 degrees around the ⟨1 1 1⟩ surface normal, changing the orientation relation to AuNi (1 1 1) [$\bar{3}$ 2 1] ∥ α-Al_2O_3 (0 0 0 1) [1 0 $\bar{1}$ 0] (OR2). Interestingly, the ratio of OR2 to OR1 increases with increasing Au concentration, which could stem from different Au-dependent interface energetics. Furthermore within the in-plane measurements a diffuse background was found for NPs with a lattice mismatch >1 % originating from a buckling of the terminating layer at the interface (delocalized coherent interface). The vanishing of the diffuse signal for particles with 55 at.% Au indicates a change in the interface structure from a delocalized coherent interface to a semi-coherent interface. Interestingly, the size and degree of texturing changes in a stepwise manner in the same concentration regime. This might be correlated to a sudden change in the interface energetics due to the formation of a semi-coherent interface.

TEM studies of two single particles with a composition of $Au_{55}Ni_{45}$ in plan view reveal

the succesful matching of the alloy- and α-Al_2O_3-lattice parameter due to the overlap of the $\{2\,2\,0\}$ AuNi and $\{3\,0\,\bar{3}\,0\}$ α-Al_2O_3 reflections in the SAED-measurements. Furthermore STEM studies of the particle-substrate interface reveal the formation of a misfit dislocation network due to the formation of hexagonal (Twin 1) and triangular (Twin 2) shaped features. Following Pilania et al. [38] a dislocation network consisting of dislocations with a line direction in $\langle 1\,1\,0\rangle$ and a Burgers vector of $\frac{a}{6}\langle\bar{2}\,1\,1\rangle$ has formed.

The next step is to achieve high cooling rates in combination with high gas flows with the RTP system from ANNEALSYS. Then, a systematic investigation of the influence of H_2 during thermal processing on texturing by changing the H_2 flow rate from low to higher values can be performed. Furthermore, further plan-view and additional cross-sectional investigations of the particle-substrate interface can be implemented to get a detailed characterization of the misfit dislocation network. With the help of cross-sectional TEM lamellas also the influence of the lattice matching and the type of misfit (positive and negative) on the segregation behaviour of Au and Ni at the interface can be investigated. Additionally *in situ* SEM-manipulation of the particles can be used to measure the influence of the lattice matching on the adhesion of the particles on the substrate.

References

[1] C. V. Thompson, "Solid-state dewetting of thin films", *Annual review of materials research*, vol. 42, no. 1, pp. 399–434, Aug. 2012. DOI: 10.1146/annurev-matsci-070511-155048 (cit. on pp. 1, 3, 4).

[2] M. Yoshitake, S. Yagyu, and T. Chikyow, "Novel method for the prediction of an interface bonding species at alumina/metal interfaces", *Journal of vacuum science & technology a: Vacuum, surfaces, and films*, vol. 32, no. 2, p. 021 102, Mar. 2014. DOI: 10.1116/1.4849375 (cit. on p. 1).

[3] W. Wunderlich, "The atomistic structure of metal/ceramic interfaces is the key issue for developing better properties", *Metals*, vol. 4, no. 3, pp. 410–427, Aug. 2014. DOI: 10.3390/met4030410 (cit. on p. 1).

[4] J. Y. Park, L. R. Baker, and G. A. Somorjai, "Role of hot electrons and metal–oxide interfaces in surface chemistry and catalytic reactions", *Chemical reviews*, vol. 115, no. 8, pp. 2781–2817, Mar. 2015. DOI: 10.1021/cr400311p (cit. on p. 1).

[5] M. Ruhle and A. G. Evans, *Metal-ceramic interfaces: Proceedings of an international workshop (acta-scripta metallurgica proce)*. Pergamon, 2013, ISBN: 9781483287461 (cit. on p. 1).

[6] M. F. Niekiel, "Solid-state dewetting of metallic thin films studied by advanced in situ electron microscopy techniques", PhD thesis, Friedrich-Alexander-Universität Erlangen-Nürnberg, 2017 (cit. on p. 3).

[7] T. Young, "III. An essay on the cohesion of fluids", *Philosophical transactions of the royal society of london*, vol. 95, pp. 65–87, Jan. 1805. DOI: 10.1098/rstl.1805.0005 (cit. on p. 4).

[8] H. Sadan and W. D. Kaplan, "Au–sapphire (0001) solid–solid interfacial energy", *Journal of materials science*, vol. 41, no. 16, pp. 5099–5107, Jul. 2006. DOI: 10.1007/s10853-006-0437-5 (cit. on pp. 4–6, 72).

[9] W. D. Kaplan, D. Chatain, P. Wynblatt, and W. C. Carter, "A review of wetting versus adsorption, complexions, and related phenomena: The rosetta stone of wetting", *Journal of materials science*, vol. 48, no. 17, pp. 5681–5717, Jun. 2013. DOI: 10.1007/s10853-013-7462-y (cit. on pp. 4, 5).

[10] W. W. Mullins, "Theory of thermal grooving", *Journal of applied physics*, vol. 28, no. 3, pp. 333–339, Mar. 1957. DOI: 10.1063/1.1722742 (cit. on p. 4).

[11] D. J. Srolovitz and S. A. Safran, "Capillary instabilities in thin films. I. Energetics", *Journal of applied physics*, vol. 60, no. 1, pp. 247–254, Jul. 1986. DOI: 10.1063/1.337689 (cit. on p. 4).

[12] E. Shaffir, I. Riess, and W. Kaplan, "The mechanism of initial de-wetting and detachment of thin au films on YSZ", *Acta materialia*, vol. 57, no. 1, pp. 248–256, Jan. 2009. DOI: 10.1016/j.actamat.2008.09.004 (cit. on p. 4).

[13] R. Brandon and F. Bradshaw, "The mobility of the surface atoms of copper and silver evaporated deposits", Royal aircraft establishment Farnborough (United Kingdom), Tech. Rep., 1966 (cit. on p. 4).

[14] O. Kovalenko, J. Greer, and E. Rabkin, "Solid-state dewetting of thin iron films on sapphire substrates controlled by grain boundary diffusion", *Acta materialia*, vol. 61, no. 9, pp. 3148–3156, May 2013. DOI: 10.1016/j.actamat.2013.01.062 (cit. on p. 4).

[15] A. Kosinova, O. Kovalenko, L. Klinger, and E. Rabkin, "Mechanisms of solid-state dewetting of thin au films in different annealing atmospheres", *Acta materialia*, vol. 83, pp. 91–101, Jan. 2015. DOI: 10.1016/j.actamat.2014.09.049 (cit. on p. 4).

[16] F. Niekiel, S. M. Kraschewski, P. Schweizer, B. Butz, and E. Spiecker, "Texture evolution and microstructural changes during solid-state dewetting: A correlative study by complementary in situ TEM techniques", *Acta materialia*, vol. 115, pp. 230–241, Aug. 2016. DOI: 10.1016/j.actamat.2016.05.026 (cit. on p. 4).

[17] G. Dehm, H. Edongué, T. Wagner, S. Oh, and E. Arzt, "Obtaining different orientation relationships for Cu films grown on (0001) α-Al2O3 substrates by magnetron sputtering", *Zeitschrift für metallkunde*, vol. 96, no. 3, pp. 249–254, Mar. 2005. DOI: 10.3139/146.101027 (cit. on pp. 5, 77).

[18] S. Hieke, B. Breitbach, G. Dehm, and C. Scheu, "Microstructural evolution and solid state dewetting of epitaxial al thin films on sapphire", *Acta materialia*, vol. 133, pp. 356–366, Jul. 2017. DOI: 10.1016/j.actamat.2017.05.026 (cit. on pp. 5, 74, 77).

[19] H. Meltzman, D. Mordehai, and W. D. Kaplan, "Solid–solid interface reconstruction at equilibrated Ni–Al2O3 interfaces", *Acta materialia*, vol. 60, no. 11, pp. 4359–4369, Jun. 2012. DOI: 10.1016/j.actamat.2012.04.037 (cit. on pp. 5, 10, 11, 72, 77).

[20] L. Rayleigh, "On the instability of jets", *Proceedings of the london mathematical society*, vol. s1-10, no. 1, pp. 4–13, Nov. 1878. DOI: 10.1112/plms/s1-10.1.4 (cit. on p. 5).

[21] G. Wulff, "XXV. Zur Frage der Geschwindigkeit des Wachsthums und der Auflösung der Krystallflächen", *Zeitschrift für kristallographie - crystalline materials*, vol. 34, no. 1-6, Jan. 1901. DOI: 10.1524/zkri.1901.34.1.449 (cit. on p. 5).

[22] W. Winterbottom, "Equilibrium shape of a small particle in contact with a foreign substrate", *Acta metallurgica*, vol. 15, no. 2, pp. 303–310, Feb. 1967. DOI: 10.1016/0001-6160(67)90206-4 (cit. on p. 6).

[23] F. Nichols and W. Mullins, "Surface-(interface-) and volume-diffusion contributions to morphological changes driven by capillarity", *Trans. metall. soc. aime*, vol. 233, no. 10, pp. 1840–1848, 1965 (cit. on p. 6).

[24] D. Wang and P. Schaaf, "Ni–Au bi-metallic nanoparticles formed via dewetting", *Materials letters*, vol. 70, pp. 30–33, Mar. 2012. DOI: 10.1016/j.matlet.2011.11.102 (cit. on pp. 6, 75).

[25] A. Herz, D. Wang, R. Müller, and P. Schaaf, "Formation of supersaturated Au–Ni nanoparticles via dewetting of an Au/Ni bilayer", *Materials letters*, vol. 102-103, pp. 22–25, Jul. 2013. DOI: 10.1016/j.matlet.2013.03.096 (cit. on pp. 7, 32, 71).

[26] A. Herz, M. Friák, D. Rossberg, M. Hentschel, F. Theska, D. Wang, D. Holec, M. Šob, O. Schneeweiss, and P. Schaaf, "Facet-controlled phase separation in supersaturated Au-Ni nanoparticles upon shape equilibration", *Applied physics letters*, vol. 107, no. 7, p. 073 109, Aug. 2015. DOI: 10.1063/1.4928627 (cit. on p. 7).

[27] J. Petersen and S. G. Mayr, "Dewetting of ni and NiAg solid thin films and formation of nanowires on ripple patterned substrates", *Journal of applied physics*, vol. 103, no. 2, p. 023 520, Jan. 2008. DOI: 10.1063/1.2832758 (cit. on p. 7).

[28] A. Herz, D. Wang, T. Kups, and P. Schaaf, "Solid-state dewetting of Au/Ni bilayers: The effect of alloying on morphology evolution", *Journal of applied physics*, vol. 116, no. 4, p. 044 307, Jul. 2014. DOI: 10.1063/1.4891448 (cit. on p. 7).

[29] A. Herz, F. Theska, D. Rossberg, T. Kups, D. Wang, and P. Schaaf, "Solid-state dewetting of Au–Ni bi-layer films mediated through individual layer thickness and stacking sequence", *Applied surface science*, vol. 444, pp. 505–510, Jun. 2018. DOI: 10.1016/j.apsusc.2018.03.096 (cit. on p. 7).

[30] X. Cen, A. M. Thron, X. Zhang, and K. van Benthem, "Cross-sectional characterization of the dewetting of a au/ni bilayer film", *Ultramicroscopy*, vol. 178, pp. 131–139, Jul. 2017. DOI: 10.1016/j.ultramic.2016.06.004 (cit. on p. 8).

[31] X. Cen, A. M. Thron, and K. van Benthem, "In-situ study of the dewetting behavior of Au/Ni bilayer films supported by a SiO2/Si substrate", *Acta materialia*, vol. 140, pp. 149–156, Nov. 2017. DOI: 10.1016/j.actamat.2017.08.027 (cit. on p. 8).

[32] H. Barda and E. Rabkin, "Improving the thermal stability of nickel thin films on sapphire by a minor alloying addition of gold", *Applied surface science*, vol. 484, pp. 1070–1079, Aug. 2019. DOI: 10.1016/j.apsusc.2019.04.176 (cit. on p. 8).

[33] D. Wolf and S. Yip, *Materials interfaces: Atomic-level structure and properties*. Springer Science & Business Media, 1992 (cit. on p. 9).

[34] R. E. Smallman, *Modern physical metallurgy*. Elsevier LTD, Oxford, Nov. 4, 2013, ISBN: 0080982042 (cit. on p. 9).

[35] R. Smallman and A. Ngan, "Surfaces, grain boundaries and interfaces", in *Modern physical metallurgy*, Elsevier, 2014, pp. 415–442. DOI: 10.1016/b978-0-08-098204-5.00010-9 (cit. on p. 10).

[36] G. Dehm, C. Scheu, M. Rühle, and R. Raj, "Growth and structure of internal Cu/Al2O3 and Cu/Ti/Al2O3 interfaces11Paper presented at Sympos. Synergistic Synthesis of Inorganic Materials, March 1996, Schloß Ringberg, Germany.", *Acta materialia*, vol. 46, no. 3, pp. 759–772, Jan. 1998. DOI: 10.1016/s1359-6454(97)00257-7 (cit. on p. 10).

[37] T. Sasaki, K. Matsunaga, H. Ohta, H. Hosono, T. Yamamoto, and Y. Ikuhara, "Atomic and electronic structures of Cu/a-Al2O3 interfaces prepared by pulsed-laser deposition", *Science and technology of advanced materials*, vol. 4, no. 6, pp. 575–584, Jan. 2003. DOI: 10.1016/j.stam.2003.12.003 (cit. on p. 10).

[38] G. Pilania, B. J. Thijsse, R. G. Hoagland, I. Lazić, S. M. Valone, and X.-Y. Liu, "Revisiting the Al/Al2O3 Interface: Coherent Interfaces and Misfit Accommodation", *Scientific reports*, vol. 4, no. 1, Mar. 2014. DOI: 10.1038/srep04485 (cit. on pp. 10, 11, 80, 82).

[39] T. Massalski, "Binary alloys phase diagrams", *Ams international*, 1992 (cit. on p. 13).

[40] P. K. S. S. Harsha, *Principles of vapor deposition of thin films*. Elsevier Science & Technology, Dec. 16, 2005, 1176 pp., ISBN: 008044699X (cit. on p. 14).

[41] A. Rigort and J. M. Plitzko, "Cryo-focused-ion-beam applications in structural biology", *Archives of biochemistry and biophysics*, vol. 581, pp. 122–130, Sep. 2015. DOI: 10.1016/j.abb.2015.02.009 (cit. on pp. 16, 20).

[42] *FEI Helios Nanolab 660 data sheet*, FEI, 2013 (cit. on pp. 16, 19).

[43] B. Hafner, "Scanning electron microscopy primer", 2007 (cit. on p. 17).

[44] L. Reimer, *Scanning electron microscopy*. Springer Berlin Heidelberg, Dec. 1, 2010, 544 pp., ISBN: 3642083722 (cit. on p. 17).

[45] J. Goldstein, D. E. Newbury, D. C. Joy, C. E. Lyman, P. Echlin, E. Lifshin, L. Sawyer, and J. Michael, *Scanning Electron Microscopy and X-Ray Microanalysis: Third Edition*. Springer, 2012, ISBN: 978-1-4615-0215-9 (cit. on pp. 17–19).

[46] https://physics.nist.gov/PhysRefData/ASD/ionEnergy.html (cit. on p. 18).

[47] A. J. Wilkinson and T. B. Britton, "Strains, planes, and EBSD in materials science", *Materials today*, vol. 15, no. 9, pp. 366–376, Sep. 2012. DOI: 10.1016/s1369-7021(12)70163-3 (cit. on pp. 18, 19).

[48] N. Yao, *Focused ion beam systems: Basics and applications*. Cambridge University Press, 2007 (cit. on pp. 19, 20).

[49] S. Reyntjens and R. Puers, "A review of focused ion beam applications in microsystem technology", *Journal of micromechanics and microengineering*, vol. 11, no. 4, pp. 287–300, Jul. 2001. DOI: 10.1088/0960-1317/11/4/301 (cit. on pp. 19, 20).

[50] C. B. C. David B. Williams, *Transmission electron microscopy*. Springer US, Jul. 31, 2009 (cit. on pp. 20–23).

[51] B. Fultz and J. Howe, *Transmission electron microscopy and diffractometry of materials*. Springer Berlin Heidelberg, 2013. DOI: 10.1007/978-3-642-29761-8 (cit. on p. 22).

[52] C. Evans, R. Brundle, and Wilson, *Encyclopedia of materials characterization: Surfaces, interfaces, thin films (materials characterization series)*. Butterworth-Heinemann, 1992, ISBN: 0750691689 (cit. on pp. 23, 25).

[53] M. Birkholz, *Thin film analysis by x-ray scattering*. Wiley-VCH, 2005, ISBN: 9783527310524 (cit. on pp. 24–26).

[54] W. D. Callister and W. D. C. Jr., *Fundamentals of materials science and engineering, 5th edition*. Wiley, 2000, ISBN: 0-471-39551-X (cit. on p. 24).

[55] C. Hammond, *The basics of crystallography and diffraction*. Oxford University Press, Jun. 11, 2015, 544 pp., ISBN: 0198738684 (cit. on p. 25).

[56] K. Inaba, "X-ray thin-film measurement techniques", *Overview. rigaku j*, vol. 24, no. 1, 2008 (cit. on p. 25).

[57] K. Omote and J. Harada, "Grazing-incidence X-Ray diffractometer for determining In-plane structure of thin films", *Advances in x-ray analysis*, vol. 43, pp. 192–200, 2000 (cit. on pp. 26, 27).

[58] K. Nagao and E. Kagami, "X-ray thin film measurement techniques vii. pole figure measurement", *The rigaku journal*, vol. 27, no. 2, pp. 6–14, 2011 (cit. on pp. 27, 28).

[59] J. Will and P. Herre, "Correlative TEM and XRD study of the role of Au on the solid state dewetting behavior of Au/Ni bilayers on α - Al_2O_3" (cit. on pp. 28–31).

[60] A. F. Crawley and D. J. Fabian, "A Redetermination of the Lattice Spacings and Densities of Gold-Nickel Solutions", *Journal of the institute of metals*, 1966 (cit. on pp. 29, 30, 55, 56, 65, 76).

[61] L. Vegard, "Die Konstitution der Mischkristalle und die Raumfüllung der Atome", *Zeitschrift für physik*, vol. 5, no. 1, pp. 17–26, Jan. 1921. DOI: 10.1007/bf01349680 (cit. on pp. 29, 56, 65).

[62] A. R. Denton and N. W. Ashcroft, "Vegard's law", *Physical review a*, vol. 43, no. 6, pp. 3161–3164, Mar. 1991. DOI: 10.1103/physreva.43.3161 (cit. on p. 29).

[63] *Rapid Thermal Processor AS-One 100 – Installation Manual*, 2.16, ANNEALSYS, Oct. 2017 (cit. on p. 33).

[64] *Rapid Thermal Processor AS-One 100 – User's Manual*, 2.15, ANNEALSYS, Oct. 2017 (cit. on pp. 33, 71).

[65] J.-C. Zhao and M. R. Notis, "Ordering transformation and spinodal decomposition in Au-Ni alloys", *Metallurgical and materials transactions a*, vol. 30, no. 3, pp. 707–716, Mar. 1999. DOI: 10.1007/s11661-999-0062-4 (cit. on p. 71).

[66] *Rapid Thermal Processor AS-One 100 - Functional acceptance protocol*, 1.14, ANNEALSYS, Oct. 2017 (cit. on p. 72).

[67] P. Herre, "Deformation and breakage behavior of complex ceramic and metallic particles", PhD thesis, Friedrich-Alexander-Universität Erlangen-Nürnberg, 2018 (cit. on pp. 72, 73, 77).

[68] R. V. Zucker, D. Chatain, U. Dahmen, S. Hagège, and W. C. Carter, "New software tools for the calculation and display of isolated and attached interfacial-energy minimizing particle shapes", *Journal of materials science*, vol. 47, no. 24, pp. 8290–8302, Aug. 2012. DOI: 10.1007/s10853-012-6739-x (cit. on pp. 73, 74).

[69] H. Meltzman, D. Chatain, D. Avizemer, T. M. Besmann, and W. D. Kaplan, "The equilibrium crystal shape of nickel", *Acta materialia*, vol. 59, no. 9, pp. 3473–3483, May 2011. DOI: 10.1016/j.actamat.2011.02.021 (cit. on pp. 73, 74).

[70] C. Wolverton and A. Zunger, "Ni-Au: A testing ground for theories of phase stability", *Computational materials science*, vol. 8, no. 1-2, pp. 107–121, May 1997. DOI: 10.1016/s0927-0256(97)00023-2 (cit. on p. 74).

[71] C. V. Thompson and R. Carel, "Stress and grain growth in thin films", *Journal of the mechanics and physics of solids*, vol. 44, no. 5, pp. 657–673, May 1996. DOI: 10.1016/0022-5096(96)00022-1 (cit. on p. 75).

[72] C. V. Thompson, "Structure evolution during processing of polycrystalline films", *Annual review of materials science*, vol. 30, no. 1, pp. 159–190, Aug. 2000. DOI: 10.1146/annurev.matsci.30.1.159 (cit. on p. 75).

[73] E. Rabkin, D. Amram, and E. Alster, "Solid state dewetting and stress relaxation in a thin single crystalline Ni film on sapphire", *Acta materialia*, vol. 74, pp. 30–38, Aug. 2014. DOI: 10.1016/j.actamat.2014.04.020 (cit. on p. 75).

[74] J. Ye, D. Zuev, and S. Makarov, "Dewetting mechanisms and their exploitation for the large-scale fabrication of advanced nanophotonic systems", *International materials reviews*, vol. 64, no. 8, pp. 439–477, Dec. 2018. DOI: 10.1080/09506608.2018.1543832 (cit. on p. 75).

[75] H. Mykura, "The variation of the surface tension of nickel with crystallographic orientation", *Acta metallurgica*, vol. 9, no. 6, pp. 570–576, Jun. 1961. DOI: 10.1016/0001-6160(61)90160-2 (cit. on p. 75).

[76] N. Seriani and F. Mittendorfer, "Platinum-group and noble metals under oxidizing conditions", *Journal of physics: Condensed matter*, vol. 20, no. 18, p. 184 023, Apr. 2008. DOI: 10.1088/0953-8984/20/18/184023 (cit. on p. 75).

[77] J. Ye and C. V. Thompson, "Anisotropic edge retraction and hole growth during solid-state dewetting of single crystal nickel thin films", *Acta materialia*, vol. 59, no. 2, pp. 582–589, Jan. 2011. DOI: 10.1016/j.actamat.2010.09.062 (cit. on p. 75).

[78] V. Lubarda, "On the effective lattice parameter of binary alloys", *Mechanics of materials*, vol. 35, no. 1-2, pp. 53–68, Jan. 2003. DOI: 10.1016/s0167-6636(02)00196-5 (cit. on p. 77).

[79] G. Dehm, B. J. Inkson, and T. Wagner, "Growth and microstructural stability of epitaxial Al films on (0001) α-Al2O3 substrates", *Acta materialia*, vol. 50, no. 20, pp. 5021–5032, 2002 (cit. on p. 77).

[80] K. Persson, "Materials Data on Au (SG:225) by Materials Project", Apr. 2016. DOI: 10.17188/1307925 (cit. on p. 91).

[81] K. Persson, "Materials Data on Ni (SG:225) by Materials Project", Feb. 2016. DOI: 10.17188/1199153 (cit. on p. 91).

[82] M. Bienzle, T. Oishi, and F. Sommer, "Thermodynamics and local atomic arrangements of gold-nickel alloys", *Journal of alloys and compounds*, vol. 220, no. 1-2, pp. 182–188, Apr. 1995. DOI: 10.1016/0925-8388(94)06003-7 (cit. on p. 91).

[83] K. Persson, "Materials Data on Al2O3 (SG:167) by Materials Project", Nov. 2014. DOI: 10.17188/1187823 (cit. on p. 91).

Appendix

A

Table A.1: Crystallographic database for XRD.

Element	$(h\,k\,l)$	2θ
Au [80]	(1 1 1)	38.24
	(2 0 0)	44.45
	(2 2 0)	64.68
Ni [81]	(1 1 1)	44.49
	(2 0 0)	51.84
	(2 2 0)	76.37
$Au_{45}Ni_{55}$ [82]	(1 1 1)	40.94
	(2 0 0)	47.63
	(2 2 0)	69.65
α-Al_2O_2 [83]	(0 0 0 6)	41.68
	(3 $\overline{3}$ 0 0)	68.29

Table A.2: Peak positions for XRD and determination lattice constant of the measurement series ERL.

nominal Au content / at.%	$(h\,k\,l)$	2θ	a / Å
0	(1 1 1)	44.5	3.52
	(2 0 0)	51.85	
15	(1 1 1)	42.6	3.67
	(2 0 0)	49.59	
28	(1 1 1)	41.44	3.77
	(2 0 0)	48.23	
41	(1 1 1)	40.61	3.84
	(2 0 0)	47.24	
43	(1 1 1)	40.37	3.87
	(2 0 0)	46.94	
45	(1 1 1)	40.34	3.87
	(2 0 0)	46.91	
47	(1 1 1)	40.23	3.88
	(2 0 0)	46.79	
49	(1 1 1)	40.11	3.89
	(2 0 0)	46.66	
55	(1 1 1)	39.75	3.92
	(2 0 0)	46.23	
70	(1 1 1)	39.15	3.98
	(2 0 0)	45.51	
85	(1 1 1)	38.64	4.03
	(2 0 0)	44.90	
100	(1 1 1)	38.64	4.07
	(2 0 0)	44.43	

Table A.3: Peak positions for XRD and determination of the lattice constant of the measurement series ILM.

nominal Au content / at.%	$(h\,k\,l)$	2θ	a Å
28	(1 1 1)	41.19	3.79
	(2 0 0)	48.26	
35	(1 1 1)	40.91	3.82
	(2 0 0)	47.58	
40	(1 1 1)	40.59	3.85
	(2 0 0)	47.26	
45	(1 1 1)	40.26	3.88
50	(1 1 1)	40.05	3.90
52.5	(1 1 1)	39.90	3.91
55	(1 1 1)	39.77	3.92
57.5	(1 1 1)	39.65	3.93
60	(1 1 1)	39.57	3.94
62.5	(1 1 1)	39.43	3.95

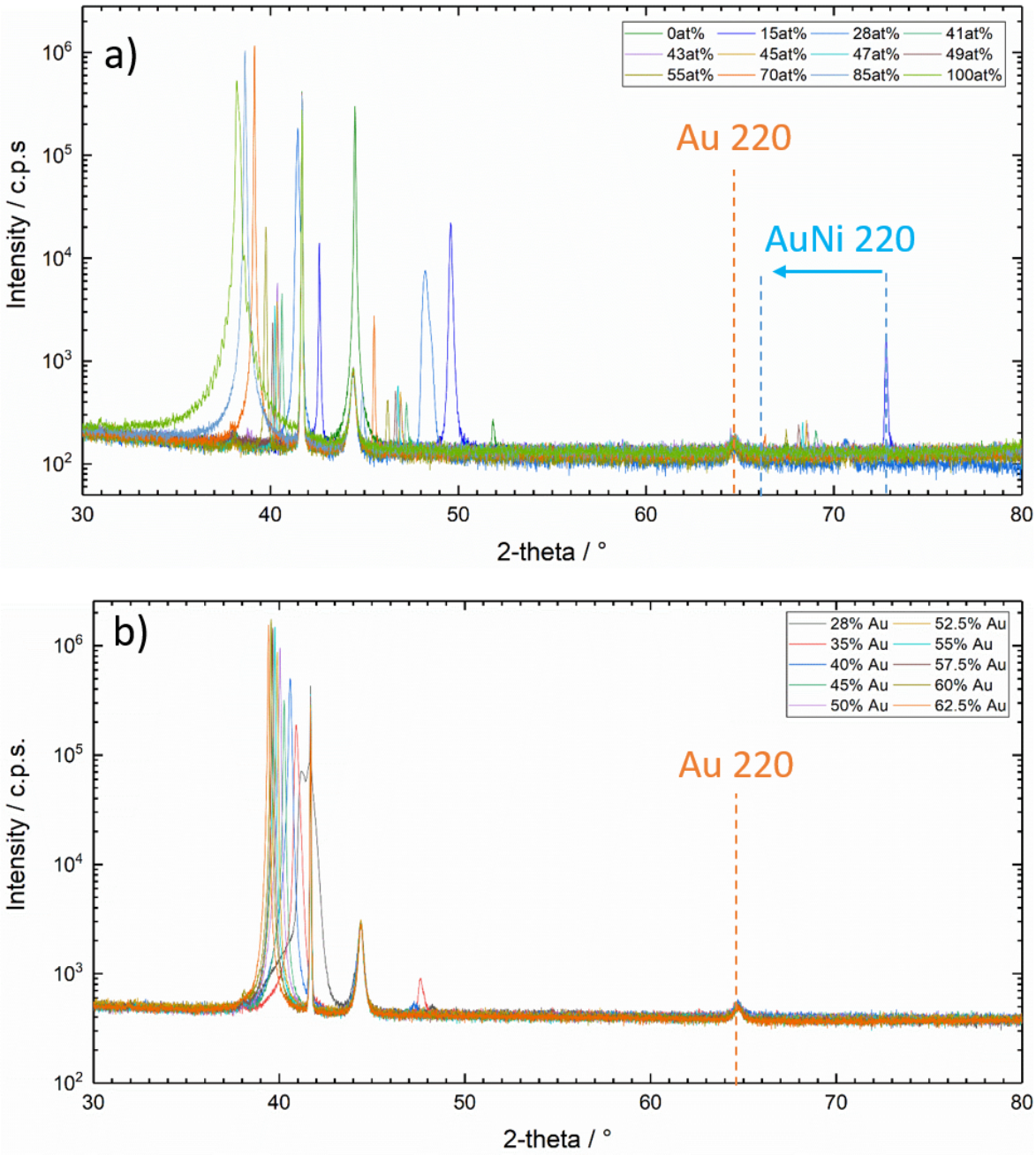

Figure A.1: Full range XRD measurement of ERL (a) and ILM (b).

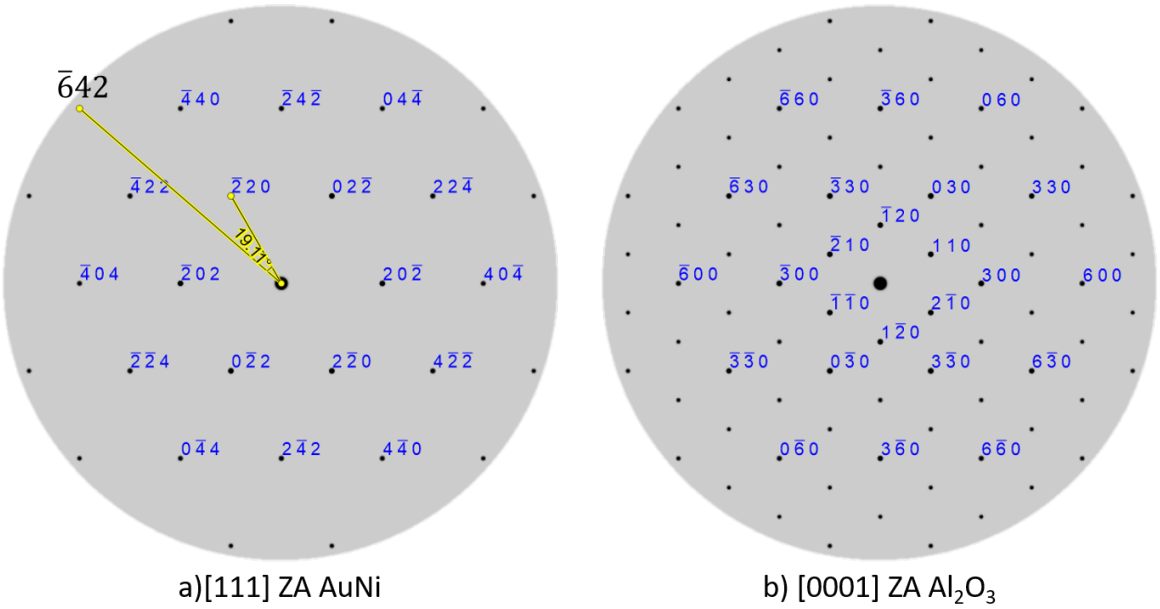

Figure A.2: Simulated SAED-Patterns of AuNi (a) and α-Al_2O_3 (b). After rotating the AuNi pattern about 19.11° the $\langle\bar{3}\,2\,1\rangle$ direction is parallel to the $\langle\bar{3}\,3\,0\,0\rangle$ direction of α-Al_2O_3.

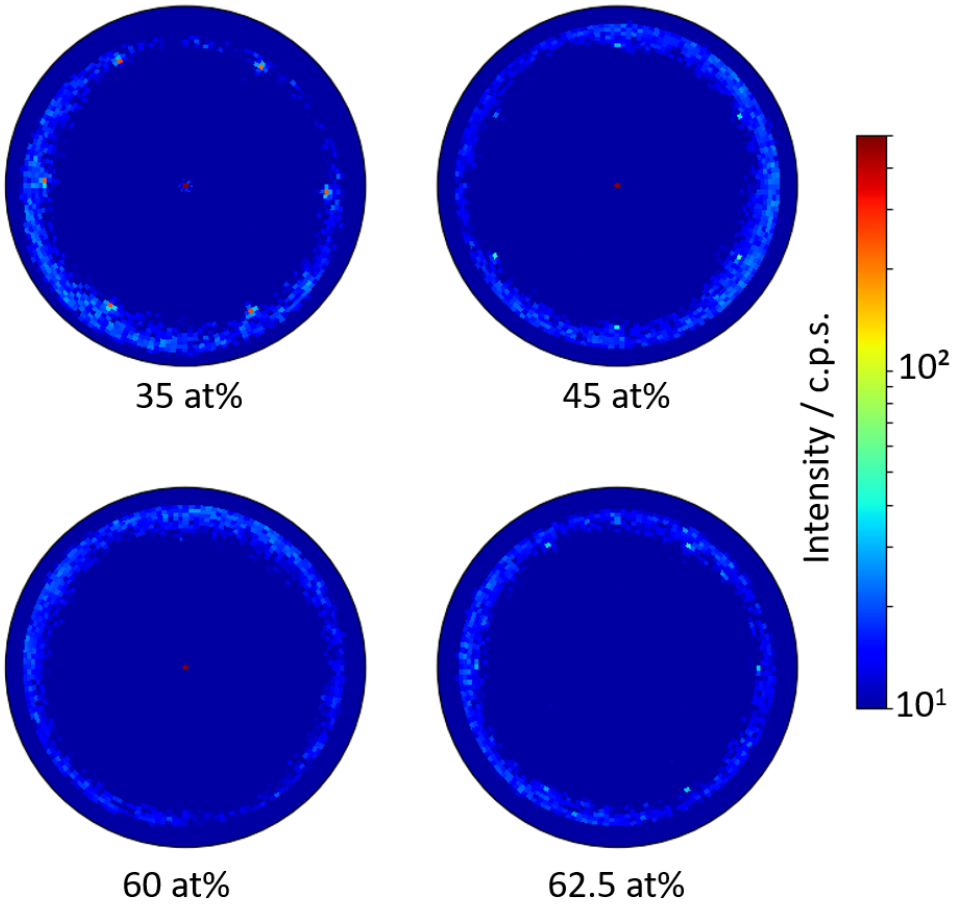

Figure A.3: (0 0 0 6) pole figures of α-Al_2O_3.

Prüfungsrechtliche Erklärung

Ich versichere, dass ich die Arbeit ohne fremde Hilfe und ohne Benutzung anderer als der angegebenen Quellen angefertigt habe und dass die Arbeit in gleicher oder ähnlicher Form noch keiner anderen Prüfungsbehörde vorgelegen hat und von dieser als Teil einer Prüfungsleistung angenommen wurde. Alle Ausführungen, die wörtlich oder sinngemäß übernommen wurden, sind als solche gekennzeichnet.

_____ Erlangen, den 16. März 2020

Martin Dierner